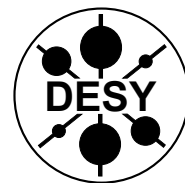


**DEUTSCHES ELEKTRONEN-SYNCHROTRON**  
Ein Forschungszentrum der Helmholtz-Gemeinschaft



DESY-THESIS-2017-050

December 2017

## **A Novel Optical Tool for Controlling and Probing Ultrafast Surface Dynamics**

by

Y. Yang

ISSN 1435-8085

**NOTKESTRASSE 85 - 22607 HAMBURG**

# **A novel optical tool for controlling and probing ultrafast surface dynamics**

**Yudong Yang**

Fachbereich Physik  
Universität Hamburg

zur Erlangung des akademischen Grades  
*Doctor rerum naturalium*

Fakultät für Mathematik, Informatik  
und Naturwissenschaften

Dezember 2017



Gutachter der Dissertation:

Prof. Dr. Franz X. Kärtner

Prof. Dr. Wilfried Wurth

Zusammensetzung der Prüfungskommission:

Prof. Dr. Franz X. Kärtner

Prof. Dr. Wilfried Wurth

Prof. Dr. Daniela Pfannkuche

Prof. Dr. Markus Drescher

Jun.-Prof. Dr. Thorsten Upheus

Datum der Disputation:

21.12.2017





## **Eidesstattlich Versicherung**

### *Delaration on oath*

Hiermit erkläre ich an Eides statt, dass ich die vorliegende Dissertationsschrift selbst verfasst und keine anderen als die angegebenen Quellen und Hilfsmittle benutzt habe.

*I hereby declare, on oath, that I have written the present dissertation by my own and have not used other than the acknowledge resources and aids.*

Yudong Yang  
Dezember 2017

Hamburg, den  
*Hamburg, date*

Unterschrift  
*signature*



## Acknowledgements

First and foremost, I would like to express my deep gratitude to my supervisor Prof. Dr. Franz X. Kärtner for offering me the lifetime opportunity to work on this exciting project during my doctoral study. His profound knowledge, broad perspective and, more importantly, never-fading enthusiasm on research has always been the inspiration for me and set him as my role model. Thanks to his support, I have been granted a large degree of independence on research and allowed to fulfill my intellectual curiosity. I feel truly honored by the opportunity to work under his supervision. In addition, I would like to thank my co-supervisor Prof. Dr. Wilfried Wurth. Discussions with him on surface science are stimulating and have broadened my vision on this field. Moreover, his concise suggestions have helped me greatly on the progress on my research project.

I also would like to extend my gratitude to many colleagues who have contributed directly or indirectly to my doctoral thesis, without whom my research project would be doomed failure. First, I would like to thank Dr. Oliver D. Mücke who is the project leader of the attoscience project. His support has been there since the very first day of my doctoral study. The discussions with him have greatly broadened my vision about ultrafast optics and attosecond science. Moreover, he is always able to provide helpful advice either on theory or experiment. Meanwhile, Dr. Giovanni Cirimi also has shared his deep understanding about ultrafast optics to help me make progress on my project. He has the capability to turn the laboratory into a joyful working place. I would like to also thank Dr. Hüseyin Çankaya. Without his great efforts on laboratory organization, progress on my project would be impossible. On the other hand, Roland Mainz and Giulio Maria Rossi are the persons with whom I worked most tightly during my doctoral study. Working with them as well as discussing with them over very diverse topics has been always a great pleasure. The friendships with both of them are highly appreciated. In the meantime, I have benefited a lot from Dr. Liwei Song's skilled experience on constructing the few-cycle laser pulse source. Discussions with Dr. Phillip (Donnie) D. Keathley have then helped me greatly on building the attosecond pulse apparatus. Besides, I would like to thank Dr. Shaobo Fang for initiating the construction of the hollow-core fiber compressor as well as Dr. Shih-Hsuan Chia for designing the double-chirped mirrors and offering advice on pulse compression. Furthermore, I am grateful to Prof. Dr. Thorsten Uphues and Tanja Neumann

from the Uphues group. Prof. Dr. Thorsten Uphues and Tanja Neumann have designed the narrow-bandwidth multilayer mirror monochromator. Meanwhile, Tanja Neumann has spent great efforts on building the monochromator. Moreover, Prof. Dr. Thorsten Uphues has provided me valuable advice on constructing the attosecond pulse apparatus. Last but not least, I would like to also thank Dr. Giuseppe Mercurio from the Wurth group for coordinating the planned surface science experiments.

Furthermore, I would like to thank our group secretary Christine Berber for her dedicated work and support on the administrative affairs, which have allowed me to focus on research.

Finally, I would like to express my deepest gratitude to my parents, my sister and my friends for their long-lasting unconditional support during my doctoral study. This work is dedicated to my most beloved ones.

## Abstract

Ultrashort pulse laser sources have been greatly developed over the past few decades. The available pulse duration has been reduced to the single-cycle pulse regime. The discovery of high harmonic generation has freed us from the limitation of the laser wavelength. Moreover, the demonstration of isolated attosecond pulse generation has indicated the advent of the attosecond science era. Attosecond pulses undoubtedly allow one to study ultrafast dynamics with unprecedented time resolution. However, physical systems with genuine attosecond time scale dynamics are rather challenging to find. Ultrafast surface charge transfer, which is an important process in photochemistry and electrochemistry, is a good candidate experimental system exhibiting attosecond electronic dynamics. Specifically, the ultrafast surface charge transfer on the  $c(4\times 2)S/Ru(0001)$  surface was previously studied and the charge transfer time inferred to be 320 as using core-hole clock spectroscopy at a synchrotron facility. In order to measure this benchmark attosecond electronic dynamics with real time-resolving methods, pump pulses centered at 160 eV and probe pulses centered at 40 eV are required. To this end, a dedicated attosecond experimental beamline including an ultrashort laser pulse source and an attosecond pulse generation and characterization setup has been designed and is being developed. The author of this thesis was responsible for the construction of the attosecond experimental beamline which will be used ultrafast surface charge transfer studies.

In this thesis, a completely functional attosecond extreme ultraviolet (XUV) beamline, which includes a few-cycle laser pulse source, an attosecond pulse generation and characterization setup, is described. A commercial Ti:sapphire-based chirped-pulse amplification (CPA) laser system is the overall source of the beamline. The laser system is actively carrier-envelope phase (CEP) stabilized and the output pulse duration is  $\sim 35$  fs. The laser pulse spectrum is then broadened via self-phase modulation by means of propagation through a gas-filled hollow-core fiber. The output pulses, spectrally broadened and temporally stretched, are recompressed with double-chirped mirrors. The compressed few-cycle pulses are characterized with SHG-FROG. The pulse characterization difficulties due to the broad bandwidth associated with few-cycle pulses have been tackled by exploiting the FROG trace frequency marginal correction. The pulse duration is measured to be 5.3 fs. The few-cycle pulses are then used for HHG in the attosecond pulse generation setup. The generated XUV pulses are characterized with an XUV

spectrometer, which is equipped with varied line space gratings and an XUV CCD camera as detector. An XUV continuum, indicating the generation of isolated attosecond pulses, has been obtained with the attosecond pulse generation setup via double optical gating. The XUV continuum supports pulse durations shorter than 300 as. Meanwhile, obvious CEP effects on the XUV continuum strongly support the generation of isolated attosecond pulses. Full characterization of the attosecond pulses requires measurement of a photoelectron energy spectrogram in the presence of both the streaking IR and XUV fields. The XUV beam is focused by a gold coated toroidal mirror with grazing incidence. The delay between the XUV pulses and the IR pulses is controlled by varying the difference between the arm lengths of a Mach-Zehnder interferometer. A FROG-CRAB photoelectron spectrogram, which is used for attosecond pulse characterization, has been measured. The highly demanding interferometric stability for attosecond streaking experiments is achieved passively thanks to an elaborate vibration decoupling design of our vacuum system.

In contrast to the broad bandwidth of the XUV continuum required for generating attosecond pulses, narrow bandwidth XUV sources with tunability are important for photoelectron spectroscopy experiments requiring high spectral resolution. To obtain an XUV source with narrow bandwidth and tunability for our experiments, a multilayer mirror monochromator has been designed and developed by our collaboration partners from Prof. T. Uphues group. The multilayer mirror monochromator is able to select out a desired spectral region with bandwidth narrower than 0.5 eV in the range between 90 eV and 98 eV. In this thesis, the characterization of the multilayer mirror monochromator has been carried out in collaboration with Prof. T. Uphues group.

Some more efforts are still necessary on implementing the attosecond pulse reconstruction algorithm and completing the setup automatization. Eventually, the beamline will become a powerful tool for time-resolved attosecond dynamics studies and also XUV related spectroscopy studies in the near future.

## Zusammenfassung

Ultrakurzpuls-laser haben in den vergangenen Jahrzehnten eine große Entwicklung erfahren. Die verfügbaren Pulsdauern konnten bis in den Einzyklenbereich reduziert werden. Die Entdeckung der Erzeugung hoher Harmonischer hob die Beschränkung in der Laserwellenlänge auf den sichtbaren Bereich oder länger auf. Weiterhin hat die erstmalige Erzeugung von isolierten Attosekundenpulsen das Zeitalter der Attosekundenphysik eingeläutet. Attosekundenpulse erlauben zweifelsohne die Untersuchung von Dynamiken auf viel kürzeren Zeitskalen als je zuvor möglich. Nichtsdestotrotz ist es schwierig, physikalische Systeme zu identifizieren, die eine echte Attosekundendynamik aufweisen. Ein guter Kandidat für einen solchen elektronischen Prozess auf der Attosekundenzeitskala sind ultraschnelle Ladungsträgerwechsel an Oberflächen, welche in photo- oder elektrochemischen Prozessen eine bedeutende Rolle spielen. Besonders der ultraschnelle Ladungsträgertransfer im  $c(4\times 2)S/Ru(0001)$  Adsorbat-Oberflächen-System war bereits Forschungsgegenstand, und auch die Ladungsträgertransferzeit konnte mittels Kernloch-Zeitreferenz-Spektroskopie an einer Synchrotronquelle bereits ein Wert von 320 as extrahiert werden. Um diese Referenzdynamik zeitaufgelöst beobachten zu können, werden Anregepulse mit 160 eV und Abfragepulse mit 40 eV Photonenenergie benötigt. Zu diesem Zweck wurde ein speziell dafür geeigneter experimenteller Versuchsaufbau inklusive eines parametrischen optischen Wellenformsynthesizers, sowie ein Aufbau zur Attosekundenpulserzeugung und -charakterisierung geplant und aufgebaut. Der Autor der vorliegenden Arbeit war verantwortlich für den Aufbau der Attosekundenpulserzeugung und -charakterisierung.

In dieser Arbeit wird ein voll funktionsfähiger XUV-Attosekundenaufbau beschrieben, bestehend aus einer Zwei-Zyklen-Laserquelle, sowie einem Aufbau zur Attosekundenpulserzeugung und -charakterisierung. Ein kommerzielles Titan:Saphir-Lasersystem basierend auf der Verstärkung von geschirpten Pulsen ist die Primärlaserquelle für die Attosekundenstrahlführung. Das Lasersystem ist mit einer aktiven Stabilisierung der Träger-Einhüllenden-Phase (CEP) ausgestattet, und die erzeugten Laserpulse besitzen eine Pulsdauer von  $\sim 35$  fs. Die Bandbreite der Laserpulse wird anschließend während der Propagation in einer gasgefüllten Hohlkernfaser durch Selbstphasenmodulation verbreitert. Die Ausgangspulse, die spektral verbreitert und zeitlich gestreckt sind, werden schließlich mittels doppelt-geschirpter Spiegel wieder rekomp-



primiert und mit SHG-FROG charakterisiert. Schwierigkeiten bei der Pulscharakterisierung aufgrund der großen Bandbreite der Wenig-Zyklen-Pulse wurden mit Hilfe der Frequenzmarginalkorrektur der FROG-Spur gelöst, die gemessene Pulsdauer der Wenig-Zyklen-Pulse beträgt 5,3 fs. Diese Wenig-Zyklen-Pulse treiben dann die höheren Harmonischen zur Attosekundenpulserzeugung. Die erzeugten Pulse im extremen ultravioletten (XUV) Spektralbereich wurden mit einem XUV Spektrometer, welches mit einem Gitter mit variablem Gitterabstand und einer XUV CCD-Kamera ausgestattet ist, charakterisiert. Ein kontinuierliches XUV-Spektrum, welches auf isolierte Attosekundenpulse hindeutet, wurde mittels „Double Optical Gating, DOG“ erzeugt. Die Bandbreite des XUV-Spektrums erlaubt Pulslängen unter 300 as. Die beobachtete starke Abhängigkeit der Form der XUV-Spektren von der CEP des treibenden Laserfeldes ist ein weiteres starkes Indiz für die Erzeugung von isolierten Attosekundenpulsen. Eine vollständige Charakterisierung der Attosekundenpulse mit der Attosekunden-Streaking Methode (FROG-CRAB) erfordert die Messung eines Photoelektronenspektrogramms bei gleichzeitiger Präsenz des XUV-Feldes und des IR-Laserfeldes. Der XUV-Strahl wird durch einen goldbeschichteten Toroidspiegel unter streifendem Einfall fokussiert. Die Zeitverzögerung zwischen den XUV und IR-Feldern wird durch Veränderung der Längendifferenz der beiden Arme eines Mach-Zehnder-Interferometers erreicht. Ein FROG-CRAB Photoelektronenspektrogramm, welches zur Attosekundenpulscharakterisierung verwendet wird, wurde im Experiment gemessen. Die für Attosekunden-Streaking-Messungen benötigte sehr hohe interferometrische Stabilität wurde durch geschickte Schwingungskopplung des Vakuumaufbaus vom optischen Aufbau erreicht.

Im Gegensatz zu den breitbandigen XUV-Kontinua, die zur Erzeugung von Attosekundenpulsen notwendig sind, sind abstimmbare schmalbandige XUV-Quellen wichtig für Photoelektronenspektroskopie-Experimente, die eine hohe spektrale Auflösung benötigen. Um eine abstimmbare schmalbandige XUV-Quelle zu realisieren, wurde in Kooperation mit der Arbeitsgruppe von Prof. Uphues ein Multilagenspiegel-Monochromator entwickelt. Dieser Monochromator erlaubt es ein weniger als 0,5 eV schmales Spektrum im Bereich von 90 eV bis 98 eV zu selektieren. In der vorliegenden Arbeit wurde dieser XUV Monochromator in Zusammenarbeit mit der Gruppe von Prof. Uphues charakterisiert.

Es sind noch ein paar weitere Anstrengungen nötig, um den Rekonstruktionsalgorithmus für die Attosekundenpulse anzuwenden und die Automatisierung des Versuchsaufbaus zu vollenden. In naher Zukunft wird der Attosekundenversuchsaufbau ein leistungsfähiges Werkzeug für zeitaufgelöste Untersuchungen der Attosekundendynamik und andere spektroskopische Anwendungen sein.

# Table of contents

<b>List of figures</b>	<b>xv</b>
<b>Nomenclature</b>	<b>xix</b>
<b>1 Introduction</b>	<b>1</b>
<b>2 Few-cycle pulse generation and characterization</b>	<b>7</b>
2.1 Chirped-pulse amplification laser system . . . . .	8
2.2 Carrier-envelope phase stabilization . . . . .	13
2.3 Hollow core fiber compressor . . . . .	23
2.4 Few-cycle pulse characterization . . . . .	28
2.4.1 Field autocorrelation and intensity autocorrelation . . . . .	28
2.4.2 Frequency-resolved optical gating . . . . .	30
2.4.3 Practical issues in few cycle pulses characterization with FROG . . . . .	33
2.5 Summary . . . . .	37
<b>3 High harmonic generation and isolated attosecond pulse generation</b>	<b>39</b>
3.1 Introduction to high harmonic generation . . . . .	39
3.1.1 Semiclassical model of high harmonic generation . . . . .	40
3.1.2 Quantum model of high harmonic generation . . . . .	49
3.1.3 Phase matching in high harmonic generation . . . . .	52
3.1.4 Experimental apparatus and experimental methods for high harmonic generation . . . . .	55
3.1.5 HHG experimental results . . . . .	66
3.2 Narrow-bandwidth multilayer mirror monochromator for XUV pulses . . . . .	73
3.2.1 Design of a narrow-bandwidth multilayer mirror monochromator . . . . .	74
3.2.2 Experimental characterization of the multilayer mirror monochromator . . . . .	78
3.3 Isolated attosecond pulse generation . . . . .	80
3.3.1 Polarization gating and double optical gating . . . . .	81

---

3.3.2	Experimental apparatus and methods for isolated attosecond pulse generation . . . . .	83
3.3.3	Experimental results of isolated attosecond pulses generation . . . . .	86
3.4	Summary . . . . .	89
<b>4</b>	<b>Attosecond pulse characterization</b>	<b>93</b>
4.1	Attosecond pulse characterization methods . . . . .	93
4.1.1	Reconstruction of attosecond beating by interference of two-photon transitions . . . . .	94
4.1.2	Complete reconstruction of attosecond burst . . . . .	96
4.2	Experimental apparatus and methods for attosecond pulse characterization . .	98
4.2.1	Focusing with a toroidal mirror . . . . .	101
4.2.2	Electron time-of-flight spectrometer . . . . .	104
4.2.3	Stability of the optical delay line . . . . .	109
4.3	Experimental results of attosecond pulse characterization . . . . .	109
4.4	Summary . . . . .	115
<b>5</b>	<b>Conclusion and outlook</b>	<b>117</b>
	<b>Publication list</b>	<b>121</b>
	<b>References</b>	<b>123</b>

# List of figures

1.1	Characteristic time scale of microscopic motions and the related energy . . .	2
1.2	Schematic of surface charge transfer time measurement. . . . .	5
2.1	Schematic of the Ti:sapphire laser system . . . . .	8
2.2	Schematic of a multipass amplifier . . . . .	9
2.3	Schematic of a regenerative amplifier . . . . .	10
2.4	Principle of chirped-pulse amplification . . . . .	11
2.5	Schematic of the CPA system . . . . .	12
2.6	Definition of CEP $\varphi_{CE}$ . . . . .	13
2.7	Electric fields of laser pulses with different CE-phases . . . . .	14
2.8	Frequency comb and $f_{CEO}$ . . . . .	15
2.9	Principle of f-2f self-referencing interferometry . . . . .	17
2.10	Schematic of f-2f interferometry setup for $f_{CEO}$ measurement of the oscillator pulses . . . . .	18
2.11	The f-2f beat signal monitored with an RF spectrum analyzer . . . . .	19
2.12	Schematic of f-2f interferometry setup for $\varphi_{CE}$ measurement of the amplified pulses . . . . .	20
2.13	CEP drift when CEP stabilization loops are running . . . . .	21
2.14	Illustration of principle of double chirped mirrors . . . . .	24
2.15	Photo of HCF compressor . . . . .	25
2.16	HCF output spectrum . . . . .	26
2.17	HCF output spectrum versus gas pressure . . . . .	27
2.18	Schematic of field autocorrelation measurement setup . . . . .	29
2.19	Schematic of intensity autocorrelation measurement setup . . . . .	30
2.20	Schematic of SHG-FROG measurement setup . . . . .	31
2.21	FROG retrieval algorithm flowchart . . . . .	32
2.22	FROG trace frequency marginal correction . . . . .	34
2.23	FROG measurement and retrieval . . . . .	36

---

3.1	A schematic HHG spectrum . . . . .	40
3.2	Trajectories of an electron ionized at different phase . . . . .	44
3.3	Trajectories of electrons ionized at different phase and return within one laser cycle . . . . .	46
3.4	Electron return kinetic energy versus the ionization time and recombination time	47
3.5	Photo of the vacuum chambers and the XUV spectrometer . . . . .	56
3.6	XUV transmission and reflectivity of materials . . . . .	56
3.7	Design of the vibration isolation vacuum feedthrough . . . . .	57
3.8	CAD drawing of the experimental setup configuration . . . . .	59
3.9	Optical configuration of the experimental apparatus . . . . .	60
3.10	Picture of the HHG gas target . . . . .	61
3.11	McPherson 251MX XUV spectrometer . . . . .	63
3.12	Photo of the McPherson 251MX XUV spectrometer gratings . . . . .	65
3.13	HHG beam profile observed via the zeroth diffraction order beam of the grating	67
3.14	2-D image of the diffracted HHG signal via the CCD camera . . . . .	68
3.15	2-D image of HHG signal used for wavelength calibration . . . . .	69
3.16	HHG signal for wavelength calibration and filter transmission . . . . .	69
3.17	Schematic of the XUV diffraction grating . . . . .	70
3.18	HHG spectrum obtained after wavelength calibration . . . . .	71
3.19	HHG spectrum obtained with argon . . . . .	72
3.20	HHG spectrum obtained with krypton . . . . .	72
3.21	HHG spectrum covers up to 180 eV obtained with neon gas. . . . .	73
3.22	Reflectivity of one multilayer mirror . . . . .	76
3.23	Schematic of optical beampath in the monochromator . . . . .	77
3.24	Photo of the multilayer mirror monochromator . . . . .	77
3.25	Reflectivity of the monochromator at 15° incidence angle . . . . .	78
3.26	Monochromatic XUV spectrum and the monochromator reflectivity . . . . .	79
3.27	Electric field in polarization gating . . . . .	82
3.28	Two color electric field . . . . .	84
3.29	Schematic of polarization gating and double optical gating . . . . .	85
3.30	Dependence of HHG yield on the ellipticity of the laser pulses . . . . .	86
3.31	Dependence of HHG yield on rotation angle of the quartz plate . . . . .	87
3.32	Width of HHG spectral peaks dependence on the double optical gating field .	88
3.33	XUV continuum with double optical gating . . . . .	89
3.34	Variation in the XUV spectrum as the CEP of the laser pulses changes . . . . .	90
4.1	Principle of sideband formation . . . . .	95

---

4.2	Schematic of the attosecond pulse characterization experiment setup . . . . .	99
4.3	Optical configuration in the HHG chamber . . . . .	100
4.4	Optical configuration in the toroidal mirror chamber . . . . .	101
4.5	Schematic of a toroidal mirror . . . . .	102
4.6	Toroidal mirror assembly in our experimental setup . . . . .	103
4.7	Electron time-of-flight spectrometer ETF11 . . . . .	105
4.8	Schematic of a time-of-flight spectrometer . . . . .	105
4.9	Photo of the MCP and the TOF . . . . .	106
4.10	Toroidal mirror focal profile . . . . .	110
4.11	Combined beam profiles after the interferometer . . . . .	111
4.12	Raw MCP signal recorded with an oscilloscope . . . . .	111
4.13	TOF spectrum conversion . . . . .	112
4.14	Photoelectron spectrum with XUV field alone and with IR-XUV field . . . . .	113
4.15	Photoelectron spectrogram measured with our experimental apparatus . . . . .	114



# Nomenclature

## Acronyms / Abbreviations

CEP Carrier-envelope phase

CPA Chirped pulse amplification

CRAB complete reconstruction of attosecond burst

DCM double-chirped mirror

DOG double optical gating

ESCA electron spectroscopy in chemical analysis

FROG Frequency resolved optical gating

HCF hollow-core fiber

HHG High harmonic generation

KLM Kerr lens mode-locking

OPA Optical parametric amplifier

SLM spatial light modulator

SPIDER spectral phase interferometry for direct electric field reconstruction

XUV extreme ultraviolet





# Chapter 1

## Introduction

Curiosity about the world has always been a main impetus of human adventures. Not being satisfied with just the knowledge about the world which can be experienced personally, our adventurous minds drive us to explore the world otherwise unimaginable. Tools are invented to break the cognition boundaries set by our senses. Starting with Muybridge's question of the horse in motion about one and a half centuries ago, cameras have been helping us look at the fast moving world. However, even most advanced modern cameras are not fast enough for observing the motion of atoms, molecules and electrons. New approaches are in demand. The advent of the laser in 1960 heralded a new era in science. The first operational laser was demonstrated by T. H. Maiman at Hughes Research Labs [1]. Shortly afterwards, nanosecond laser pulses became a reality thanks to the development of the Q-switching technique [2]. Ultrafast physics and nonlinear optics also emerged during the same period. The first second harmonic generation was observed in 1961 [3]. The mode-locking technique [4, 5] further pushed the frontiers and allowed generation of laser pulses with femtosecond durations. Nowadays, Ti:sapphire Kerr-lens mode-locked oscillators which are able to deliver pulses shorter than 5 fs are commonly used in laboratories [6–8]. The intrinsic time scale of a process is determined by the transition energy involved, as shown in Fig 1.1. Molecular rotations take place on a picosecond time scale. The time scale of molecular vibrations is hundreds of femtoseconds. In contrast, electrons move on a much shorter time scale of few femtoseconds to attoseconds. Femtosecond laser pulses allow us to study phenomena, like the formation and rupture of chemical bonds, in real time, which had never been done before. The Nobel Prize in chemistry was awarded to A. Zewail in 1999 for his contribution to this research field named femtochemistry.

To study microscopic processes in a system in a time-resolved manner, the pump-probe spectroscopy scheme is commonly adopted. In the pump-probe method, the first laser pulse (pump) excites the system, then the second laser pulse (probe) interrogates the temporal evolution of the process. The information of the dynamics of the system under investigation

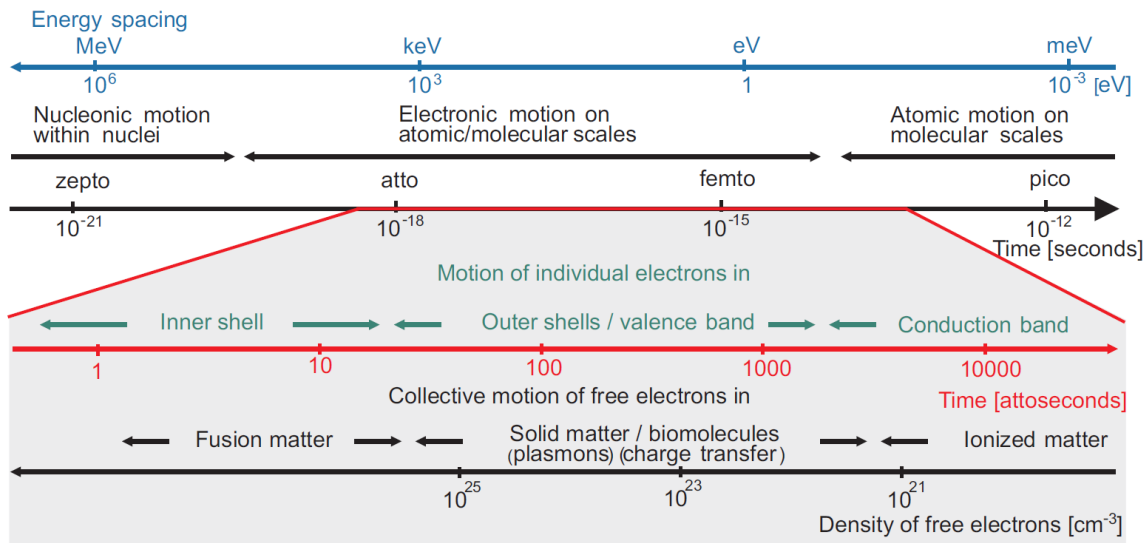


**Fig. 1.1** Characteristic time scales of microscopic motions and the related energy scales. From Ref. [9]

can be encoded either in the probe pulse or in other resultants, such as secondary photons, electrons or ions. This method is called time-resolved spectroscopy. The temporal resolution of time-resolved spectroscopy measurements is typically determined by the duration of the pulses used. The duration of the probe pulses should ideally be significantly shorter than the dynamical process under investigation.

Electronic motion in atoms and molecules has a natural time scale ranging from few femtoseconds to attoseconds. Therefore, femtosecond laser pulses are not sufficient for studying processes involving electronic dynamics. The discovery of high harmonic generation (HHG) and later the demonstration of isolated attosecond pulse generation have announced the advent of the attosecond science era. HHG is a strong-field phenomenon, in which electrons, that are ionized in the first step by the strong laser field, are subsequently driven by the laser field back to the parent ions, and the excess energy of electrons acquired by the driving laser field is released in form of extreme ultraviolet (XUV) photons. The XUV spectrum consists of integer odd harmonic orders of the fundamental driving field. Very high-order harmonics, that may extend up to thousands of harmonic orders, can be generated. The HHG process is extremely sensitive to the shape of the laser field and is intrinsically a process with attosecond time scale. Controlling the waveform of the laser field and thus the force exerted on the electrons would allow us to control the phase and the amplitude of the attosecond XUV pulses generated. In fact, the capability to control elementary chemical reactions via the intense laser field control existed before the birth of attosecond pulses. This is called quantum coherent control of chemical reactions [10]. Generation of arbitrarily shaped waveforms with a time scale ranging from

---

few-cycle to sub-cycle has been pursued by the ultrafast optics community for years [11]. One of the promising routes towards intense arbitrary waveform generation is the optical parametric waveform synthesizer [12, 13]. In an optical waveform synthesizer [14], the amplitude and phase of different spectral components in a laser pulse are controlled independently to achieve certain desired waveforms  $E(t)$ .

Chemical reactions take place in various environments, e.g., in gas phase or in condensed phase. Chemical reactions, such as the formation of a molecule, in gas phase are the simplest case to model. However, in many practical important situations, the chemical reactions take place in more complex environments. In these environments, the reacting species are constantly exchanging energy and momentum with other neighboring molecules. Therefore, the effects of the environments on the chemical reactions can only be considered through the average properties. In the meantime, the gas-solid interface is an environment with complexity between the two cases above. The interactions between the adsorbed molecule and the surface are usually more regular which allows for more precise measurements and more detailed theoretical descriptions. Therefore, the studies of the chemical reactions on surfaces provide us a deeper understanding of chemical reactions in condensed phases. Due to its importance in chemistry, studies of the chemical processes at surfaces have a long history and several Nobel Prizes have been awarded to researches related to surface chemistry, e.g., the Nobel Prize in chemistry in 2007 was awarded to G. Ertl. The chemical reactions on the surfaces can be studied with the electron spectroscopy in chemical analysis (ESCA) technique which is a well-established tool to study the chemical environment of molecular systems. K. Siegbahn is awarded the Nobel Prize in physics in 1981 for his extensive efforts in developing ESCA into a useful analytical tool. The realization of ultrashort XUV pulses allows one to perform ESCA in time-resolved manner [15, 16]. Various surface dynamics study experiments have been performed with XUV ultrashort pulses from both free-electron lasers and HHG-based XUV sources. For instance, using the Linac Coherent Light Source (LCLS) free-electron x-ray laser, the electronic structure changes of CO molecules on Ru(0001) surface are studied [17]. Time-resolved core-level photoelectron spectroscopy on a W(110) surface has been performed with the FLASH free-electron laser [18]. On the other hand, first demonstration of direct monitor of surface chemical reactions on femtosecond time scales with ultrashort XUV pulses generated by HHG was first demonstrated in 2001 [19]. Since then, many experiments using a ultrashort XUV pulse source based on HHG, such as time-resolved study of core-level chemical shifts in a monolayer of aromatic molecules [20], direct observations of the structural and electronic dynamics of the photoinduced insulator–metal transition in VO<sub>2</sub> [21], femtosecond time-resolved core-level study of the surface photovoltage effect on the p-GaAs(100) surface [22], direct time-resolved observations of the lifetime of core-excited states of an atom adsorbed onto a surface [23],

have been performed. Moreover, various experiments are performed with sub-femtosecond resolution to resolve electronic dynamics in the natural time scale [24, 25]. For instance, experiments on direct time-domain access to charge dynamics with attosecond resolution were conducted in 2007 [26], as well as distinguishing electron–electron screening and charge scattering in the time domain in individual energy bands within a solid [27], measurement of the lifetime difference between photoelectrons born into free electron–like states and those excited into unoccupied excited states [28] and direct observation of electron propagation and dielectric screening on the atomic length scale [29]. Ultrafast surface charge transfer, which is important in photochemistry and electrochemistry as well as catalyst study, is processes which may exhibit attosecond-scale dynamics. One of the experiments to study the surface charge transfer time is performed with a  $c(4\times 2)S/Ru(0001)$  surface. The charge transfer time is inferred to be about 320 as [30]. In this synchrotron experiment, the attosecond dynamics was indirectly inferred using core-hole clock spectroscopy. The main goal of our research projects is to perform real attosecond time-resolved surface chemistry studies.

With the scientific goal to realize attosecond time-resolved spectroscopy measurement, including ultrafast surface charge transfer time measurement, an attosecond experimental apparatus is developed and constructed in our laboratory [12]. The attosecond experimental apparatus consists of a multi-millijoule (mJs) parametric waveform synthesizer as well as an attosecond pulse generation and characterization apparatus. The parametric waveform synthesizer consist of three 3-stage optical parametric amplifier (OPA) channels, which cover the spectral region from the visible to the infrared. The seed pulses of the three OPAs originate from a common source. The output of the three OPA outputs are combined coherently with controlled amplitude and phase. In the meantime, the author’s contribution in this experimental endeavor is the construction of the attosecond beamline, which allows attosecond pulse generation and characterization. Moreover, the author also implemented a hollow-core fiber compressor, which delivers energetic two-cycle (5.3 fs duration) pulses for construction and testing of the attosecond beamline. When the entire experimental system is completed, the above mentioned ultrafast surface transfer time measurement will be carried out.

In order to measure the surface charge transfer time of this system in a time-resolved manner, an attosecond pulse centered at 160 eV resonantly excites an electron in the adsorbed sulfur atom to the  $3p_z$  level. Then, another attosecond pulse centered at 40 eV is used as the probe pulse. The probe pulse further excites the  $3p_z$  electron into the continuum. The yield of the photoelectron versus pump-probe delay tracks the charge transfer dynamics and allows to measure the charge transfer time.

In contrast to the broad bandwidth of the XUV continuum required for generating attosecond XUV pulses, monochromatic XUV sources with tunability are preferred in many experiments,

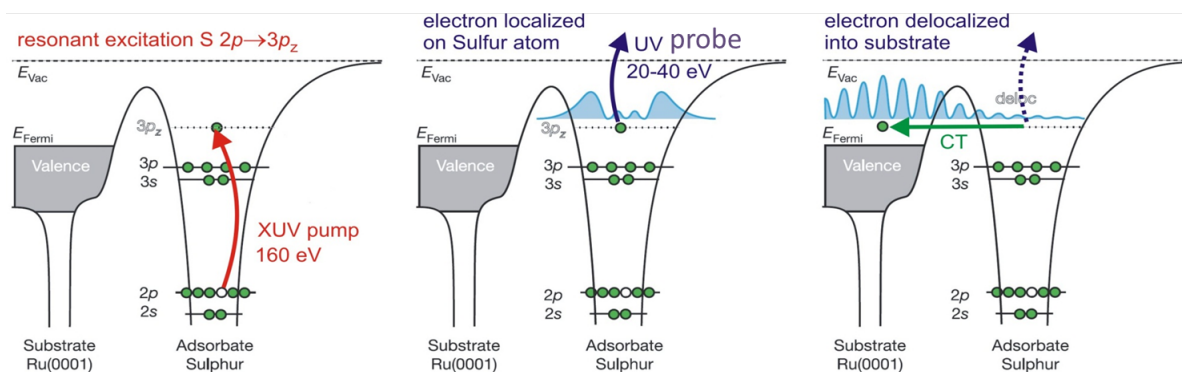


**Fig. 1.2** Schematic of time-resolved surface charge transfer pump-probe measurement. (Left) An inner electron is resonantly excited by XUV pulses centered at 160 eV, (middle) if the excited electron remains localized on the atom adsorbed on the surface when the XUV probe pulse centered at 40 eV arrives, a photoelectron is emitted, (right) if the excited electron has already transferred to the substrate when the XUV probe pulse arrives, no photoelectron is produced

such as time-resolved and angle-resolved photoelectron spectroscopies [31]. In order to obtain narrow-bandwidth XUV radiation, a multilayer mirror monochromator has been designed and developed by our collaboration partners from Prof. T. Uphues group. In this thesis, the characterization of the multilayer mirror monochromator inside our attosecond beamline has been carried out in collaboration with the Uphues group.

In this dissertation, the author's work on construction of a completely functional attosecond beamline, including carrier-envelope phase (CEP) controlled few-cycle pulse generation using a hollow-core fiber compressor, isolated attosecond pulse generation and characterization apparatus, is described. Besides, the characterization of the multilayer-mirror monochromator is also discussed. Some more efforts are still necessary on implementing the attosecond pulse reconstruction algorithm and completing the setup automatization. Eventually, the beamline will become a powerful tool for time-resolved attosecond dynamics studies and also XUV related spectroscopy studies in the near future.

This thesis is structured as follows:

*Chapter 2* contains the description of the laser system which consists of a commercial Ti:sapphire chirped-pulse amplification (CPA) system and a hollow-core fiber compressor. The CPA laser system is actively CEP-stabilized. Both the working principle of the CPA system and the CEP stabilization are introduced. The ultrashort pulse characterization method, frequency resolved optical gating (FROG), is discussed in detail. The characterization results of the few-cycle pulses from the hollow-core fiber compressor are presented. The pulse duration of the few-cycle pulses from the HCF compressor is characterized to be 5.3 fs corresponding to two optical cycles of light.

*Chapter 3* first describes the physics underlying high harmonic generation (HHG) and the experimental results are presented. The scientific background covers the semiclassical and the quantum model of single-atom response as well as the theory on phase matching. HHG from various noble gas media and also HHG with different laser pulses are presented. Then, the experimental results for the characterization of the narrow-bandwidth multilayer mirror monochromator are presented. Moreover, the experimental scheme and setup for isolated attosecond pulse generation are described. The XUV continuum generated using the double optical gating (DOG) technique is then presented. The XUV continuum supports a transform-limited pulse duration of  $\sim 300$  as.

*Chapter 4* first presents the attosecond XUV pulse characterization methods and the experimental apparatus for implementing these methods. The key components of the experimental apparatus, i.e., the toroidal mirror and the electron time-of-flight spectrometer, are discussed in detail. Finally, the experimental results, which are used for attosecond pulse characterization, are presented.

## Chapter 2

# Few-cycle pulse generation and characterization

Ultrashort-pulse lasers make intense electric fields comparable to the intra-atomic fields available and open up the doorway towards extreme nonlinear optics. High harmonic generation (HHG), which makes attosecond pulses possible, is one example of extreme nonlinear optics. Ultrashort-pulse lasers with pulse durations of tens of femtoseconds up to picoseconds can be used for HHG, provided the required intensity is achieved. The HHG obtained from gases forms an attosecond pulse train in the time domain which has similar length as the driving laser pulse [32, 33]. These attosecond bursts are separated by half of the laser cycle, which makes them not practical to use for many applications in time-resolved attosecond spectroscopy. In order to access the attosecond dynamics on their natural time scale, isolated attosecond pulses are essential. Sub-cycle driving pulses are desirable for direct isolated attosecond pulse generation, while combined with various gating methods, few-cycle pulses can also be employed for isolated attosecond pulse generation. Although few-cycle pulses with nanojoules (nJs) of pulse energy can be routinely generated from Ti:sapphire mode-locked laser oscillators [7], those pulses are not intense enough for HHG. Amplification that boosts the pulse energy from nanojoules (nJs) to millijoules (mJs) is in general necessary to generate intense ultrashort pulses applicable for HHG. Ultrafast amplifiers that can deliver mJs to 1 J are commercially available. However, the lower limit of the pulse duration of ultrashort-pulse amplifiers is usually a few tens of femtoseconds. Additional methods need to be employed to shorten the duration of the amplified pulses further. Typically, hollow-core fiber (HCF) compressors [34] are used to this end. This chapter covers the laser system used in the author's experimental setup, which consists of a carrier-envelope phase (CEP) controlled chirped pulse amplification (CPA) laser system and a hollow-core fiber compressor.



## 2.1 Chirped-pulse amplification laser system

The most common laser systems which provide multi-mJ pulse energy ultrashort pulses are Ti:sapphire-based laser systems which employ chirped-pulse amplification. The laser system utilized in the attosecond beamline developed in this thesis is a commercial system from Coherent Inc.. It consists of a CEP-stabilized mode-locked seed oscillator (Vitara), a CPA based amplifier with two amplification stages (Legend Elite Duo), and a CEP stabilization system. The scheme of this laser system is shown in Fig. 2.1.

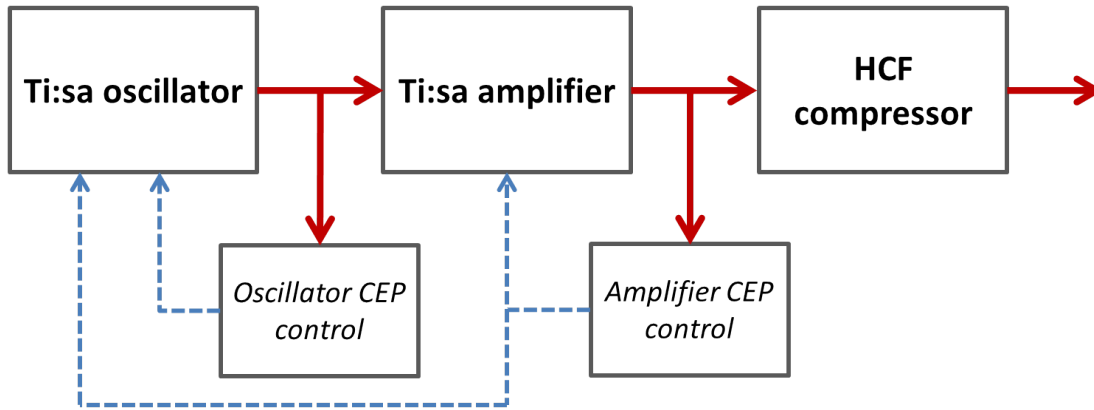


**Fig. 2.1** Schematic of the Ti:sapphire laser system. The laser system consists of a mode-locked seed oscillator, a CPA based amplifier with two amplification stages and a CEP stabilization system. The ultrashort pulses from the oscillator are amplified in the amplifier. The amplified pulses are then spectrally broadened and compressed to form few-cycle pulses in the hollow-core fiber compressor. Small portions of the oscillator pulses and of the amplified pulses are used as input to the CEP measurement and control systems. The CEP control systems then control actuators in both the oscillator and the amplifier for active CEP stabilization.

The oscillator is a Kerr-lens mode-locked (KLM) Ti:sapphire oscillator, which is the most commonly used type of laser oscillator in ultrafast optics laboratories. Ti:sapphire oscillators that have octave-spanning spectra and deliver sub-5 fs pulses are available [8]. However, oscillators that deliver such broad bandwidth pulses are less robust than those only having  $>10$  fs output pulses. Moreover, the broad bandwidth is difficult to preserve during the amplification due to various issues, e.g., gain narrowing [35]. As a result, in the case where oscillators are used as the seed source for an ultrafast amplifier, one would usually prefer oscillators with pulses longer than 10 fs.

Amplifying media in a femtosecond amplifier must have broad optical gain bandwidth. Nowadays, Ti:sapphire is the most widely used medium for femtosecond amplifiers, which is also the prevailing gain medium for solid-state mode-locked oscillators. In order to tackle the problem that solid-state media typically have low gain per pass, the seeds are commonly

arranged to pass the gain medium multiple times. Two commonly used schemes to achieve this are termed multipass amplifiers and regenerative amplifiers, respectively.

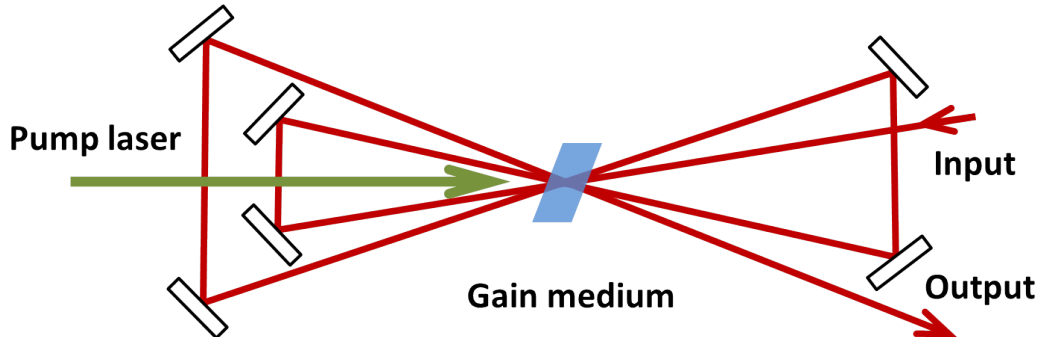


**Fig. 2.2** Schematic of a multipass amplifier

The first scheme is the multipass amplifier. In a multipass amplifier, a number of mirrors are used to guide the seed pulses through the gain crystal for several times as in Fig. 2.2. The beam paths of different passes through the crystal are separated geometrically. Meanwhile, with appropriate beam layout design, it is possible to send the laser pulses through different portion of the gain crystal with different gain. However, the geometrical complexity limits the number of passes that can be achieved with a multipass amplifier. Moreover, it lacks flexibility since the number of passes and thus the gain is fixed for a certain multipass amplifier. The fixed geometry also increases the complexity for overlapping the pump and the seed beam.

The other amplifier scheme is the regenerative amplifier, see Fig. 2.3. Different from a multipass amplifier, the number of passes through the gain crystal in a regenerative amplifier is controlled by an optical switch. The optical switch is usually realized with an electro-optic modulator (typically a Pockels cell) and a polarizer. By manipulating the polarization state of the pulses, one can choose to let the pulse into the cavity, keep the pulse in the cavity, or release the pulse from the cavity. In Fig. 2.3, an input pulse is reflected by the thin film polarizer (TFP) into the cavity. The pulse returns to the TFP with the polarization plane rotated by  $90^\circ$  due to a double pass through the quarter waveplate (QWP). When the Pockels cell is kept off, the pulse would arrive at the TFP from the right the next time with the polarization plane rotated by  $180^\circ$  with respect to the input pulse, and the pulse is reflected out of the cavity. In this case, the pulse is rejected by the amplifier. Meanwhile, if the Pockels cell is switched on after the first double pass of the pulse, the QWP and the Pockels cell form an effective half waveplate. A pulse passing through a half waveplate twice maintains the polarization state so that the pulse is able to transmit through the TFP. When the desired number of passes through the gain crystal is reached, the pulse can be coupled out from the cavity by switching off the Pockels cell. Obviously, in a regenerative amplifier, the number of passes through the gain medium of a

pulse can be easily controlled. As a result, the number of passes in a regenerative amplifier can be very large which allows for very high gain. However, the large numbers of passes through the gain medium introduces large material dispersion in the pulses due to the thick material in the beam path. This dispersion brings about some difficulties for full compression of the output pulses.

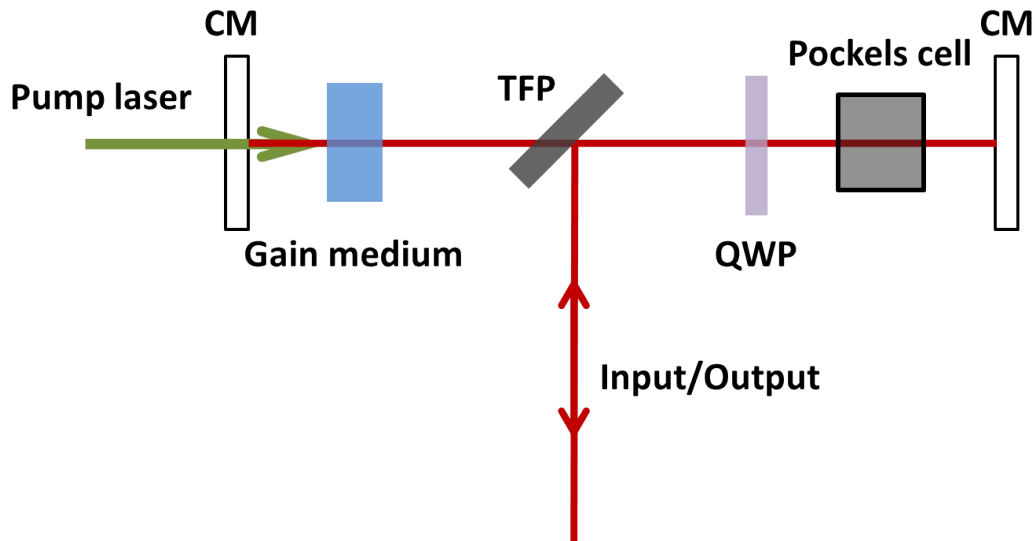


**Fig. 2.3** Schematic of a regenerative amplifier. CM: cavity mirror, TFP: thin film polarizer, QWP: quarter waveplate.

When a high-power ultrashort-pulse amplifier is scrutinized, there are some special problems to tackle. One of these problems is that, due to high intensity associated with the amplified ultrashort pulses, the high-energy pulse can induce nonlinear refractive index phenomena, such as self-focusing, in the gain medium. With self-focusing occurring, the intensity of the laser pulse can easily exceed the damage threshold of the gain medium. For example, the critical power, above which self-focusing appears, for Ti:Sapphire is  $P_{crit} = 2.6 \text{ MW}$  [36]. Considering an amplifier, as the one in the author's laboratory, of which the output is 35 fs and 5 mJ, the peak power of the pulses is about 150 GW. One can expect pulses with this high intensity would cause serious damage to the gain medium. The damage on the gain medium due to nonlinear beam propagation limits the maximum power can be reached by an amplifier.

The method called chirped-pulse amplification (CPA) has successfully overcome this problem [37, 38]. In applying CPA, the pulses are first chirped by passing through a highly dispersive system. The pulses maintain the bandwidth while having much longer temporal durations. The pulses after stretching can pass through the gain medium safely thanks to the reduced peak power. After amplification, the pulses will go through another dispersive system, which has dispersion with opposite sign compared to the first one. The residual chirp

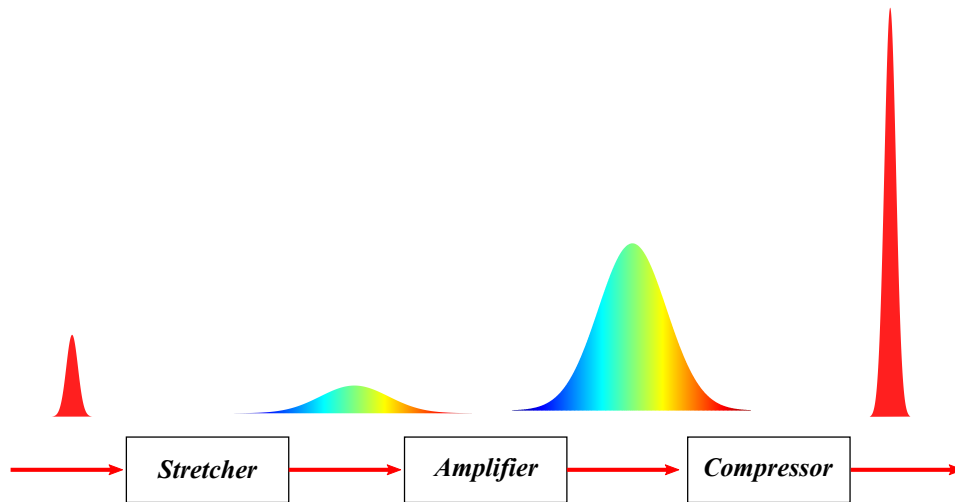


**Fig. 2.4** Principle of chirped-pulse amplification

in the pulses will be taken away and the pulses are recompressed back to the original temporal duration, if the bandwidth narrowing effects in the amplification process are ignored. The first and the second dispersive system are termed the stretcher and the compressor. In an ultrashort-pulse amplifier, the dispersive elements in the stretcher and the compressor are usually diffraction gratings. Grating based stretchers and compressors provide large pulse stretching and compression ratio that is commonly required in CPA. Moreover, grating based compressors are able to withstand the peak power in a high-energy system. For Ti:sapphire-based laser systems, CPA is suitable for pulses with transform-limited duration of roughly above 20 fs to hundreds of femtoseconds. Effective stretching and thus peak power reduction for longer pulses with too narrow bandwidth is difficult. Simultaneously, gain narrowing also limits the bandwidth which an amplifier can support.

The scheme of the CPA system used in this thesis is shown in Fig. 2.5. The oscillator is a Vitara Ti:sapphire Kerr-lens mode-locked oscillator from Coherent Inc., which delivers 15 fs pulses at 80 MHz repetition rate and an average output power of  $\sim 450$  mW. The pulses from the oscillator are split into two parts. The portion of the beam with lower energy is used for the CEP measurement and control system, which will be described later. Most of the pulse energy is sent as seed into the CPA system. The pulses are first stretched to longer than 1 ps by propagating through a grating stretcher. Then the stretched pulses are amplified within 14 round-trips in the regenerative amplifier. The Pockels cell allows only one pulse out of every 26664 pulses enter the regenerative amplifier, which decreases the repetition rate of the laser pulses from 80 MHz to 3 kHz. The regenerative amplifier is equipped with two Pockels cells rather than only one as shown in Fig. 2.3. The two-Pockels-cell configuration prevents the input beam and the output beam of the regenerative amplifier from overlapping with each other.

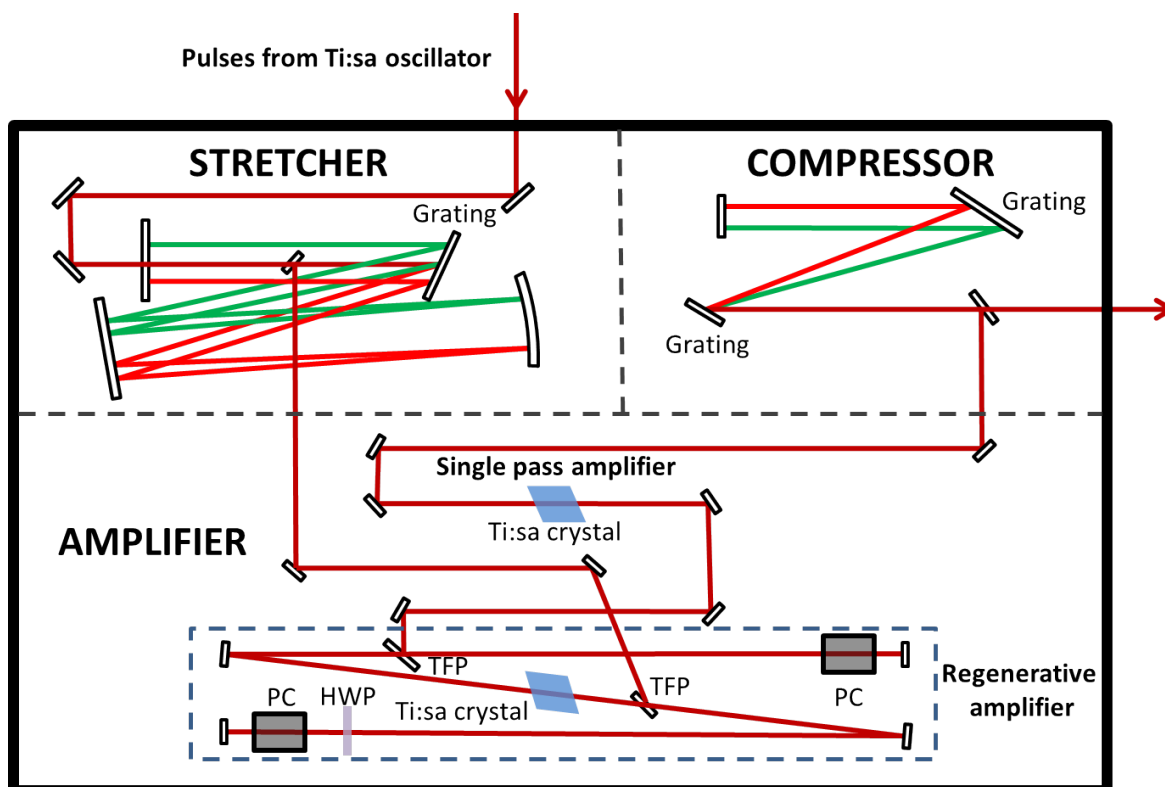


**Fig. 2.5** Schematic of the CPA system. The seed pulses from the Ti:sapphire laser oscillator are sent into the CPA system. The pulses are first stretched to longer than 1 ps by propagating through a grating stretcher. The stretched pulses then travel 14 round-trips through the regenerative amplifier. The regenerative amplifier is equipped with two Pockels cells, which separate the beam path of the input pulses and the output pulses. After the regenerative amplifier, the pulse energy is further amplified to more than 6 mJ by a single-pass amplifier. After compression, the pulse duration is 35 fs and the pulse energy is 5 mJ. The pump laser beam path is not shown in the figure. HWP: Half waveplate, PC: pockels cell, TFP: thin film polarizer.

After the regenerative amplifier, the pulse energy is further amplified to more than 6 mJ by a single-pass amplifier. The gain crystals in both amplifiers are thermoelectrically cooled to  $-10^\circ\text{C}$ . After the compressor, the pulse duration is compressed to 35 fs and the pulse energy is 5 mJ.

## 2.2 Carrier-envelope phase stabilization

The electric field of an optical pulse can be described as the product of a fast sinusoidal oscillating carrier wave and a slowly varying envelope function. The carrier-envelope phase (CE phase or CEP) of a pulse is the difference between the peak of the carrier wave and the peak of the pulse electric-field envelope, as shown in Fig. 2.6. As a result, the electric field  $e(t)$  of a laser pulse can be written as

$$e(t) = A(t) \cos(\omega_0 t + \varphi_{CE}) \quad (2.1)$$

where  $A(t)$  is the pulse envelope function,  $\omega_0$  is the carrier angular frequency and  $\varphi_{CE}$  is the CE phase. For Gaussian pulses with peak amplitude of the field  $A_0$  and FWHM pulse duration  $\tau$ ,

$$A(t) = A_0 e^{-2\ln(2)\frac{t^2}{\tau^2}} \quad (2.2)$$

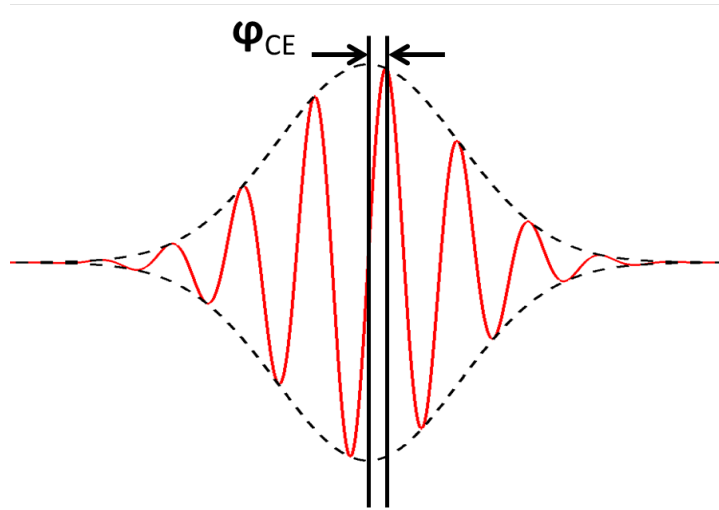


**Fig. 2.6** Definition of CEP  $\varphi_{CE}$ . The CEP  $\varphi_{CE}$  is the phase difference between the envelope (black dashline) and the carrier wave (red line)

Strong-field phenomena such as high harmonic generation (HHG) and above threshold ionization (ATI) are extremely sensitive to the shape of the electric field. Pulses with the same

electric field envelope but different CE-phases have different electric field shapes as shown in Fig. 2.7. The situation becomes significant when few-cycle pulses are concerned. Thus, in the case of isolated attosecond pulse generation via HHG, for which few-cycle pulses are usually used, CEP control is crucial.

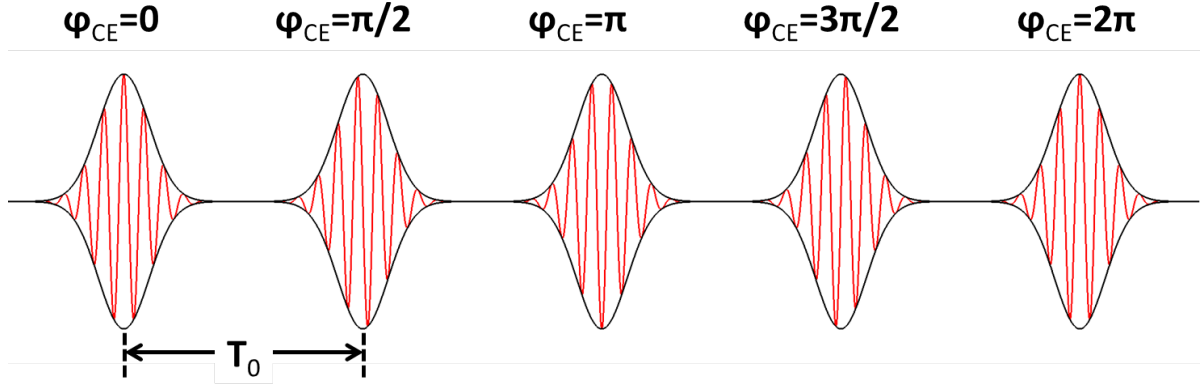


**Fig. 2.7** Electric fields of laser pulses with different CE-phases

Typically, the CEP of pulses from a mode-locked oscillator changes from one pulse to the other. Here we look at the physical origin of this CEP variation. The derivation mainly follows reference [39, 40]. The laser pulse is expressed by Eq. (2.1) and propagate along the  $z$  direction and we have the electric field at  $z$  given by

$$e(z, t) = A\left(t - \frac{z}{v_g}\right) \cos\left[\omega_0\left(t - \frac{z}{v_p}\right) + \varphi_{CE}\right] \quad (2.3)$$

It states that the envelope travels with group velocity  $v_g$  and the carrier wave travels with phase velocity  $v_p$ . In a reference frame which moves together with the pulse envelope,

$$t' = t - \frac{z}{v_g} \quad (2.4)$$

the electric field can be written as

$$e(z, t') = A(t') \cos\left[\omega_0 t' + \omega_0\left(\frac{z}{v_g} - \frac{z}{v_p}\right) + \varphi_{CE}\right] \quad (2.5)$$

as a result, we can see that the  $\varphi_{CE}$  at  $z$  is

$$\varphi(z) = \omega_0\left(\frac{z}{v_g} - \frac{z}{v_p}\right) + \varphi_{CE} \quad (2.6)$$

and the  $\varphi_{CE}$  drift due to propagation is

$$\Delta\varphi_{CE} = \omega_0 \left( \frac{1}{v_g} - \frac{1}{v_p} \right) z \quad (2.7)$$

This states that the CEP drift is due to the difference between the phase velocity and the group velocity in dispersive materials. For pulses propagating in vacuum, where  $v_g = v_p$ , the CEP of pulses stays constant.

The output of a mode-locked oscillator forms a pulse train. The pulses separation equals to the round-trip time in the resonator  $T_0$ . Assuming the variation between pulses  $\Delta\varphi_{CE}$  stays constant, the pulse train can be written as

$$e(t) = \sum_{m=-\infty}^{+\infty} a(t - mT_0) e^{i[\omega_0(t - mT_0) + m\Delta\varphi_{CE} + \varphi_0]} \quad (2.8)$$

where  $\varphi_0$  is the common phase term for all the pulses in the pulse train. It is instructive to look at the mode-locked pulse train in the frequency domain. Considering a pulse train with bursts separated by  $T_0$  in time, it is natural to anticipate that the spectrum of the pulse train consists of a frequency comb with comb line separation equal to  $f_{rep} = 1/T_0$  which is the repetition rate of the oscillator.

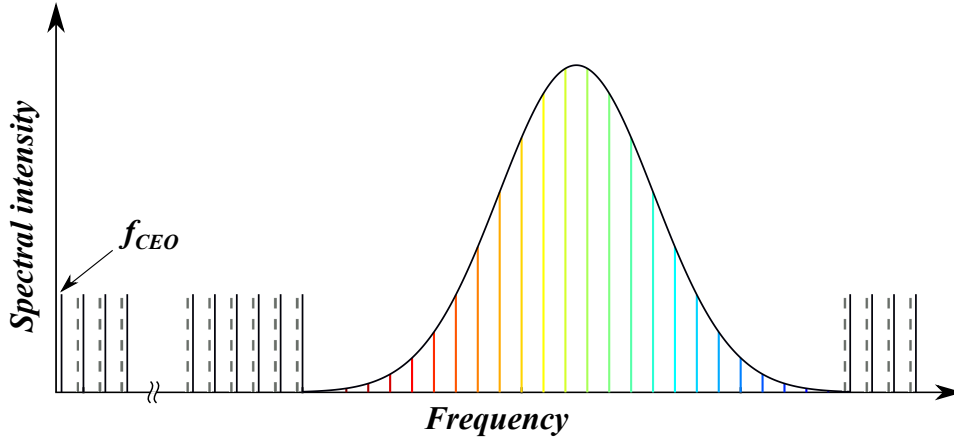


**Fig. 2.8** Frequency comb and  $f_{CEO}$ . The frequency comb lines lying inside (colored lines) and outside (black lines) the laser spectrum are shown. The "vacuum" frequency comb lines (dashed line) are shown as a reference for indicating  $f_{CEO}$

Performing a Fourier transform to the pulse train given by Eq. (2.8), we obtain [41]

$$E(\omega) = e^{i\varphi_0} \sum_{m=-\infty}^{+\infty} e^{im(\Delta\varphi_{CE} - \omega_0 T_0)} \int_{-\infty}^{\infty} a(t - mT_0) e^{-i(\omega - \omega_0)t} dt \quad (2.9)$$



by recalling the identity that

$$\int_{-\infty}^{\infty} f(x-a)e^{-i\alpha x} dx = e^{-i\alpha a} \int_{-\infty}^{\infty} f(x)e^{-i\alpha x} dx \quad (2.10)$$

then we have

$$\begin{aligned} E(\omega) &= e^{i\varphi_0} \sum_{m=-\infty}^{+\infty} e^{im(\Delta\varphi_{CE}-\omega_0 T_0)} e^{-im(\omega-\omega_0)T_0} \int_{-\infty}^{\infty} a(t)e^{-i(\omega-\omega_0)t} dt \\ &= e^{i\varphi_0} A(\omega - \omega_0) \sum_{m=-\infty}^{+\infty} e^{im(\Delta\varphi_{CE}-\omega T_0)} \end{aligned} \quad (2.11)$$

where

$$A(\omega) = \int_{-\infty}^{\infty} a(t)e^{-i\omega t} dt \quad (2.12)$$

is the Fourier transform of the envelope function  $a(t)$ . By making use of the identity

$$\sum_{m=-\infty}^{+\infty} f(x-mp) = \sum_{n=-\infty}^{+\infty} \frac{1}{p} F\left(\frac{n}{p}\right) e^{i2\pi nx/p} \quad (2.13)$$

where  $F(y)$  is the Fourier transform of  $f(x)$ , and recalling the fact that the Fourier transform of  $\delta(t)$  is a constant, we have

$$E(\omega) = e^{i\varphi_0} A(\omega - \omega_0) \sum_{m=-\infty}^{+\infty} \delta(\omega T_0 - \Delta\varphi_{CE} - 2m\pi) \quad (2.14)$$

Eq. (2.14) represents a frequency comb as shown in Fig. 2.8. The frequency spacing in this frequency comb is  $f_{rep} = 1/T_0$  as expected. The  $m$ th comb line in the frequency comb is

$$f_m = mf_{rep} + f_0 \quad (2.15)$$

where

$$f_0 = \frac{\Delta\varphi_{CE}}{2\pi T_0} \quad (2.16)$$

is called the carrier-envelope offset frequency  $f_{CEO}$ , where  $\Delta\varphi_{CE}$  is modulo  $2\pi$ . Assuming there is a cavity without dispersion, then the CEP of the pulses from this cavity would stay constant, i.e.,  $\Delta\varphi_{CE} = 0$  and  $f_{CEO} = 0$ . There is a comb line located at exactly 0 Hz. Such a "vacuum" frequency comb is also shown in Fig. 2.8 as a reference. In a real cavity, dispersion is inevitable and  $\Delta\varphi_{CE} \neq 0$ . There is an offset between the lowest comb line and 0 Hz, which is  $f_{CEO}$ . On the other hand,  $f_{CEO}$  can be regarded as the changing rate of the CE phase between pulses.

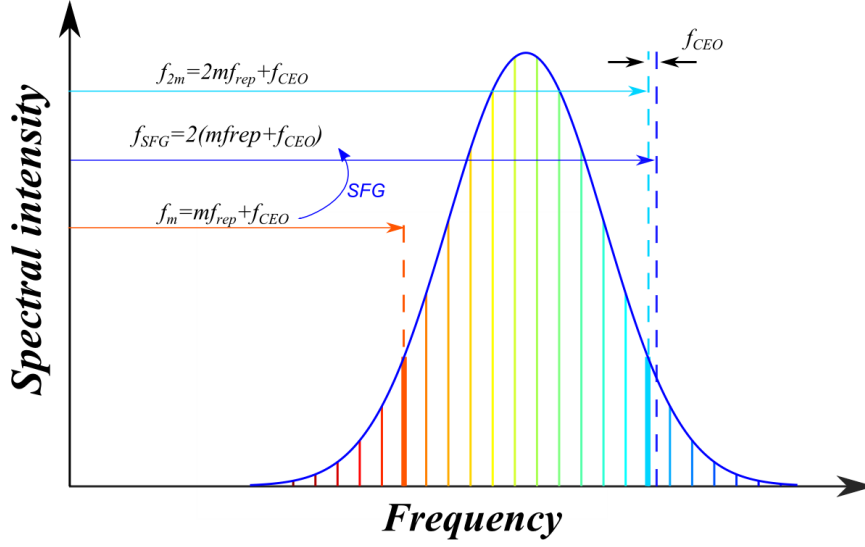


**Fig. 2.9** Principle of f-2f self-referencing interferometry

$f_{CEO}$  can be measured with a method called *f-2f self-referencing interferometry* [42–44]. The f-2f self-referencing interferometry requires the frequency comb covers at least one octave as the one shown in Fig. 2.9, which means the second harmonic of the low-frequency end of the comb will spectrally overlap with the high-frequency end of the comb. The beat note between the fundamental comb and the second harmonic comb gives the carrier envelope offset frequency,  $f_{CEO}$ . The natural but incorrect way of thinking about generating the second harmonic comb is to perform second harmonic generation on all of the comb lines. However, generating the second harmonic of a frequency comb  $f_m = mf_{rep} + f_{CEO}$  leads to a frequency comb  $f_m = 2(mf_{rep} + f_{CEO})$  which has twice the frequency spacing and corresponds to a pulse train with twice the repetition rate. The problem can be solved by noting that, for ultrashort pulses, second harmonic generation is a misnomer [41]. One is actually performing sum-frequency generation among all the frequency comb lines. The sum-frequency generation between different comb lines yields upconverted comb lines with the same frequency spacing as in the fundamental frequency comb. Eventually, the beat between the fundamental comb and the second harmonic comb is written as

$$f_{beat} = f_{SFG} - f_{2m} = 2(mf_{rep} + f_{CEO}) - (2mf_{rep} + f_{CEO}) = f_{CEO} \quad (2.17)$$

The beat frequency can be rather easily detected, while the generation of an octave-spanning frequency comb is challenging. Technical details will be covered later in this section. We know that in a real cavity, the intracavity dispersion and nonlinearities cause a slipping on the CE

phase, and it is essential to control the variation of the CE phase for attosecond experiments. CEP control can refer to two different situations. First, in the stringent sense, CEP control means the CEP of the laser pulses stays constant which is the same as saying the CEP changing rate  $f_{CEO} = 0$ . While in a less stringent situation, CEP control means controlling the changing rate of the CEP, i.e., keeping  $f_{CEO}$  constant. In general, both cases can be realized. However, fixing  $f_{CEO}$  of the laser oscillator pulses at a certain nonzero value, e.g.,  $f_{rep}/4$ , is easier to implement and sufficient for our experiment. For example, in a pulse train as shown in Fig. 2.7, the CE phase shifts by  $\pi/2$  from pulse to pulse and the CE phase repeats itself every 4 pulses. In our experiment, we use the pulses from the amplifier, which has a much lower repetition rate than the oscillator. A pulse picker can be used to select the pulses with the same CE phase for amplification and ignore the pulses with different CE phase. Notice that it has been mentioned above, the repetition rate has decreased by 26664, which is an integer multiple of 4!

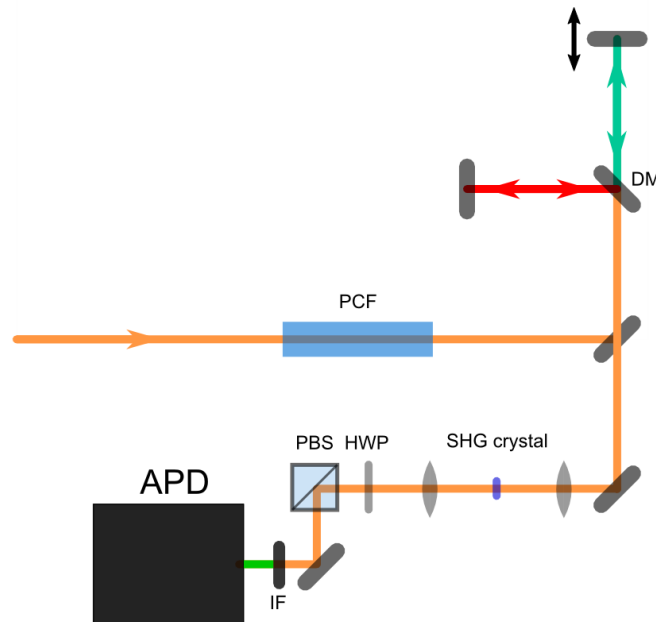


**Fig. 2.10** Schematic of f-2f interferometry setup for  $f_{CEO}$  measurement of the oscillator pulses. PCF: Photonic crystal fiber, DM: Dichroic mirror, HWP: Half waveplate, PBS: Polarizing beam splitter, IF: Interference filter, APD: avalanche photodiode

The scheme of a typical f-2f self-referencing interferometry setup to measure  $f_{CEO}$  is shown in Fig. 2.10. Notice that the spectrum from the laser oscillator does not have broad enough bandwidth for an f-2f measurement. The required octave-spanning spectrum is generated by sending a small portion of the pulse in a piece of photonic crystal fiber (PCF). The CEP of the pulses is not affected by the spectral broadening. After spectral broadening, the beam is sent into a Michelson interferometer. The beam is first split by a dichroic mirror. The two portions

of the beam with different frequencies are then recombined. In order to frequency double the long-wavelength components, the beam is then focused down into a nonlinear crystal for second harmonic generation. Since type-I phase matching is used in the setup, the polarization plane of the fundamental beam and the frequency-doubled beam is orthogonal. A half waveplate and a polarizing beamsplitter are used after the SHG crystal to optimize the beating signal. The temporal delay between the two pulses is controlled with a movable mirror in the interferometer. A bandpass interference filter (centered at 532 nm) in front of the avalanche photodiode (APD) which detects the weak filtered light. The beat signal, i.e.,  $f_{CEO}$ , can be extracted from the measured APD signal as RF signal.

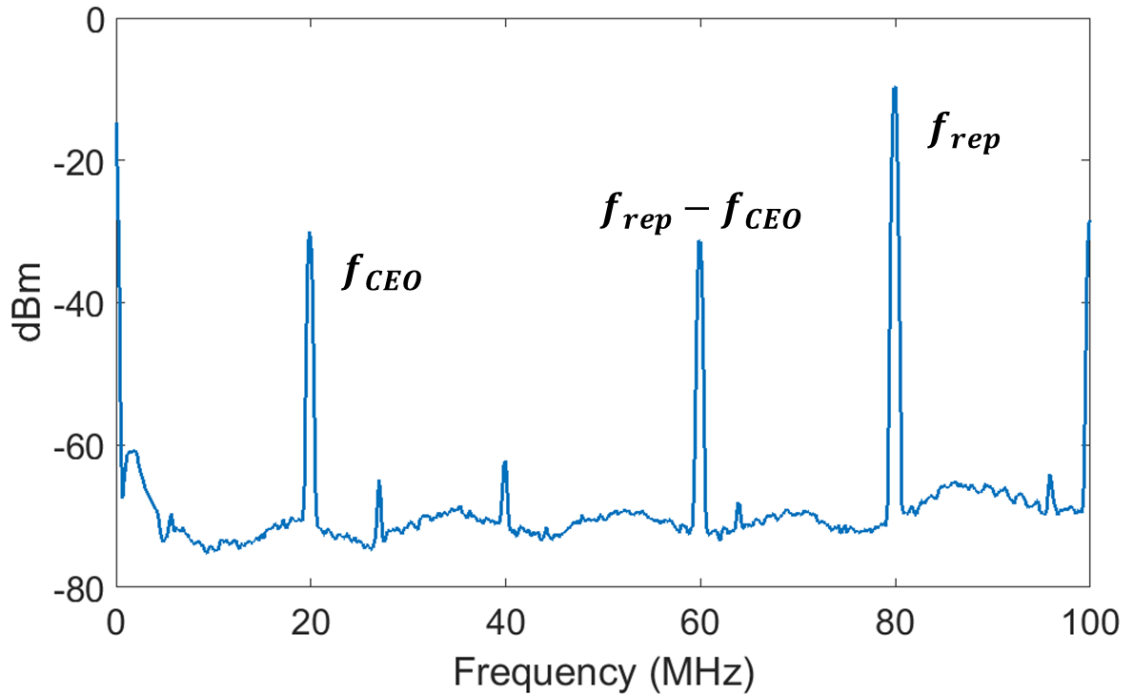


**Fig. 2.11** The  $f$ - $2f$  beat signal monitored with an RF spectrum analyzer. The three highest peaks from left to right are: the carrier-envelope offset frequency  $f_{CEO}$  which is locked to  $1/4$  of the repetition rate  $f_{rep}$ ,  $f_{rep} - f_{CEO}$ , and the repetition rate  $f_{rep}$  which is located at 80 MHz.

After  $f_{CEO}$  is measured, a feedback loop is implemented to phase-lock it to a certain reference value. In the laboratory,  $f_{CEO}$  is locked to  $f_{rep}/4$  and a pulse train looking like the one in Fig. 2.7 is produced. First, the APD signal is fed into a commercial phase-locking system from Menlo Systems. The electronics extracts the  $f_{CEO}$  signal from the APD signal. Meanwhile, the repetition rate of the oscillator  $f_{rep}$  is monitored with another photodiode. The repetition rate signal is also fed into the phase-locking electronics and divided by 4. A phase detector in the locking electronics compares the phase of these two signals,  $f_{CEO}$  and  $f_{rep}/4$ ,

and generates an error signal which is proportional to the phase difference. The error signal is then fed into a proportional-integral controller (PI controller). The output from the PI controller modulates the pump power of the laser oscillator by means of an acousto-optic modulator (AOM) to minimize the phase difference and thus locks  $f_{CEO}$  to  $f_{rep}/4$ . The repetition rate and the beat signal are monitored for system diagnostics with an RF spectrum analyzer as shown in Fig. 2.11. Here, the practical reason of setting  $f_{CEO} = f_{rep}/4$  is that this frequency is far away from DC and  $f_{rep}$  also does not overlap with  $f_{rep} - f_{CEO}$ .

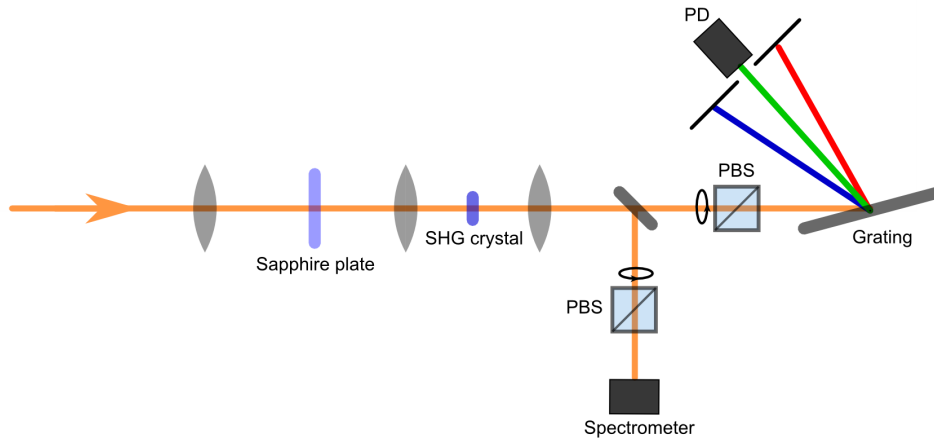


**Fig. 2.12** Schematic of f-2f interferometry setup for  $\varphi_{CE}$  measurement of the amplified pulses. PBS: Polarizing beam splitter, PD: photodiode

Even if the CE-phase of the oscillator pulses is controlled, the CE-phase stability of the pulses after the amplifier can be deteriorated. There are many factors that can negatively influence the CE phase of the amplified pulses, e.g., the thermal drift of the gain medium, pump intensity fluctuations, and vibrations of the gratings in the stretcher/compressor. In order to obtain amplified pulses with constant CE phase, the CE phase drift must be measured and compensated. The same method, f-2f self-referencing interferometry, is used for measuring the CE phase of the amplified pulses. The scheme of the f-2f setup for the amplified pulses is shown in Fig. 2.12. Different from the case used for the oscillator pulses, it is possible to measure the single-shot CE phase variation for the amplified pulses due to the low repetition rate. Meanwhile, the bandwidth of the amplified pulses is not broad enough to directly apply f-2f interferometry method either. Since the amplified pulses are very energetic, a portion of the beam (<2%) is focused into bulk material, in our case a sapphire plate, rather than PCF, to broaden the spectrum in a filament to cover more than one octave. The spectrally broadened beam is then refocused into a type-I BBO for second harmonic generation. As before, the polarization of the fundamental beam and the frequency-doubled beam is orthogonal. A polarizer is again used to project the polarization to a common plane from both beams and allow

them to interfere. Since, in the supercontinuum generation process, the blue end of the spectrum is delayed with respect to the red end, the blue end of the spectrum is also delayed with respect to the second harmonic of the red end of the spectrum. As a result, with a spectrometer, spectral interference fringes can be observed in the spectral region where fundamental spectrum and the second harmonic spectrum overlaps.

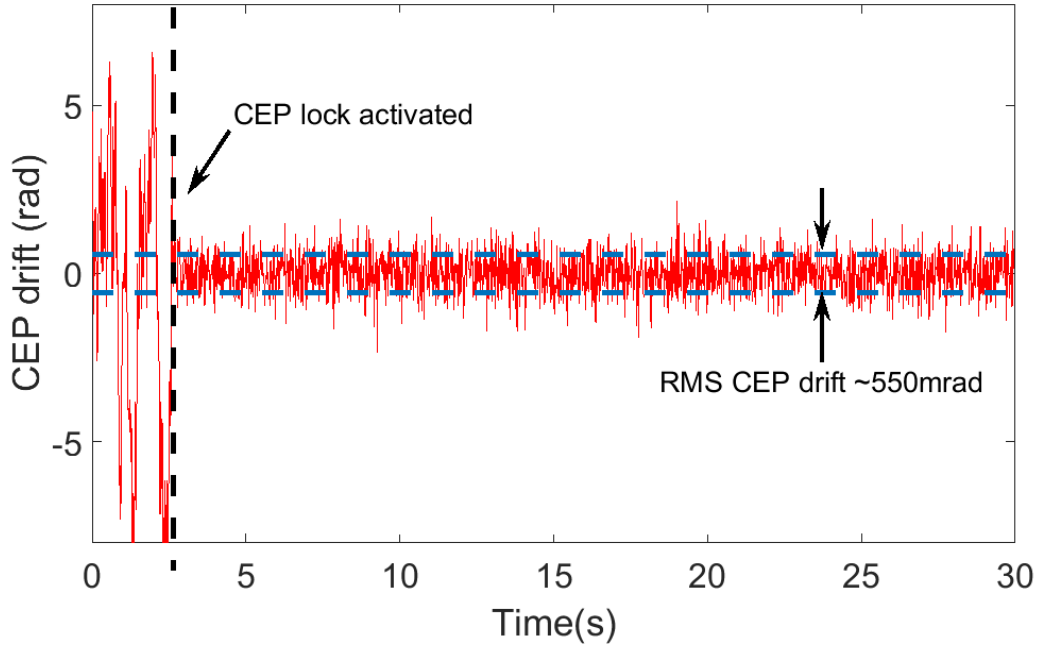


**Fig. 2.13** CEP drift when both fast and slow CEP stabilization loops running. The CEP lock is activated at the point marked with a vertical dashed line. It can be seen that the CEP drift decreases significantly when the CEP is locked. The CEP drift is  $\sim 550$  mrad RMS when the CEP lock is activated. The boundaries of  $\pm$ RMS CEP drift are marked as dashed lines in the figure.

The electric field of the fundamental beam and the frequency-doubled beam can be written in the frequency domain as

$$E_f(\omega) = \sqrt{I_f(\omega)} e^{i(\varphi_f(\omega) + \varphi_{CE})} \quad (2.18)$$

$$E_{2f}(\omega) = \sqrt{I_{2f}(\omega)} e^{i(\varphi_{2f}(\omega) + \varphi_{CE} + \omega\tau_g)} \quad (2.19)$$

where  $I_f$ ,  $I_{2f}$  is the intensity of the fundamental beam and the frequency-doubled beam, respectively.  $\tau_g$  is the delay between the second harmonic of the red end of the spectrum and the blue end of the spectrum. The two beams interfere and the signal detected by the spectrometer

is

$$\begin{aligned} S(\omega) &= |E_f(\omega) + E_{2f}(\omega)|^2 \\ &= I_f(\omega) + I_{2f}(\omega) + \sqrt{I_f(\omega)I_{2f}(\omega)} \cos(\varphi_{2f}(\omega) - \varphi_f(\omega) + \varphi_{CE} + \omega\tau_g) \end{aligned} \quad (2.20)$$

From the spectral interference fringes, the overall phase can be extracted which is written as

$$\varphi(\omega) = \varphi_{2f}(\omega) - \varphi_f(\omega) + \varphi_{CE} + \omega\tau_g \quad (2.21)$$

When the variation of  $\varphi_{2f}(\omega) - \varphi_f(\omega)$  and  $\tau_g$  is negligible, the variation of the CE phase  $\Delta\varphi_{CE}$  equals to the variation of the overall phase  $\Delta\varphi(\omega)$ , which is given by

$$\Delta\varphi_{CE} = \Delta\varphi(\omega) \quad (2.22)$$

The measured  $\Delta\varphi_{CE}$  is used as an error signal to actively stabilize the CE phase-variation originating from the amplification system. In the implementation of our setup, however, the intensity variation of one spectral component rather than the whole spectrum is monitored with a photodiode. Assuming that the intensity variation of both the fundamental and frequency-doubled beam is small, the intensity variation of one spectral component reflects the variation of the CEP. The spectrometer shown in Fig. 2.12 is not part of the feedback loop but merely for out-of-loop CEP monitoring.

Notice that the grating separation in the stretcher and the compressor has influence on the CE phase. We can therefore control the separation of the gratings to compensate the CE phase fluctuation. In general, either the stretcher or the compressor can be used as part of the CE phase stabilization feedback loop. In our system, the feedback loop controls the grating in the stretcher. Compared to the compressor, the grating in the stretcher is smaller and thus allows higher feedback bandwidth. The CE phase variation due to the variation of the effective grating separation  $\Delta l_{eff}$  in the stretcher is [45]

$$\Delta\varphi_{CE} = 2\pi \sin(\gamma) \frac{\Delta l_{eff}}{d} \quad (2.23)$$

where  $\gamma$  is the incident angle and  $d$  the grating constant. The whole CE phase feedback system consists of a fast loop acting on the laser oscillator and a slow loop acting on the amplifier. The slow CEP drift monitored by the spectrometer in Fig. 2.12 is shown in Fig. 2.13. When both fast and slow CEP stabilization loops are activated, the CEP drift decreases significantly. The RMS CEP drift is  $\sim 550$  mrad which means the CEP control system currently does not perform as expected from the specifications achieved during installation of the laser system.

However, as we will see, the CEP effect on the HHG spectrum can still be clearly observed in experiments. The HHG results are shown in the next chapter.

## 2.3 Hollow core fiber compressor

The duration of the pulses from the CPA system is approximately 35 fs. These pulses are usually too long for direct isolated attosecond pulse generation. Indeed, it has been demonstrated that pulses with duration of tens of femtoseconds can be used to produce isolated attosecond pulses (IAPs) by employing gating methods, which will be introduced in *Chapter 2*. However, in isolated attosecond pulse generation, there is effectively only less than one cycle of the laser pulse significantly contributing to the XUV generation. The longer the pulses, the lower the efficiency. For isolated attosecond pulse generation, energetic few-cycle pulses are preferred. A noble gas filled hollow-core fiber compressor is the standard method to produce few-cycle pulses with pulse energy up to a few mJs. The pulses are first spectrally broadened in the noble gas and then recompressed with chirped mirrors.

A hollow-core fiber is a glass capillary with inner diameter of a few hundred micrometers, which is much larger than visible wavelengths. Unlike a typical optical fiber, in which the refractive index of the core material is larger than that of the cladding material, the modes in hollow-core fibers are lossy. After propagation in hollow-core fibers with sufficient length, only the mode with the lowest loss remains. Linear propagation in hollow dielectric waveguides with diameters much larger than the wavelength was studied thoroughly in Ref. [46]. The mode with lowest loss is the  $EH_{11}$  mode. The intensity profile of this mode is

$$I(r) = I_0 J_0^2 \left( 2.405 \frac{r}{a} \right) \quad (2.24)$$

where  $I_0$  is the peak intensity,  $J_0$  is the zero-order Bessel function, and  $a$  is the core radius.

The hollow-core fiber is filled with noble gas as nonlinear medium for spectral broadening. Noble gases have high ionization potential which allows them to withstand large laser intensity before multiphoton ionization happens. The dominating nonlinear effect involved in the process is a pure third-order nonlinear effect. The strength of the nonlinearity can be controlled by varying the gas pressure and using different gas species.

Different frequency components experience large group-delay dispersion (GDD) after propagation in the noble gas. The uncompressed HCF output pulse duration is on the order of hundreds of femtoseconds. The dispersion must be compensated to obtain short pulses, for that various methods are available: double chirped mirrors (DCMs), prism compressors or a



spatial light modulator (SLM). A pulse compression scheme based on DCMs is adopted in our experiments.

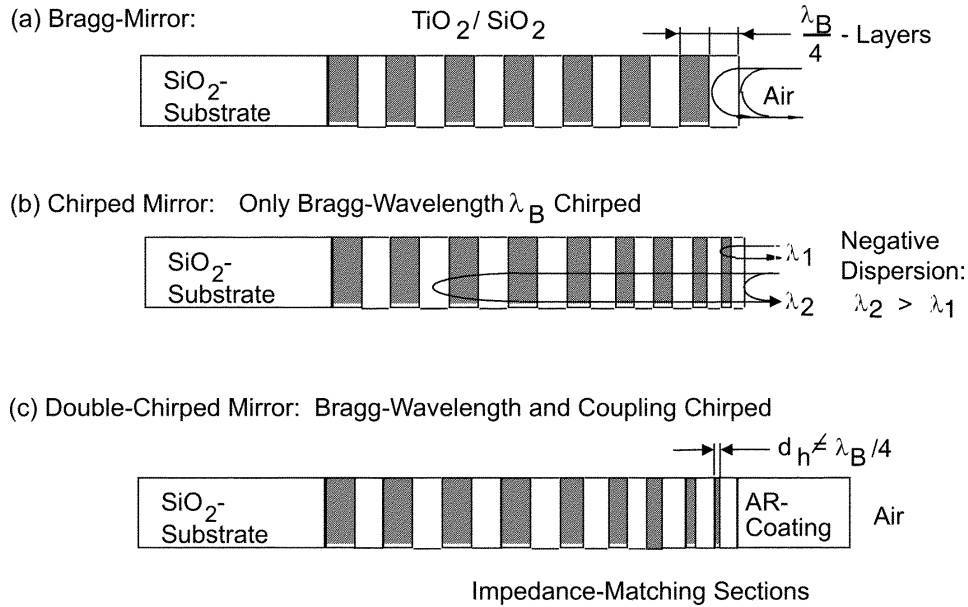


**Fig. 2.14** Illustration of principle of double chirped mirrors.(a) standard Bragg-mirror. (b) chirped mirrors. The Bragg wavelength varies in the structure. (c) double chirped mirrors. Figure adopted from [47][2003]IEEE

A chirped mirror is a dielectric dispersive mirror, which is based on a special multi-layer coating design, as shown in Fig. 2.14. The Bragg wavelength varies within the coatings. The red end of the spectrum penetrates deeper into the coating than the blue end. This means that the low-frequency components experience a longer optical path than the high-frequency components, and thus a negative chirp is imposed onto the pulse. However, this simple idea does not work perfectly in practical applications. The reflections from a chirped mirror based on this simple design would exhibit strong group delay (GD) oscillations which originates from Gires-Tournois interferences. First, the partial reflection from the front section of the mirror and the reflection of the back section of the mirror form an effective Gires-Tournois Interferometer. This is solved by varying the duty cycle, which is the ratio of the optical thickness of the high and low refractive-index layers. Second, the Fresnel reflection on the front surface of the mirror also introduces a Gires-Tournois effect. An anti-reflection (AR) coating is added to tackle the second problem. The chirped mirrors with these new designs are termed double-chirped mirrors (DCMs) [48]. These two modifications make the double-chirped mirrors a practical tool for precise dispersion management. The size of the GD oscillation is proportional to the residual reflectivity of the AR coating. To achieve small enough GD oscillations and thus satisfying performance, the residual reflectivity of the AR coating has to be sufficiently low.

However, AR coating with sufficiently low residual reflectivity is almost impossible when an octave-spanning spectrum is considered. However, two DCMs with proper complementary design can have counteracting group-delay oscillations. The resultant GD oscillations from the DCM pair is proportional to the square of the residual reflectivity of the AR coating [49]. DCM pairs allow one to achieve precise dispersion compensation for ultrabroadband spectra.

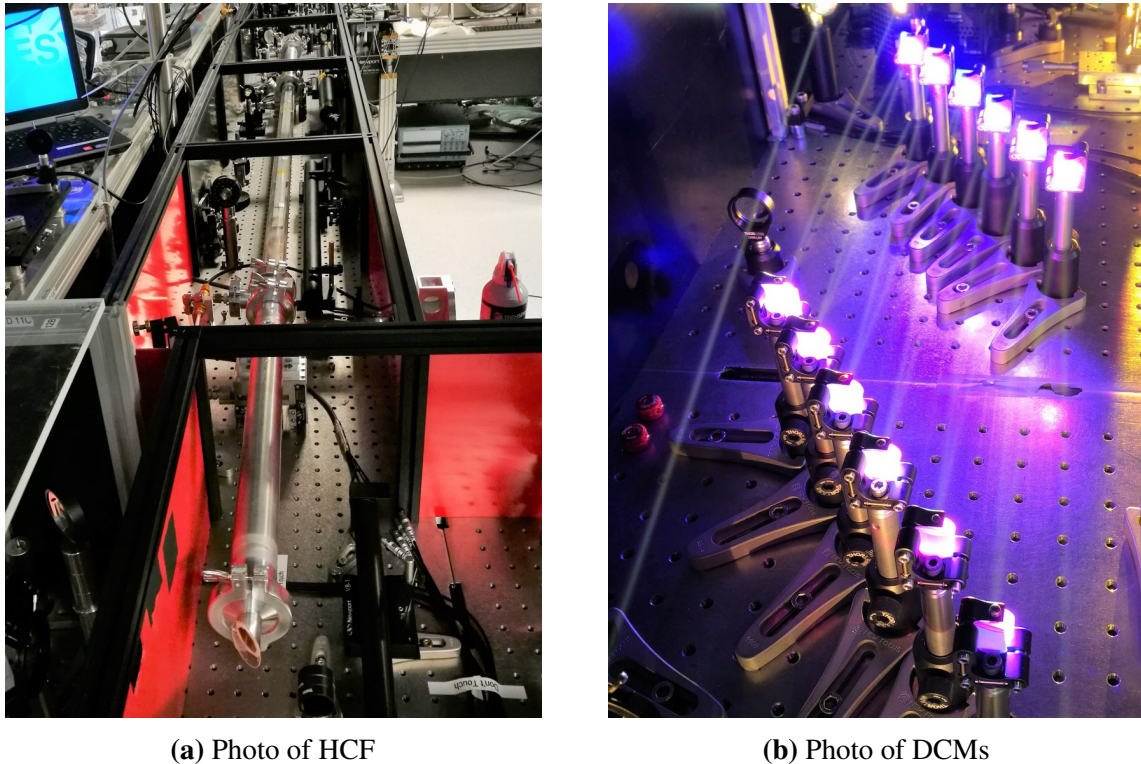


**Fig. 2.15** Photo of HCF compressor

The hollow-core fiber used in our experimental setup is 1 m long and the core diameter is  $400\ \mu\text{m}$ . Only about half of the CPA output energy,  $\sim 2.1\ \text{mJ}$ , is fed into the HCF compressor. This is the maximum energy still free of multiphoton ionization. The CPA pulses are focused with a lens of 1.5-m focal length and coupled into the hollow-core fiber. The fiber is placed on a supporting steel bar with a V-groove to prevent any bending of the fiber itself. The fiber and its holder are placed inside a sealed tube filled with 2.6 bar of neon gas. The input and output windows are both used at Brewster's angle to avoid reflection losses. Since the energy transmission and the output spectrum of the HCF are both sensitive to the coupling condition, the pointing of the input beam to the HCF must be stabilized. A beam-pointing stabilization system from MRC Systems GmbH has been implemented for this purpose. The tube housing the fiber is placed on two precisely adjustable and stable 2D translation stages. Due to the fact that the beam pointing does not necessarily recover to the same position on each on-off cycle

of the beam pointing system, the translation stages are for the fiber position fine adjustment for optimizing the parameters of the fiber output, like spectral shape, stability, compression, etc.

At the HCF output, the laser spectrum is drastically broadened compared to the input spectrum as shown in Fig. 2.16. The spectrum covers from 400 nm to 1000 nm, which is more than one octave of spectral bandwidth. The input pulse energy is 2.1 mJ and the output pulse energy is 1.05 mJ. The HCF is filled with 2.6 bar of neon gas as nonlinear medium.

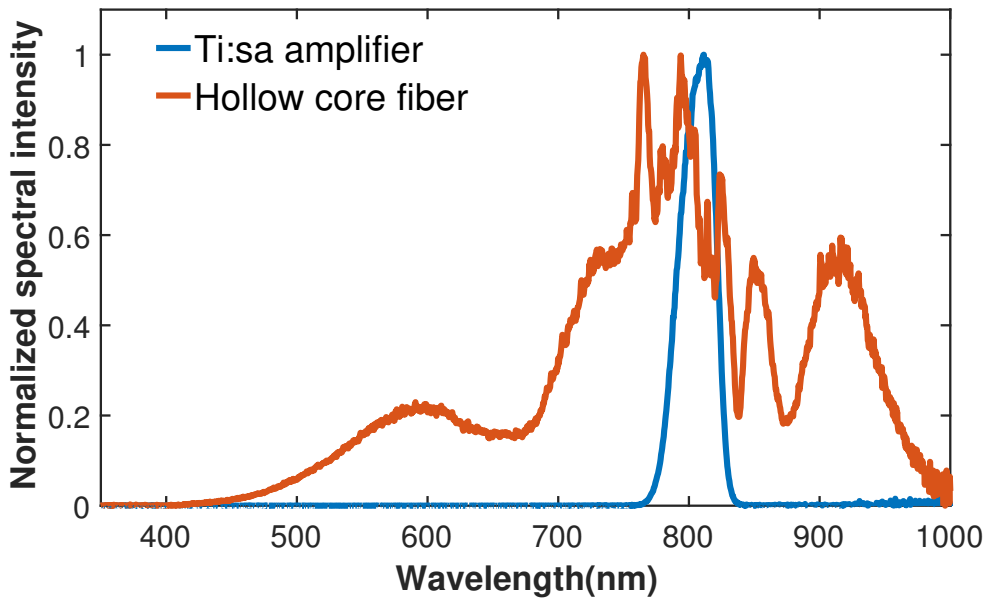


**Fig. 2.16** HCF input and output spectra. Both spectra are measured with an USB2000 spectrometer from OceanOptics. The spectrum is corrected for the wavelength dependent response of the detector. The noisy looking spectral part in the long wavelength region ( $>980$  nm) is due to the low detection efficiency in that spectral region. The input pulse duration is  $\sim 35$  fs, the pulse energy is 2.1 mJ. The output pulse energy from the HCF is 1.05 mJ. The HCF is filled with 2.6 bar of neon gas.

As mentioned above, the nonlinearity for spectral broadening and thus the HCF output spectral shape and bandwidth can be controlled by varying the gas pressure along other degrees of freedom. In Fig. 2.17, the dependence of the spectral bandwidth on gas pressure is shown. Neon gas is used as the nonlinear medium and the pressure varies from 200 mbar to 1800 mbar. As the gas pressure increases, the HCF output spectrum bandwidth increases. However, there is also an upper limit on the gas pressure. When the gas pressure is larger than the upper limit, too much nonlinearity is introduced in the pulse propagation and thus the output beam profile is too distorted for experimental applications.

The output pulses are then compressed with DCM pairs. The custom-designed DCMs employed in our setup have a bandwidth of 500-1000 nm and GDD of  $-50$  fs<sup>2</sup>. It takes 5 bounces off the DCM pairs, which is in total 10 reflections, to compensate the dispersion of

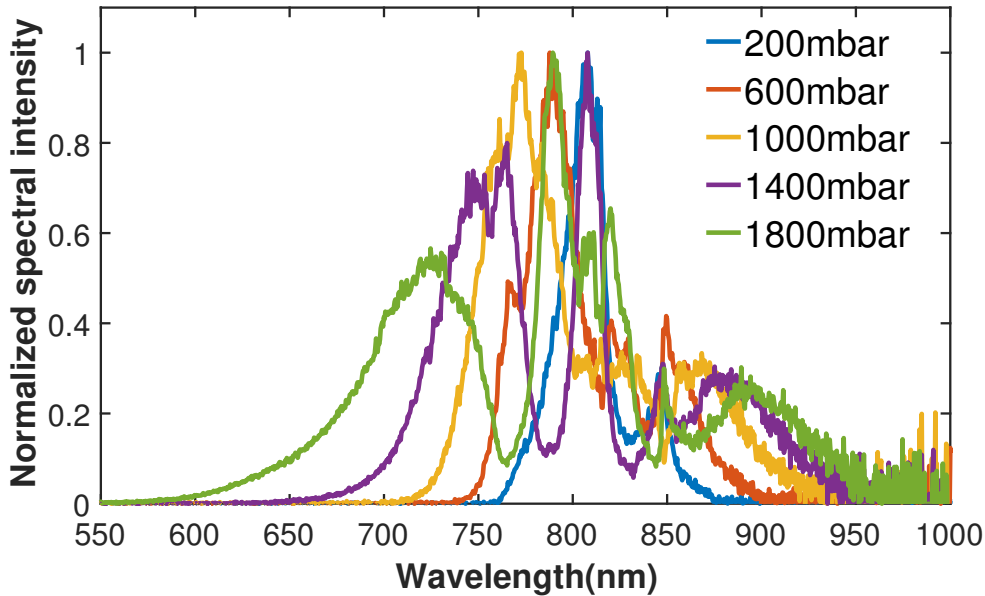


**Fig. 2.17** HCF output spectrum vs pressure. The spectra are measured directly at the hollow-core fiber output. Neon is used as the nonlinear medium. All the spectra are measured with an USB2000 spectrometer from OceanOptics. The spectrum is corrected for the wavelength dependent response of the detector.

the HCF output pulses. Meanwhile, as shown in Fig. 2.15b, two more reflections on the DCM pairs are needed to compensate the dispersion of a pair of fused silica wedges and the vacuum chamber's input window which is a fused silica window of 1 mm thickness. The fused silica wedges are for precise dispersion compensation and also for tuning the pulse CEP. With this configuration, the pulses are compressed to the minimum duration in the HHG gas target.

As discussed in the next section, the recompressed pulse duration was characterized by SHG-FROG to be  $\sim 5.3$  fs. Thus, the HCF compressor indeed delivers few-cycle pulses. Usually, it is instructive to calculate the transform-limited (TL) pulse duration with the pulse spectrum since the TL pulse duration is a good reference for determining whether the pulse compression is carried out properly. The TL pulse duration calculated with the HCF compressor output spectrum is  $\sim 3$  fs which significantly differs from the measured value. However, the TL pulse duration calculated with the entire spectrum is misleading since the reflection bandwidth of the DCMs is broader than the dispersion compensation bandwidth of the DCMs. The TL pulse duration from the entire spectrum is longer than the pulse duration that can be achieved after pulse compression with our DCM pairs. In our experiments, the reflectivity bandwidth of the DCMs covers the entire HCF output spectrum ranging from 400 nm to 1000 nm. In contrast, only part of the spectrum, roughly ranging from 500 nm to 1000 nm, is effectively compressed by the DCMs. To distinguish the compressed portion of the spectrum from the

uncompressed portion, one has to measure the spectral phase of the pulse which means one has to perform a full pulse characterization. Ultrashort-pulse characterization methods will be discussed in the next section. The TL pulse duration of our HCF compressor can be better estimated with the FROG reconstructed pulse spectrum in which only the compressed portion of the HCF compressor output spectrum appears. The TL pulse duration calculated from the FROG reconstructed pulse spectrum is  $\sim 4.3$  fs which is closer to the measured value.

## 2.4 Few-cycle pulse characterization

Pulse characterization means measuring the variation of electric field in amplitude and phase versus time. Different methods have been applied for pulse characterization over the years. Pulses with durations as short as 10 ps can be measured directly with fast photodiodes. While for pulses with shorter duration, electronic devices are too slow. Although streak cameras can be used to measure pulses down to few hundreds of femtoseconds, it is still not sufficient for characterizing few-cycle pulses. The three most often used methods of ultrafast pulse characterization are autocorrelation techniques, which do not yield the phase, spectral phase interferometry for direct electric field reconstruction (SPIDER) [50] and frequency-resolved optical gating (FROG) [51]. Measurement of the complex spectrum means that both the spectral amplitude and the spectral phase must be determined. The square of spectral amplitude, i.e., the spectral intensity, can be measured directly with an optical spectrometer. Both FROG and SPIDER aim to measure the spectral intensity and phase. SPIDER is based on Fourier transform spectral interferometry. The main idea behind FROG is that a short gate pulse can be used to sample another long pulse. When measuring ultrashort pulses, the pulse is used as the gate pulse to sample itself. Either of the two methods has its own advantages and disadvantages. SHG-FROG is used here for characterizing our few-cycle pulses and will be described in detail. This description also helps understand the concept of attosecond pulses characterization, which shares common ideas as FROG. This attosecond pulses characterization method will be introduced in *Chapter 4*.

### 2.4.1 Field autocorrelation and intensity autocorrelation

FROG can be regarded as a spectrally-resolved extension of the well-established autocorrelation techniques. As a result, it is helpful to briefly review some related concepts before introducing FROG. In optics, various autocorrelation functions can be realized experimentally. The most basic one is the field autocorrelation. Assuming a complex electric field  $e(t)$ , the field

autocorrelation function is defined as

$$G_1(\tau) = \int_{-\infty}^{+\infty} e(t)e(t-\tau)dt \quad (2.25)$$

Experimentally, this can be realized by sending the pulse under test in a Michelson interferom-

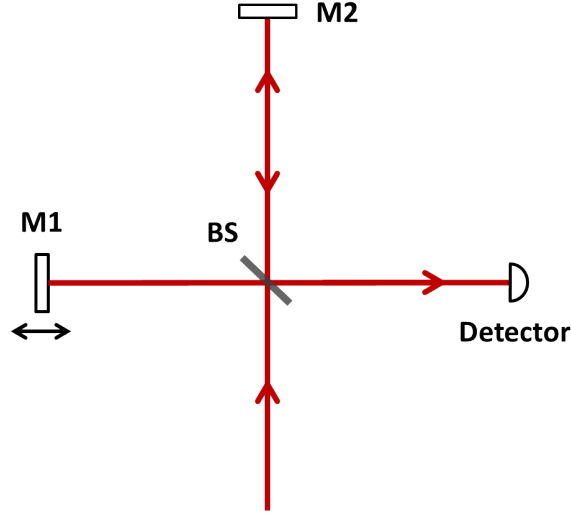


**Fig. 2.18** Schematic of field autocorrelation measurement setup

eter. A detector is placed at the output of the interferometer. One mirror in the interferometer is used to control the delay  $\tau$  between two pulse interferometric replicas. The experimental setup scheme is shown in Fig. 2.18. The detector is slow compared to the pulse, so the output signal of the detector is proportional to the time-averaged power

$$I_1(\tau) = \int_{-\infty}^{+\infty} |e(t) + e(t-\tau)|^2 dt \quad (2.26)$$

it is straightforward to verify that one of the terms in  $I_1(\tau)$  is the field autocorrelation  $G_1(\tau)$ . However, it can be proven that the field autocorrelation is merely the reverse Fourier transform of the input pulse power spectrum which means that measuring the field autocorrelation is equivalent to measuring the pulse power spectrum. The field autocorrelation does not allow to measure the pulse duration and it does not provide information about spectral phase of the input pulses.

Another autocorrelation function, the intensity autocorrelation, is defined as

$$G_2(\tau) = \int_{-\infty}^{+\infty} I(t)I(t-\tau)dt \quad (2.27)$$



in which  $I(t) = |e(t)|^2$ . The intensity autocorrelation can be measured experimentally with the scheme shown in Fig. 2.19. A pulse is split into two delayed replicas and then focused into a SHG crystal. The detector measures the signal

$$I_2(\tau) = \int_{-\infty}^{+\infty} |e(t)e(t-\tau)|^2 dt = \int_{-\infty}^{+\infty} I(t)I(t-\tau)dt \quad (2.28)$$

which is exactly the intensity autocorrelation  $G_2(\tau)$ . When the delay is much longer than the pulse duration,  $G_2(\tau)$  becomes zero. As a result, the width of the intensity autocorrelation provides some but incomplete information on the pulse duration. Meanwhile, the intensity autocorrelation is an even function of  $\tau$  regardless of the actual pulse shape. One cannot recover unique pulse shape from  $G_2(\tau)$ . Asymmetric autocorrelation shapes may indicate systematic error in the measuring process. Noted that the Fourier transform of  $\mathcal{F}[G_2(\tau)] \propto |\tilde{I}(\omega)|^2$ , where  $\tilde{I}(\omega)$  is the Fourier transform of  $I(t)$ . If  $I(t)$  is symmetric,  $\tilde{I}(\omega)$  must be real. Therefore,  $\tilde{I}(\omega)$  can be obtained by taking the square root of  $|\tilde{I}(\omega)|^2$ . However, if there is no prior knowledge about  $I(t)$ ,  $\tilde{I}(\omega)$  cannot be assumed to be real. As a result,  $G_2(\tau)$  only gives  $|\tilde{I}(\omega)|$  but no information on the phase. Intensity autocorrelation measurement cannot be used to fully reconstruct the pulse profile  $I(t)$ .

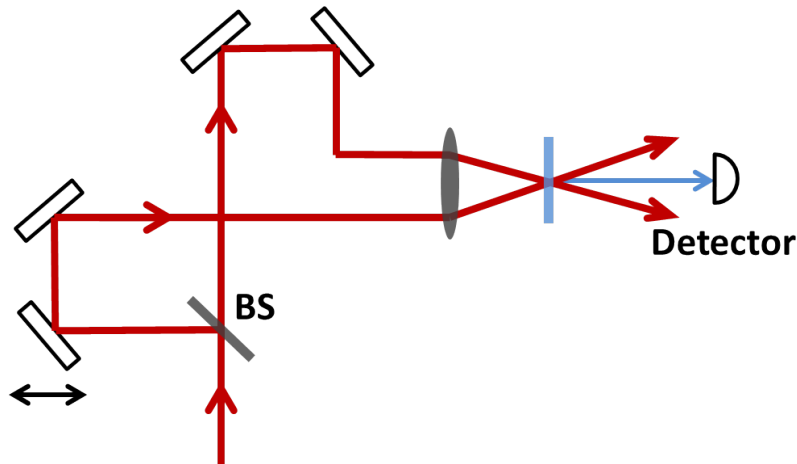


**Fig. 2.19** Schematic of intensity autocorrelation measurement setup

## 2.4.2 Frequency-resolved optical gating

If one knows the instantaneous frequency of the pulses, then the pulses are fully measured. One can multiply the pulse to be measured  $e(t)$  with a gating function  $g(t - \tau)$  leading to a gated signal field

$$e_s(t, \tau) = e(t)g(t - \tau) \quad (2.29)$$

The instantaneous frequency is then easily determined by measuring the power spectrum of  $e_s(t)$ . The entire measurement is realized by scanning through the delay  $\tau$ , and then one obtains a two-dimensional function

$$S(\omega, \tau) = \left| \int dt e_s(t, \tau) e^{-i\omega t} \right|^2 = \left| \int dt e(t) g(t - \tau) e^{-i\omega t} \right|^2 \quad (2.30)$$

which is called the spectrogram of the electric field  $e(t)$ . The spectrogram contains all the information necessary for characterizing the pulses. The next task is to retrieve the complete amplitude and phase information from the spectrogram. The method developed to this end and discussed here is called frequency-resolved optical gating (FROG). The main difficulty in measuring ultrafast pulses is to find an appropriate gate function. This gating function should be well known and as short as the pulses to measure, which is not easy to find. In FROG, the pulse is used to gate itself via nonlinear optical interaction. The most common nonlinear optical interaction used is second harmonic generation.

In SHG FROG the gated field is

$$e_s(t, \tau) = e(t)e(t - \tau) \quad (2.31)$$

and the spectrogram is

$$I_{FROG}(\omega, \tau) = \left| \int dt e(t)e(t - \tau) e^{-i\omega t} \right|^2 \quad (2.32)$$

The FROG spectrogram is also called the FROG trace. Experimentally, the setup to measure the FROG trace is very similar to an intensity autocorrelator. The only difference is that a spectrometer is used rather than a photodiode as shown in Fig. 2.20.

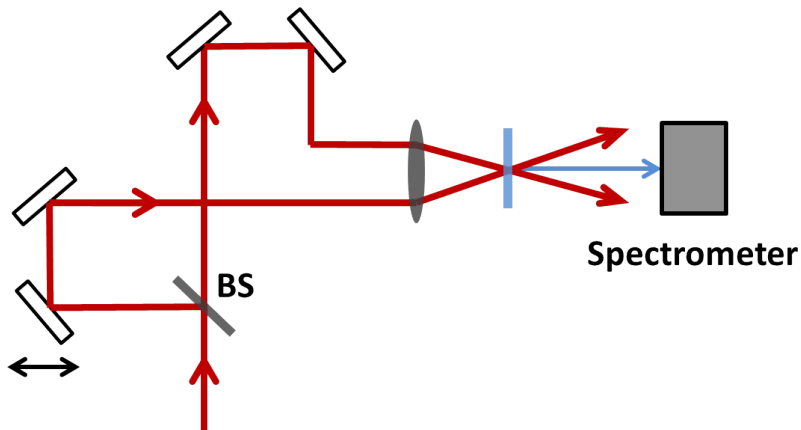


Fig. 2.20 Schematic of SHG-FROG measurement setup



### Signal retrieval from FROG trace

At this point, one has to retrieve  $e(t)$  from the FROG trace[52]. The FROG trace can be written as

$$I_{FROG}(\omega, \tau) = \left| \int dt e_s(t, \tau) e^{-i\omega t} \right|^2 = \left| \iint dt d\Omega \tilde{E}_s(t, \Omega) e^{-i\omega t} e^{i\Omega \tau} \right|^2 \quad (2.33)$$

where

$$\tilde{E}_s(t, \Omega) = \int d\tau e_s(t, \tau) e^{-i\Omega \tau} \quad (2.34)$$

is the Fourier transform of  $e_s(t, \tau)$ . Once we obtain  $e_s(t, \tau)$ , we can obtain  $e(t)$  via

$$e(t) \propto \int d\tau e_s(t, \tau) \quad (2.35)$$

Actually, retrieving  $e_s(t, \tau)$  is recovering  $\tilde{E}_s(t, \Omega)$  from its two-dimensional power spectrum. This phase-retrieval problem has been investigated by the image science community [53] in the 1980s. Trebino and co-workers have further developed several algorithms for recovering the electric field profile from the FROG trace [54]. The flowchart of their original iterative Fourier transform algorithm is shown in Fig. 2.21.

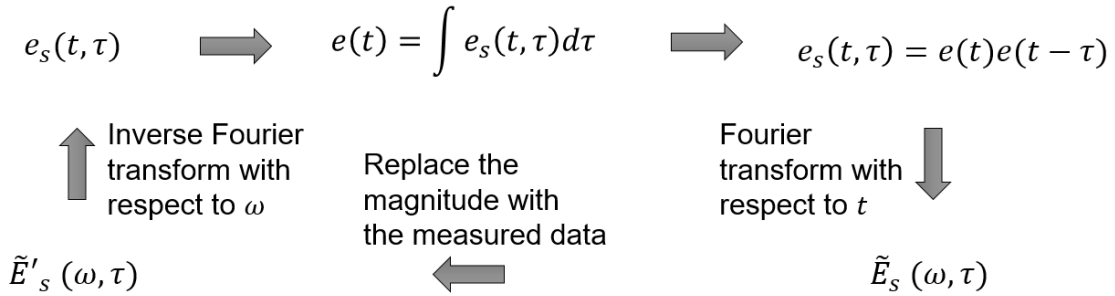


**Fig. 2.21** FROG retrieval algorithm flowchart. Ref. [39]

The retrieval procedure starts with a guess of  $e(t)$ . The next step is to use the guessed  $e(t)$  to generate  $e_s(t, \tau)$  with

$$e_s(t, \tau) = e(t)e(t - \tau) \quad (2.36)$$

Then perform Fourier transform with respect to  $t$  on  $e_s(t, \tau)$  and arrive at  $\tilde{E}_s(\omega, \tau)$ . After this, the magnitude of  $\tilde{E}_s(\omega, \tau)$  is replaced with the experiment data via

$$\tilde{E}'_s(\omega, \tau) = \frac{\tilde{E}_s(\omega, \tau)}{|\tilde{E}_s(\omega, \tau)|} \sqrt{I_{FROG}(\omega, \tau)} \quad (2.37)$$

Inverse Fourier transform  $\tilde{E}'_s(\omega, \tau)$  with respect to  $\omega$  to get  $e_s(t, \tau)$  and then  $e^{(1)}(t)$ , the first estimation of  $e(t)$ , via Eq. (2.35). At this point, one iteration is completed. The obtained  $e^{(1)}(t)$  is then used as the new input for the next iteration. The procedure continues until the solution converges. Criteria for iteration convergence can be the difference between results from two consecutive iterations or the difference between the last computed and experimental data.

In practice, the original algorithm is slow and hard to reach convergence. Various more advanced algorithms have been developed to accelerate convergence and speed up the whole retrieval procedure. The most commonly used algorithm is the principal components generalized projections algorithm (PCGPA) [55].

### 2.4.3 Practical issues in few cycle pulses characterization with FROG

When using FROG for characterizing few-cycle pulses, extra care needs to be taken for obtaining valid measurements [56, 57]. The phase-matching bandwidth is in general inversely proportional to the thickness of the nonlinear crystal. To ensure that the phase-matching bandwidth is large enough for the broad bandwidth of the few-cycle pulses, extremely thin nonlinear crystals with thickness of tens of microns are required. Moreover, from the description above, we obtain the gated signal via SHG

$$e_s(t, \tau) = e(t)e(t - \tau) \quad (2.38)$$

in which we assumed that the phase matching bandwidth is unlimited. However, this does not hold for few-cycle pulses, which have very broad bandwidth. Moreover, the frequency-dependent response of the spectrometer is also a problem that needs attention. Overall, frequency-dependent effects, which become significant due to the broad bandwidth of few-cycle pulses, need to be corrected. It was shown in Ref. [58, 57] that the experimentally measured SHG-FROG trace  $S_{exp}(\Omega, \tau, L)$  is proportional to the product of a spectral filter  $R(\Omega)$  and the ideal SHG-FROG trace  $S_{ide}(\Omega, \tau)$  which is written as

$$S_{exp}(\Omega, \tau, L) \propto R(\Omega)S_{ide}(\Omega, \tau) \quad (2.39)$$

where

$$R(\Omega) = \frac{\Omega^3}{n(\Omega)^2} Q(\Omega) \text{sinc}^2 \left[ \Delta k \left( \frac{\Omega}{2}, \frac{\Omega}{2} \right) \frac{L}{2} \right], \quad (2.40)$$

$$S_{ide}(\Omega, \tau) = \left| \int_{-\infty}^{+\infty} E(\omega) E(\Omega - \omega) e^{i\omega\tau} d\omega \right|^2 \quad (2.41)$$

in which  $\Omega$  is the detected frequency,  $n(\Omega)$  is the refractive index,  $L$  is the crystal length,  $Q(\Omega)$  is the spectral sensitivity of the detector,  $E(\omega)$  is the Fourier transform of  $e(t)$ , and  $\Delta k$  is the

phase mismatch. The spectral filter  $R(\Omega)$  originates from the finite conversion bandwidth and the wavelength dependent detection sensitivity. Eq. (2.39) can be applied to correct the measured FROG trace. Then the corrected FROG trace is used as the input to the retrieval algorithm.

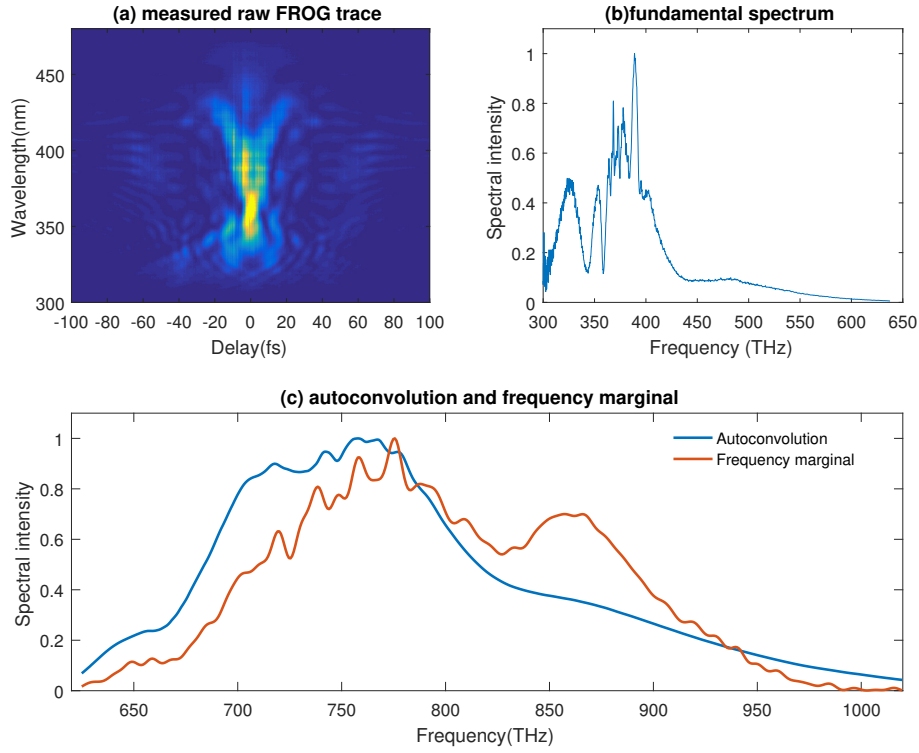


**Fig. 2.22** FROG trace frequency marginal correction. (a) Experimentally measured raw FROG trace; (b) spectrum of the pulses to measure in the frequency domain; (c) the comparison of input pulse spectrum autoconvolution and the FROG trace frequency marginal

The FROG trace overdetermines the electric field. Assume a pulse with  $N$  data points, the FROG trace of this pulse has  $N \times N$  data points, which are more than enough to determine  $2N$  degrees of freedom in the pulse. There is redundancy in the FROG trace that can be used to check the data fidelity. The frequency marginal of the FROG trace is of particular interest. In general, the frequency marginal  $P_\omega$  of a spectrogram  $S(\omega, \tau)$  is obtained by integrating over delay [39]

$$P_\omega = \int d\tau S(\omega, \tau) \quad (2.42)$$

For the SHG-FROG trace, the frequency marginal becomes

$$P_\omega = \int d\tau I_{FROG}(\omega, \tau) = \frac{1}{2\pi} \int d\omega' |E(\omega')|^2 |E(\omega - \omega')|^2 \quad (2.43)$$

which is actually the autoconvolution of the input pulse power spectrum. The autoconvolution has to be calculated using the spectral intensity in frequency  $I(\omega)$  rather than in wavelength  $I(\lambda)$  domain. In practice, the spectrometer usually provides  $I(\lambda)$ , which has to be converted to  $I(\omega)$  before it can be used for autoconvolution calculation and FROG trace retrieval. The input pulse power spectrum is usually measured with a spectrometer, which can be a separate check of the FROG setup. Thus the frequency marginal provides an independent route to check the quality of the measured data. Deviation of the frequency marginal of the FROG trace from the autoconvolution of the input pulse power spectrum indicates systematic errors in the FROG measurement.

On the other hand, although  $R(\Omega)$  can be incorporated to correct the FROG trace, it is often not easy to obtain or measure precisely. Conversely, one can simply impose the FROG frequency marginal to be the same as the autocorrelation of the input pulse power spectrum. By doing this, it gives a curve for correcting each spectrum in the spectrogram. In Fig. 2.22(a), the measured raw FROG trace is shown. The input pulse spectrum measured independently with a spectrometer is presented in Fig. 2.22(b). In Fig. 2.22(c), the autoconvolution of the input pulse spectrum and the frequency marginal of the FROG trace are shown. Although carefully measured, it is obvious that the autoconvolution of the input pulse spectrum and the frequency marginal of the FROG trace deviate from each other, which indicates that the FROG trace must be corrected. Meanwhile, the FROG measurement actually covers almost the entire bandwidth as predicted by the autoconvolution, thanks to the extra attention paid in maintaining the full bandwidth in upconversion, i.e., a thin BBO of 10  $\mu\text{m}$  thickness is used for SHG.

The nonlinear interaction geometry, as shown in Fig. 2.20, is used in a SHG-FROG setup. This makes the measured pulse duration deviate from the real one

$$\tau_{\text{measure}}^2 = \tau_{\text{real}}^2 + \delta t^2 \quad (2.44)$$

due to a geometric time-smearing effect, where  $\delta t = \theta d_f / 2c$ , and  $\theta$  is the intersection angle of the two input beams,  $d_f = f\lambda / \pi$  is beam diameter in the focal plane.

The measured and then corrected SHG-FROG trace is shown in Fig. 2.23(a). The FROG trace is used as the input of the retrieval algorithm. Fig. 2.23(c) shows the retrieved FROG trace. The reconstructed FROG trace matches well with the experimentally measured trace. The retrieved pulse temporal intensity profile and the temporal phase are shown in Fig. 2.23(b). The TL pulse profile calculated from the reconstructed pulse spectrum is shown in the same figure (green dashed line) for comparison. The measured pulse duration is  $\sim 5.3$  fs and the TL pulse duration is  $\sim 4.3$  fs. Meanwhile, the reconstructed pulse spectrum and the spectral phase are shown in Fig. 2.23(d). The HCF output spectrum is also shown in the same figure for comparison. It can be seen that the retrieved spectrum and the input pulse spectrum also

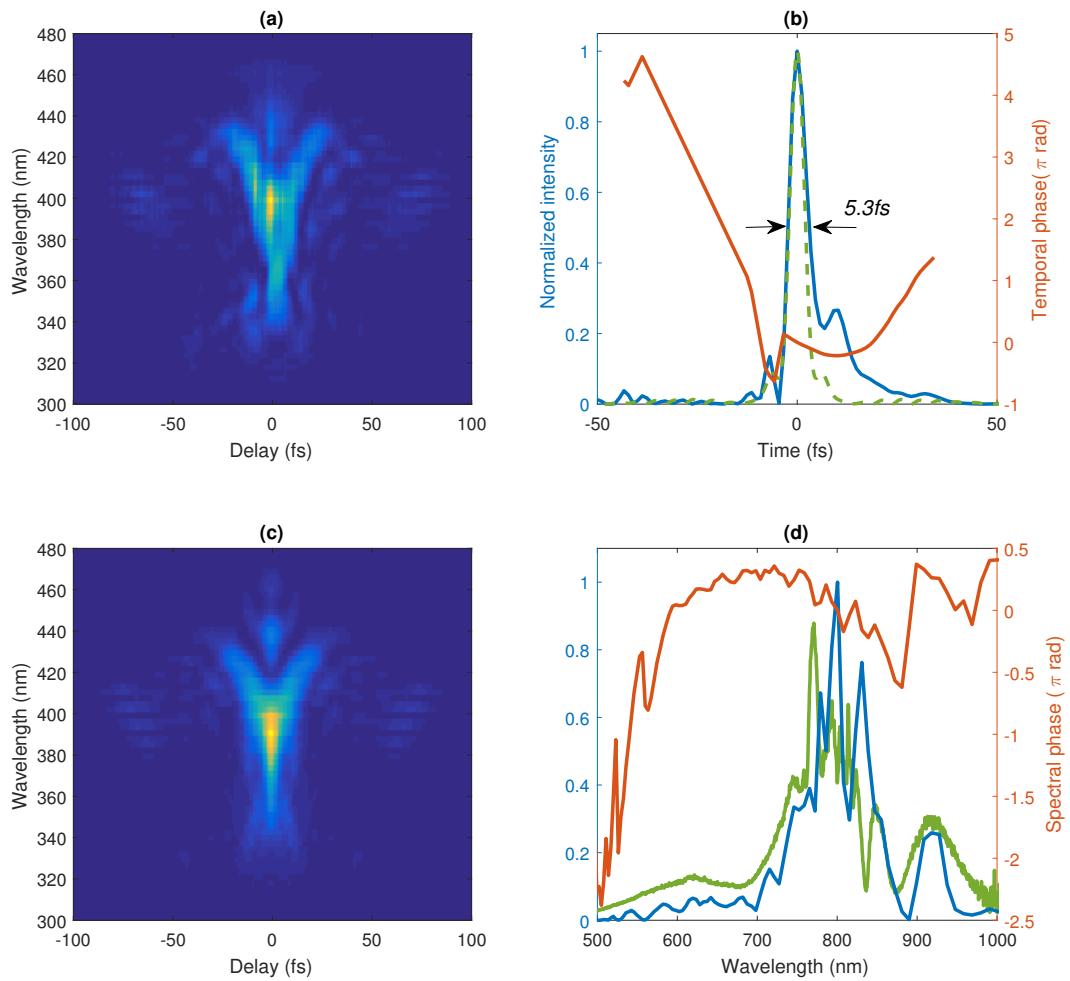


**Fig. 2.23** FROG measurement and retrieval. (a) Measured FROG trace, (b) Retrieved pulse temporal intensity (blue) and phase (red), the TL pulse calculated from the reconstructed input pulse spectrum is shown for comparison (green dashed line) (c) Retrieved FROG trace, (d) Retrieved spectral intensity (blue) and phase (red), the input spectrum (green) measured separately with a spectrometer is shown for comparison

match quite well. It is worth noting that the reconstructed spectrum only covers down to approximately 500 nm which originates from the limited dispersion compensation bandwidth of the DCMs as discussed above. The temporal phase variation over the time range, in which there is substantial energy, is less than  $2\pi$ . The spectral phase variation is also less than  $2\pi$  in the region, where a significant part of the energy is located. Both indicate the pulse has been properly compressed. Meanwhile, the deviation of the measured pulse duration from the TL pulse duration tells that the pulse is not fully compressed. It can be inferred from the shape of spectral phase or the trailing pulse in the time domain that there is residual higher-order dispersion that is not compensated by the DCMs. If improved custom-designed DCM pairs, which compensate for higher-order dispersion, are employed in the future, the compressed pulse duration will be further reduced.

## 2.5 Summary

In this chapter, the generation and characterization of few-cycle laser pulses, which are used for the experiments described in the following chapters of this thesis, are discussed. Few-cycle pulses generation and characterization are both challenging tasks. A hollow-core fiber compressor is constructed based on a commercial laser system. The commercial laser system is an actively CEP-stabilized Ti:sapphire chirped-pulse amplifier. The HCF compressor output pulse is characterized with the SHG-FROG method. Practical issues in characterizing few-cycle pulses with FROG have been discussed in detail. The hollow-core fiber compressor provides few-cycle pulses with a duration of 5.3 fs and  $\sim 1$  mJ of energy. Further reduction in pulse duration is feasible in the future using improved custom-designed double-chirped mirrors.



# Chapter 3

## High harmonic generation and isolated attosecond pulse generation

### 3.1 Introduction to high harmonic generation

When a gas, plasma or solid medium is exposed to intense laser fields of sufficient strength, highly nonlinear interaction leads to emission of very high harmonics of the fundamental optical frequency. This process is termed high harmonic generation (HHG). Here, we limit our discussion only on HHG from noble gases. HHG from gas was first observed in 1987 [59]. Different from perturbative harmonic generation, e.g., SHG, THG, HHG is a strong-field phenomenon or an extreme nonlinear optics phenomenon. In perturbative harmonic generation, the signal yield decreases rapidly with increasing harmonic order. This can be understood by considering the material needs to absorb  $n$  photons for emitting one single high energy photon of harmonic order  $n$ . Meanwhile, the probability of absorbing  $n$  photons decreases exponentially as  $n$  increases. In contrast, the spectrum of HHG typically consists of three parts with distinct characteristics [60]. A schematic HHG spectrum with the three parts is shown in Fig. 3.1. In the low-order perturbative regime, the harmonics signal decreases rapidly as harmonic order  $n$  increases, as in perturbative harmonic generation. For higher-order harmonics, the signal intensity remains approximately unchanged as the harmonic order  $n$  increases. This region is called the HHG plateau region. This plateau ends abruptly at the cutoff region. Noble gases are the most commonly used gas species for HHG. The spectrum of HHG with noble gases consists of only odd harmonic orders due to the inversion symmetry of the gas atoms.



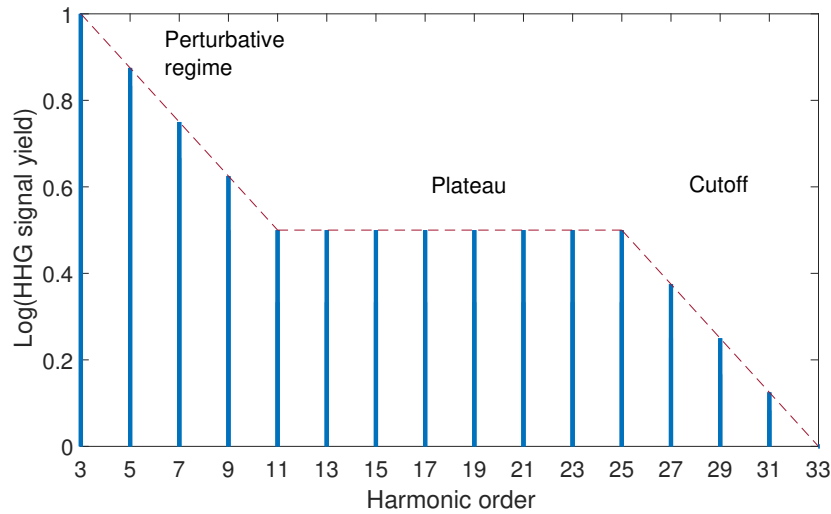


**Fig. 3.1** A schematic HHG spectrum. The HHG spectrum consists of three parts with distinct characteristics. In the low-order perturbative regime, the intensity of the harmonics decreases as the harmonic order  $n$  increases. In the plateau, the intensity of the harmonics remain approximately unchanged. The plateau ends abruptly in the cutoff regime. The HHG spectrum consists of only odd harmonic orders

### 3.1.1 Semiclassical model of high harmonic generation

High harmonic generation in noble gases originates from the nonlinear optical interaction between intense laser fields and atoms. Each atom can be regarded as a single emitter of XUV radiation. In order to well describe the HHG process, the single-atom response must be studied first before describing further effects like propagation and phase matching.

Although a full description of high harmonic generation requires a quantum theory [61], semiclassical models can be used to qualitatively describe the HHG process [62–64]. Some important aspects of HHG, e.g., the harmonic cutoff energy, can be calculated with the semiclassical model which is also termed the three-step model. Moreover, compared to the full quantum model, the semiclassical model provides a more intuitive picture of the HHG process.

In the semiclassical model, the whole HHG process is described in three steps. In the first step, an electron is ionized into the continuum from the atom by the intense laser field. In the second step, the freed electron is driven by the oscillating laser field. The Coulomb potential of the ion is neglected in this step and the electron is treated as free electron in the continuum. The motion of the electron can be then described simply by Newton’s equation of motion. The freed electron is first driven away from the parent ion by the laser field. Only when an electron is released into the laser field at the right phase, the electron will be driven back to the parent

ion. In the third step, the electron recombines with the parent ion and the excess energy of the returning electron is released in the form of high-energy XUV photons.

In the first step, the atom is ionized by the laser, which is a quantum process. Under various approximations, there are several analytic solutions for the ionization rate. These ionization rate equations allow numerical simulation without solving the TDSE which is usually computationally expensive. Here, an introduction to these approximations is given.

The ionization involved in high harmonic generation is a non-perturbative phenomenon, in which the strength of the ionizing electric field is comparable to the intra-atomic electric field. In the 1960s, Keldysh developed the first theory on one-electron atom photoionization by a strong field, when the photon energy is much smaller than the ionization potential [65]. He derived the photoionization formula for the direct transition between the electronic ground state and the Volkov states. Volkov states are the states of a free electron in the electromagnetic field [66]. In this theory, the perturbation of the ground state by the laser field and the intermediate resonance states were both neglected. Neglecting the resonance bound states is called strong-field approximation (SFA) [67].

### Volkov continuum states

The Schrödinger equation for an atom in a laser field is

$$i\hbar \frac{d}{dt} \psi(\vec{r}, t) = [H_0 + H_I] \psi(\vec{r}, t) \quad (3.1)$$

where  $H_0$  is the Hamiltonian of the atom and  $H_I$  is the Hamiltonian of the laser field.

When the electron is far away from the rest of the atom, the effect of the Coulomb potential on the electron is ignored, so  $H_0 = 0$ . Then Eq. (3.1) becomes

$$i\hbar \frac{d}{dt} \psi(\vec{r}, t) = H_I \psi(\vec{r}, t) \quad (3.2)$$

Keeping in mind that the classical Hamiltonian of an electron in laser field is

$$H_{I,classic} = \frac{1}{2m_e} (\vec{p} + \frac{e}{c} \vec{A})^2 - e\phi \quad (3.3)$$

where  $\vec{A}$  and  $\phi$  are the vector and scalar potential of the electromagnetic field, respectively,  $\vec{p}$  is the canonical momentum, it is straightforward to write down the quantum mechanical Hamiltonian

$$H_I = \frac{1}{2m_e} (\hat{p} + \frac{e}{c} \vec{A})^2 - e\phi \quad (3.4)$$

where the canonical momentum  $\vec{p}$  is simply replaced by the momentum operator  $\hat{p} = -i\hbar\nabla$ . In general,  $\vec{A}$  and  $\hat{p}$  do not commute,  $\hat{p} \cdot \vec{A} - \vec{A} \cdot \hat{p} = -i\hbar\nabla \cdot \vec{A} \neq 0$ . However, in the Coulomb gauge,  $\nabla \cdot \vec{A} = 0$  and then  $\hat{p} \cdot \vec{A} = \vec{A} \cdot \hat{p}$ . When the electron is far away from the ion, the Coulomb potential is ignored, and assuming there is no other static field, then  $\phi = 0$ , we have

$$H_l = \frac{1}{2m_e} \hat{p}^2 + \frac{e}{m_e c} \vec{A} \cdot \hat{p} + \frac{e^2}{2m_e c^2} \vec{A}^2 \quad (3.5)$$

Assuming there is a monochromatic, linearly polarized laser field, of which the electric field is given by

$$\vec{E}(t) = \vec{u}_0 E_0 \cos(\omega t) \quad (3.6)$$

where  $\vec{u}_0$  is the unit vector defines the electric field direction, and the vector potential of the laser field is

$$\vec{A}(t) = -\vec{u}_0 A_0 \sin(\omega t) \quad (3.7)$$

The solutions are eigenstates of the canonical momentum with eigenvalue  $\vec{p} = \vec{p}_m - \frac{e}{c} \vec{A}(t)$ . The solution can be expressed as

$$\psi_V(\vec{r}, t) = e^{\frac{i}{\hbar} \left[ \left[ \vec{p}_m - \frac{e}{c} \vec{A}(t) \right] \cdot \vec{r} - \frac{\vec{p}_m^2}{2m_e} t - U_p t \right]} \int_0^t dt' \left[ \vec{p}_m - \frac{e}{c} \vec{A}(t') \right]^2 \quad (3.8)$$

Use (3.7), we can have [40]

$$\begin{aligned} \psi_V(\vec{r}, t) = & e^{\frac{i}{\hbar} \left[ \vec{p}_m \cdot \vec{r} - \frac{\vec{p}_m^2}{2m_e} t - U_p t \right]} \sum_{n=-\infty}^{\infty} \sum_{m=-\infty}^{\infty} J_m \left( \frac{e^2 A_0^2}{8\hbar\omega m_e c^2} \right) \\ & \times J_{n-2m} \left( \left| \vec{E} \cdot \vec{p}_m \right| \frac{e A_0}{\hbar\omega m_e c} \right) e^{in\omega t} \end{aligned} \quad (3.9)$$

where  $\vec{p}_m$  is the mechanical momentum of the electron, and  $J_m$  is the  $m$ th order Bessel function of the first kind.

### Ionization rate

Keldysh's ionization model neglects the effect of the Coulomb potential on the final state of the electron [65]. However, the Coulomb potential is not very small compared to the potential of the laser field in location far away from the nucleus. This fact bears difficulty of Keldysh's model. Perelomov, Popov, and Terent'ev (PPT) introduced a model [68–70], which includes the Coulomb interaction at larger internuclear distances. The ionization rate  $w$  calculated with

the PPT model fits well with the experiments. The PPT ionization rate is written as

$$w_{PPT} = \sum_{q>q_0}^{\infty} w_q \quad (3.10)$$

where  $q_0$  is the minimum number of photons required to ionize an electron,  $q$  is the number of photons absorbed, and  $w_q$  is the rate of ionization due to  $q$ -photon absorption. Assume an atom with an initial quantum state  $(n, l, m)$  before the laser field arrives, we then have

$$w_q = A_q(\omega, \gamma) |C_{n^*l^*}|^2 G_{lm} I_p \left( \frac{2F_0}{E} \right)^{2n^*} \left( \frac{2F_0}{E} \frac{1}{\sqrt{1+\gamma^2}} \right)^{-|m|-1} \times \frac{4}{\sqrt{3\pi}} \frac{1}{|m|!} \frac{\gamma^2}{1+\gamma^2} e^{-\frac{2F_0}{3E}g(\gamma)} \quad (3.11)$$

where  $E$  is the laser field strength and

$$A_q = e^{-\alpha(q-\nu)} w_m [\sqrt{\beta(q-\nu)}] \quad (3.12)$$

$$\nu = \frac{I_p}{\omega} \left( 1 + \frac{1}{2\gamma^2} \right) = \frac{I_p + U_p}{\omega} \quad (3.13)$$

$$\alpha(\gamma) = 2 \left[ \sinh^{-1} \gamma - \frac{\gamma}{\sqrt{1+\gamma^2}} \right] \quad (3.14)$$

$$\beta(\gamma) = \frac{2\gamma}{\sqrt{1+\gamma^2}} \quad (3.15)$$

$$w_m(x) = \frac{x^{2|m|+1}}{2} \int_0^1 \frac{e^{-x^2 t} t^{|m|}}{\sqrt{1-t}} dt \quad (3.16)$$

in which  $F_0 = (2I_p)^{3/2}$  is the Coulomb field and  $(2F_0/E)^{2n^*}$  is the correction of the long-range Coulomb interaction,  $\gamma = \omega(F_0^{1/3}/E)$  is the Keldysh parameter, whose significance will be discussed later.  $n^* = Z/\sqrt{2I_p}$  is the effective principal quantum number and the effective orbital quantum number  $l^* = n^* - 1$ . Moreover, there is

$$|C_{n^*l^*}|^2 = \frac{2^{2n^*}}{n^* \Gamma(n^* + l^* + 1) \Gamma(n^* - l^*)} \quad (3.17)$$

$$G_{lm} = \frac{(2l+1)(l+|m|)!}{2^{|m|} |m|! (l-|m|)!} \quad (3.18)$$

$$g(\gamma) = \frac{3}{2\gamma} \left[ \left( 1 + \frac{1}{2\gamma^2} \right) \sinh^{-1} \gamma - \frac{\sqrt{1+\gamma^2}}{2\gamma} \right] \quad (3.19)$$

The Keldysh parameter

$$\gamma = \omega(F_0^{1/3}/E) = \omega\sqrt{2I_p}/E \quad (3.20)$$

can be regarded as the ratio of the classical tunneling time and the laser optical period. When  $\gamma > 1$ , the laser field is oscillating too fast so that the electron does not have enough time to tunnel through the potential barrier. The dominating ionization mechanism taking place here is multiphoton ionization. In contrast, when  $\gamma < 1$ , the bound electron can leave the parent ion via tunneling ionization. Especially, when  $\gamma \ll 1$ , the tunneling probability can be calculated using the quasi-static formula for a direct current (DC) field.

The Ammosov, Delone, Krainov (ADK) model [71] was introduced as an extension of the PPT model to cover complex atoms. The ionization rate calculated with the ADK model is the limit of PPT model, when  $\gamma$  approaches 0. Compared to the PPT model, the ADK ionization rate has a simpler form, which is

$$w_{ADK} = |C_{n^*l^*}|^2 G_{lm} I_p \left(\frac{2F_0}{E}\right)^{2n^* - |m| - 1} e^{-\frac{2F_0}{3E}} \quad (3.21)$$

It has been proven that the ADK rate applies when  $\gamma < 0.5$ .

### Classical motion of an electron in a strong laser field

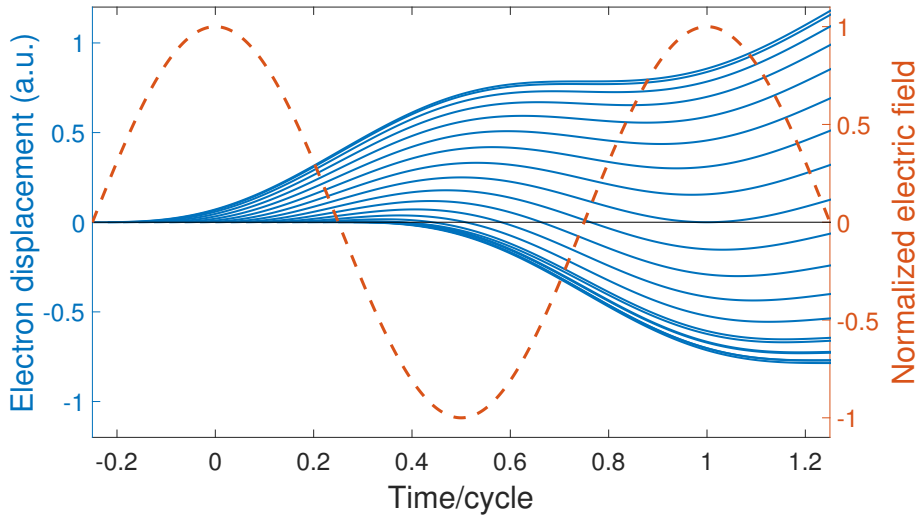


**Fig. 3.2** Trajectories of an electrons ionized at different phase. The red dashed line is the electric field driving the electron. Note that the electric field shown here is chosen to be  $E(t) = E_0 \sin(\omega_0 t)$  for demonstration. The blue curves are the different trajectories of an electron ionized at different phase. The black horizontal line shows the initial position of the electron at  $x = 0$ .

In the second step, the freed electron moves under the influence of the laser field. To simplify the derivation, we assume the laser field is monochromatic and the field is linearly polarized along the  $x$  axis. As a result, the laser field is

$$E(t) = E_0 \cos(\omega_0 t) \quad (3.22)$$

where  $E_0$  is the amplitude of the laser field.

Assume the freed electron starts its motion from the origin, i.e., the initial position of electron is  $x = 0$ . The initial velocity of the electron is also assumed to be zero,  $v = 0$ . As a result, the equation of motion of the electron is

$$\frac{d^2 x}{dt^2} = -\frac{e}{m_e} E(t) = -\frac{e}{m_e} E_0 \cos(\omega_0 t) \quad (3.23)$$

where  $e$  is the elementary charge and  $m_e$  is the electron mass.

Assume an electron is ionized at time  $t_i$ , then the velocity of this electron at time  $t$  is

$$\begin{aligned} v(t) &= \int_{t_i}^t \frac{d^2 x}{dt^2} dt = \int_{t_i}^t -\frac{e}{m_e} E_0 \cos(\omega_0 t) dt \\ &= -\frac{e E_0}{m_e \omega_0} [\sin(\omega_0 t) - \sin(\omega_0 t_i)] \end{aligned} \quad (3.24)$$

and the position of this electron at  $t$  is

$$x(t) = \int_{t_i}^t v(t) dt = \frac{e E_0}{m_e \omega_0^2} [\cos(\omega_0 t) - \cos(\omega_0 t_i) + \omega_0 \sin(\omega_0 t_i)(t - t_i)] \quad (3.25)$$

Electrons ionized by the laser field at different phases  $\varphi_i = \omega_0 t_i$  will travel along different trajectories as shown in Fig 3.2. Only electrons ionized at certain phase will return to the parent ion and contribute to HHG emission. In order to show the trajectories of an electron ionized at different phase neighboring the electric field peak, the electric field takes the form  $E(t) = E_0 \sin(\omega_0 t)$ . However, in the following discussion, the electric field has the form  $E(t) = E_0 \cos(\omega_0 t)$  as in Eq. (3.22) and the shape as in Fig. 3.3. More careful examination on the electron trajectories reveals that an electron freed at  $\pi/2 \leq \varphi_i < \pi$ , which is the rising edge of the electric field, will never return to its parent ion. This electron does not contribute to the HHG emission. Meanwhile, an electron freed at  $0 \leq \varphi_i < \pi/2$  will eventually return to its parent ion. Especially, for an electron freed at  $t_i = 0$ , it will return to the parent ion one laser cycle later at  $\omega_0 t = 2\pi$ . One laser cycle  $T_0$  is the longest excursion time an electron can have in the laser field. If one looks at a larger time range, one would find that an electron can return to  $x = 0$  more than once. However, due to the electron wave packet quantum diffusion,

the contribution to HHG from an electron with excursion time longer than one optical cycle is negligible. Therefore, only the electron returning to its parent ion within one cycle are concerned in the following discussion. Electrons ionized at different phase have different return time. Electrons ionized earlier return later as shown in Fig. 3.3. Due to the different travel time in the laser field, electrons will return to the parent ion with different kinetic energy. The kinetic energy of the electron at moment  $t$  is

$$\begin{aligned} E_k(t) &= \frac{1}{2}m_e v^2(t) = \frac{e^2 E_0^2}{2m_e^2 \omega_0^2} [\sin(\omega_0 t) - \sin(\omega_0 t_i)]^2 \\ &= 2U_p [\sin(\omega_0 t) - \sin(\omega_0 t_i)]^2 \end{aligned} \quad (3.26)$$

where the ponderomotive energy of electrons  $U_p$ , which is the cycle-averaged kinetic energy of an electron in an electromagnetic field, is

$$U_p = \frac{e^2 E_0^2}{4m_e^2 \omega_0^2} \quad (3.27)$$

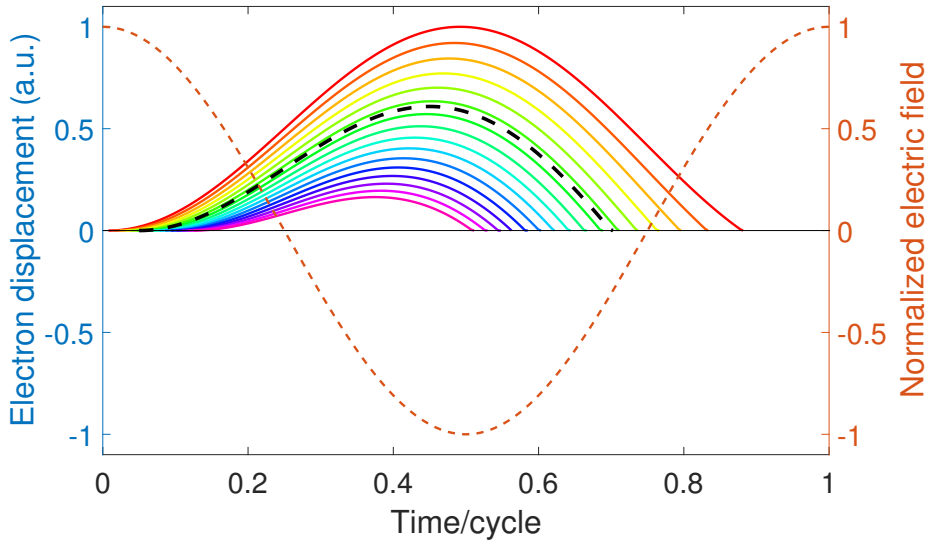


**Fig. 3.3** Trajectories of electrons ionized at different phases and returning within one laser cycle. The black dashed line shows the trajectory of the electron which has the highest returning kinetic energy. The electric field that releases the electron from the atom is shown as red dashed line. An electron leaves its parent ion earlier returns to its parent ion later and takes a long excursion time.

After traveling in the laser field, the electron eventually recombines with its parent ion at moment  $t = t_r$  and a high-energy photon is emitted. The energy of the emitted photon is

$$\hbar\omega_X(t_r) = I_p + E_k(t_r) = I_p + 2U_p [\sin(\omega_0 t_r) - \sin(\omega_0 t_i)]^2 \quad (3.28)$$

where  $I_p$  is the ionization potential of the atom used for HHG and  $\omega_X$  is the angular frequency of the emitted photon. This event will happen twice in each laser cycle. For Ti:sapphire laser ( $\lambda = 800$  nm,  $T_0 = 2.7$  fs), the separation between two HHG events is then 1.3 fs.

When the electron recombines with the parent ion at moment  $t = t_r$ ,  $x(t_r) \propto \cos(\omega_0 t_r) - \cos(\omega_0 t_i) + \omega_0 \sin(\omega_0 t_i)(t_r - t_i) = 0$ . However, there is no analytic solution to this problem. We can only obtain the recombination moment numerically. Once we know  $t_r$ , it is straightforward to find out the velocity and the kinetic energy of the returning electron. The dependence of the kinetic energy on the emission phase is shown in Fig. 3.4. The electron ionized at  $t_i = 0.05 T_0$  obtains the maximum kinetic energy  $E_{k,max} = 3.17 U_p$ . As a result, the highest photon energy obtained in the HHG process is

$$\hbar\omega_{X,max} = I_p + 3.17 U_p \quad (3.29)$$

This harmonic cutoff law is one of the most important predictions from the semiclassical model. It provides an easy way to calculate the cutoff energy of the HHG spectrum and to understand its dependence on driving wavelength.

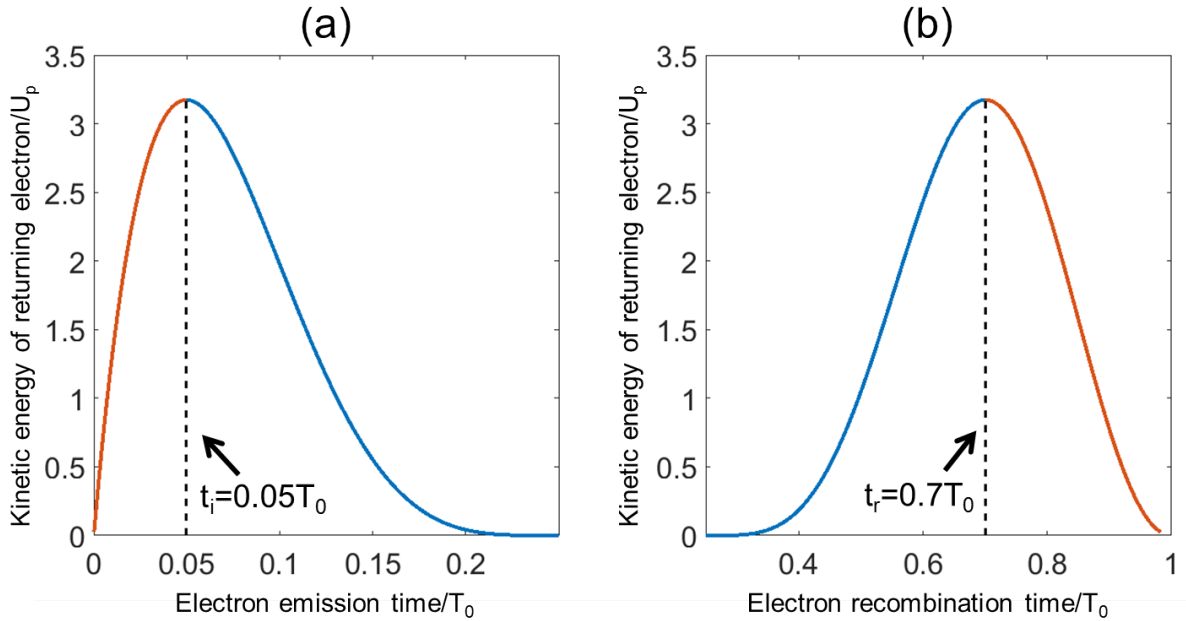


**Fig. 3.4** Electron return kinetic energy versus the ionization time and recombination time. (a) Kinetic energy of returning electron versus electron emission time. The electron with highest returning kinetic energy is ionized at  $t = 0.05 T_0$ . (b) kinetic energy of returning electron versus electron recombination time. The electron with highest returning kinetic energy returns to the parent ion at  $t = 0.7 T_0$ . In both figures, the red curves correspond to long-trajectory electrons and the blue curves correspond to short-trajectory electrons.



Electrons ionized before  $0.05 T_0$  return to the parent ion after  $t_r = 0.7 T_0$ . Electrons ionized after  $0.05 T_0$  return to the parent ion between  $0.25 T_0$  and  $0.7 T_0$ , which is shown in Fig. 3.4 as blue curves. Apparently, the electrons emitted before  $0.05 T_0$  follow a longer trajectory than those electrons emitted after  $0.05 T_0$ . The electrons following a longer trajectory are referred to as long-trajectory electrons, while the others are called short-trajectory electrons. There is one trajectory possible with which the electron acquires the maximum kinetic energy  $3.17 U_p$ . For emitting any photon energy other than the cutoff energy, the electron may follow either the long trajectory or short trajectory. However, the HHG from electrons with different trajectories have quite different properties. We can use phase matching or spatial filtering to select out either one of them. Usually, the short-trajectory HHG is preferred since the short-trajectory HHG is less divergent and spectrally narrower than the long-trajectory HHG [72]. Another important aspect can be extracted from the semiclassical model is that is that HHG corresponding to the two different trajectories has different intrinsic chirp as shown in Fig. 3.4. For short-trajectory HHG, the photons emitted earlier have lower photon energy, which means the short-trajectory HHG is positively chirped. Meanwhile, the long-trajectory HHG is inherently negatively chirped. To achieve transform-limited attosecond pulses, this intrinsic attochirp of HHG needs to be compensated.

Taking another glance at the cutoff law Eq. (3.29), one may be inclined to conclude that, by simply increasing the ionization potential  $I_p$  or the laser intensity to increase  $U_p$ , one can increase the cutoff energy at will. However, upscaling the cutoff energy is not as straightforward as it seems. First, there are only a small number of noble gases which qualify as candidate gas medium for HHG. Among them, helium has the highest ionization potential of 24.6 eV. High-power lasers are able to provide extremely high laser intensity. However, there is an upper limit of laser intensity that is applicable for HHG experiments. Laser intensity above the upper limit would totally deplete the gas atom's ground-state population. As we will discuss later, zero ground-state population would switch off HHG emission. After taking into account the saturation intensity, which is the highest intensity allowed, the HHG cutoff energy is [40]

$$\hbar\omega_{X,s} = I_p + \frac{0.5I_p^{3.5}\lambda^2}{\left[\ln\left(\frac{0.86I_p^{3.2n^*-1}G_{lm}C_{n^*l^*}^2\tau_p}{-\ln(1-p_s)}\right)\right]^2} \quad (3.30)$$

where  $p_s$  is the saturation ionization probability allowed for XUV radiation and  $\omega_{X,s}$  is the angular frequency of the cutoff photon at saturation intensity. Noted that the obtained cutoff energy  $\hbar\omega_{X,s}$  is proportional to  $\lambda^2$ , laser with longer wavelength is preferred when achieving high cutoff energy is the main objective. Meanwhile, due to the quantum diffusion of the

electron wavepacket, the HHG conversion efficiency is proportional to  $\sim \lambda^{-5.5}$ . When using long wavelength laser for HHG, the efficiency would reduce drastically.

### 3.1.2 Quantum model of high harmonic generation

The semiclassical model mentioned above works well in predicting the HHG cutoff energy. However, the complete information of the amplitude and phase of each HHG order is not given by the semiclassical model. In principle, the problem can be tackled by solving the time-dependent Schrödinger equation (TDSE). However, in practice, it is difficult and numerically expensive to solve it. It was demonstrated by Lewenstein and coworkers [73] that the time-dependent Schrödinger equation can be solved analytically under the strong-field approximation (SFA). Here the solution is briefly introduced. For a detailed solution and discussion of the problem, the reader is kindly referred to Ref. [40, 73].

In Lewenstein's theory, it assumes that the harmonic field is radiated by electric dipoles. Adopting atomic units  $e = m_e = \hbar = a_0 = 1$ , the dipole moment can be expressed as  $-e\vec{r} = -\vec{r}$ . In quantum mechanics, we calculate the expectation value of the dipole moment via

$$\vec{r}(t) = \langle \Psi(\vec{r}, t) | \vec{r} | \Psi(\vec{r}, t) \rangle \quad (3.31)$$

where  $\Psi(\vec{r}, t)$  is the wave function of the system. Provided the laser field around the atom is  $\vec{E}(t)$ , and using the single-electron approximation, then the Schrödinger equation is

$$i \frac{\partial}{\partial t} |\Psi(\vec{r}, t)\rangle = \left[ -\frac{1}{2} \nabla^2 + V(\vec{r}) - \vec{E}(t) \cdot \vec{r} \right] |\Psi(\vec{r}, t)\rangle \quad (3.32)$$

The wave function can be decomposed into

$$|\Psi(\vec{r}, t)\rangle = e^{-i\mu t} \left[ a(t) |0\rangle + \int d^3\vec{v} b(\vec{v}, t) |\vec{v}\rangle \right] \quad (3.33)$$

where  $a(t)$  is ground-state amplitude, and  $b(\vec{v}, t)$  are the amplitudes of the continuum states  $|\vec{v}\rangle$ . Inserting Eq. (3.33) into Eq. (3.31), we have

$$\begin{aligned} \vec{r} = & a^2(t) \langle 0 | \vec{r} | 0 \rangle + \int d^3\vec{r} a^*(t) b(\vec{v}, t) \langle 0 | \vec{r} | \vec{v} \rangle \\ & + \int d^3\vec{r} a(t) b(\vec{v}, t) \langle \vec{v} | \vec{r} | 0 \rangle + \int d^3\vec{r} a(t) b^2(\vec{v}, t) \langle \vec{v} | \vec{r} | \vec{v}' \rangle \end{aligned} \quad (3.34)$$

in which

$$d(\vec{r}) = \langle \vec{v} | \vec{r} | 0 \rangle \quad (3.35)$$

is the atomic dipole matrix element for the bound-free transition. In Eq. (3.34),  $\langle \vec{v} | \vec{r} | \vec{v}' \rangle$  is related to continuum-continuum transitions. In the derivation, the ground-state depletion is assumed to be slow, thus  $a^2(t) \langle 0 | \vec{r} | 0 \rangle$  is a slow variation term. Ignoring these two terms, we have

$$\vec{r} = \int d^3\vec{r} a^*(t) b(\vec{v}, t) d^*(\vec{v}) + c.c. \quad (3.36)$$

This means the dipole radiation for HHG originates from the recombination of the returning electron wave packet with the ground state. As mentioned before, if the ground state is completely depleted, i.e.,  $a(t) = 0$ , when the recombination happens, there would be no XUV radiation. Since  $a(t)$  can be obtained via PPT or ADK model, and  $d(\vec{v})$  is also a known quantity, only  $b(\vec{v}, t)$  is an unknown quantity before one can calculate the dipole moment  $\vec{r}$ . Inserting Eq. (3.33) into Eq. (3.32), one can obtain

$$b(\vec{r}, t) = i \int_{-\infty}^t dt' a(t') \vec{E}(t') \cdot \vec{d}[\vec{v} + \vec{A}(t) - \vec{A}(t')] e^{iS[\vec{v} + \vec{A}(t) - \vec{A}(t'), t, t']} \quad (3.37)$$

in which

$$S[\vec{v} + \vec{A}(t) - \vec{A}(t'), t, t'] = \int_{t'}^t dt'' \left[ \frac{1}{2} (\vec{v} + \vec{A}(t) - \vec{A}(t''))^2 + I_p \right] \quad (3.38)$$

is the quasiclassical action. Introducing the canonical momentum

$$\vec{p} = \vec{v} + \vec{A}(t) \quad (3.39)$$

yields the final expression

$$\vec{r}(t) = i \int_{-\infty}^t dt' \int d^3\vec{p} a^*(t) \vec{d}^*[\vec{p} - \vec{A}(t)] e^{-iS(\vec{p}, t, t')} a(t') \vec{E}(t') \vec{d}[\vec{p} - \vec{A}(t')] + c.c. \quad (3.40)$$

where

$$S[\vec{p}, t, t'] = \int_{t'}^t dt'' \left[ \frac{1}{2} (\vec{p} - \vec{A}(t''))^2 + I_p \right] \quad (3.41)$$

The high harmonic generation spectrum can be obtained by performing a Fourier transform on  $\vec{r}(t)$ . Eq. (3.40) has a clear physical interpretation.  $\vec{E}(t') \vec{d}[\vec{p} - \vec{A}(t')]$  is the probability amplitude of an electron making a transition into the continuum with canonical momentum  $\vec{p}$ . The electron wave function then propagates in the laser field and acquires a phase factor  $e^{-iS(\vec{p}, t, t')}$  up to time  $t'$ , the moment it recombines with the parent ion. The electron recombines with an amplitude of  $\vec{d}^*[\vec{p} - \vec{A}(t)]$ . The integral over  $\vec{p}$  in Eq. (3.40) can be done approximately with the saddle-point method. Here, we do not elaborate on the detailed deduction procedure, but only a few of the important insights are introduced to show the significance of the quantum theory. First, since the quasiclassical action  $S[\vec{p}, t, t']$  oscillates much faster than all the other

terms in the integral, the major contribution to the integral over  $\vec{p}$  comes from the stationary points of  $S[\vec{p}, t, t']$  where

$$\nabla_{\vec{p}} S(\vec{p}, t, t') = 0 \quad (3.42)$$

Meanwhile,  $\nabla_{\vec{p}} S(\vec{p}, t, t')$  is the difference between the position of the free electron at time  $t$  and  $t'$ ,

$$\nabla_{\vec{p}} S(\vec{p}, t, t') = x(t) - x(t') \quad (3.43)$$

The meaning of this equation is the dominant contribution to the harmonic generation comes from the electron born at  $t'$  and returning to the parent ion at  $t$ . This conclusion justifies the simple picture described in the semiclassical model. After performing the integral over  $\vec{p}$  with the saddle-point method, one has a new expression of the dipole moment  $\vec{r}_{st}$  of which the subscript "st" stands for stationary. The HHG spectrum can be obtained by performing a Fourier transform on  $\vec{r}_{st}$ . The calculation reveals that harmonic emissions are allowed only when electrons with kinetic energy  $E_k = (2N + 1)\hbar\omega_0 - I_p$  have returned to the parent ion and  $(2N + 1)\hbar\omega_0$  is the photon energy of the  $(2N + 1)$ -th harmonic. This conclusion is a manifestation of the energy conservation law and was also already predicted by the semiclassical model. In the limit that  $I_p \ll U_p$ , the quantum model also predicts the same maximum kinetic energy the electron can acquire as the semiclassical model, which is  $3.17U_p$ . New insights can be obtained by performing a saddle-point analysis also on the integral remaining in the expression of the dipole moment Eq. (3.40). The integrals over  $\tau$  and over  $t$  is calculated. The derivatives of  $S(\vec{p}, t, t')$  are then

$$\frac{\partial S(\vec{p}, t, \tau)}{\partial \tau} = \frac{[\vec{p} - \vec{A}(t - \tau)]^2}{2} + I_p = 0 \quad (3.44)$$

$$\frac{\partial S(\vec{p}, t, \tau)}{\partial t} = \frac{[\vec{p} - \vec{A}(t)]^2}{2} - \frac{[\vec{p} - \vec{A}(t - \tau)]^2}{2} = (2N + 1)\hbar\omega_0 \quad (3.45)$$

Let's first look at Eq. (3.45). Considering Eq. (3.44), Eq. (3.45) can be written as

$$\frac{\partial S(\vec{p}, t, \tau)}{\partial t} = \frac{[\vec{p} - \vec{A}(t)]^2}{2} + I_p = (2N + 1)\hbar\omega_0 \quad (3.46)$$

which is simply the energy conservation law and states that the  $(2N + 1)$ -th harmonic comes from electrons with appropriate kinetic energy. The maximum harmonic photon energy, i.e., the cutoff energy, stems from the electrons with maximum return kinetic energy, which is the same as described in the semiclassical model. However, there is a small quantitative difference between the two models. The evaluation of the cutoff energy with the quantum theory is not straightforward. Here only the conclusion is presented and the evaluation procedure is omitted.

First consider the case that  $I_p = 0$ , the cutoff happens at  $(2N + 1)\hbar\omega_0 \approx 3.17U_p$ . Once  $I_p$  is taken into consideration, the situation becomes complicated even when  $I_p \ll U_p$ . The cutoff energy then becomes

$$\hbar\omega_{X,max} = (2N + 1)\hbar\omega_0 \approx 3.17U_p + I_p F(I_p/U_p) \quad (3.47)$$

where  $F(I_p/U_p)$  is a numerical factor which depends on the ratio  $I_p/U_p$ . When  $I_p \ll U_p$ , the cutoff energy expression is written as

$$\hbar\omega_{X,max} = (2N + 1)\hbar\omega_0 \approx 3.17U_p + 1.32I_p \quad (3.48)$$

The modification compared to the semiclassical formula  $\hbar\omega_{X,max} = 3.17U_p + I_p$  is due to the effects of quantum tunneling and quantum diffusion. Since the electron tunnels out of the atom, it must appear in the laser field in some location distant from the origin. When the electron returns to its initial location, it gains extra kinetic energy on the way back to the origin, which manifests itself as the modification on the cutoff energy formula. Beside the cutoff energy, a few more other features on the HHG spectrum can be understood by making some small corrections to the theory. For example, by taking into account ground-state depletion, the HHG spectrum yield decreases. Corrections on the ionization step and the recombination step have been also developed.

### 3.1.3 Phase matching in high harmonic generation

In the previous two sections, both the semiclassical model and the quantum model of HHG have been discussed. These are models describing the single-atom response. When the intense laser pulse interacts with the gas target, which has a finite volume, each individual atom in the gas target is a XUV photon emitter. However, only when the XUV pulses from the atoms in different positions are in phase, the XUV pulses can add up constructively and thus allow the maximum HHG output. When these conditions are fulfilled, the high harmonic process is phase matched. In order to obtain the phase of the XUV pulses from each atom and find out the experimental condition for achieving phase matching, one can solve the wave propagation equation for the XUV pulses [40, 9].

We start from the Maxwell equations and assume that the laser field is linearly polarized. Under the paraxial approximation and slowly varying envelope approximation (SVEA) [39], we can arrive at the wave equation for the complex field amplitude, assuming the pulse propagates along  $z$  direction

$$\nabla_T^2 \tilde{A}_q(\vec{r}) - 2ik_q \frac{\partial}{\partial z} \tilde{A}_q(\vec{r}) = -\mu_0 \omega_q^2 \tilde{P}_q(\vec{r}) e^{i(k_q - qk_1)z} \quad (3.49)$$

in which  $\tilde{A}_q(\vec{r})$  and  $\tilde{P}_q(\vec{r})$  are the complex amplitude of the electric field of the  $q$ th harmonic and the polarization generating the  $q$ th harmonic, which are given by

$$E_q(\vec{r}) = \tilde{A}_q(\vec{r})e^{-ik_q z} \quad (3.50)$$

$$P_q(\vec{r}) = \tilde{P}_q(\vec{r})e^{-iqk_1 z} \quad (3.51)$$

$k_1$  is the propagation constant of the driving laser field,  $k_q = \frac{\omega_q}{c}\sqrt{\epsilon^{(1)}(\omega_q)}$  is the propagation constant of the  $q$ th harmonic,  $\omega_1$  and  $\omega_q = q\omega_1$  are the angular frequency of the driving laser field and the  $q$ th harmonic, respectively,  $\mu_0$  is the vacuum permeability.  $\epsilon^{(1)}$  is defined as follows: the electric polarization can be separated into the linear polarization and the nonlinear polarization

$$\vec{P}(\vec{r}, t) = \vec{P}^{(1)}(\vec{r}, t) + \vec{P}^{NL}(\vec{r}, t) \quad (3.52)$$

in which  $\vec{P}^{(1)}(\vec{r}, t) = \epsilon_0\chi^{(1)}E(\vec{r}, t)$ ,  $\chi^{(1)}$  is the linear susceptibility and  $E(\vec{r}, t)$  is the total electric field. Finally, we have

$$\epsilon^{(1)} = 1 + \chi^{(1)} \quad (3.53)$$

One can further simplify the situation by assuming that the field is a plane wave, then the wave propagation equation (3.49) becomes

$$2ik_q \frac{\partial}{\partial z} \tilde{A}_q(\vec{r}) = \mu_0 \omega_q^2 \tilde{P}_q(\tilde{A}_1) e^{i(k_q - qk_1)z} \quad (3.54)$$

in which  $\tilde{P}_q(\vec{r})$  is rewritten as  $\tilde{P}_q(\tilde{A}_1)$ , which states that the nonlinear polarization is only determined by the driving laser field. The justification of this is that, although  $\tilde{P}_q(\vec{r})$  is determined by the total electric field, the nonlinear polarization is almost entirely induced by the driving laser field due to the extremely low high harmonic conversion efficiency.

Rewriting the propagation constant as a complex number

$$\tilde{k}_q = \frac{\omega_q}{c}\sqrt{\epsilon^{(1)}(\omega_q)} = \frac{\omega_q}{c}[n_{real}(\omega_q) - in_{imag}(\omega_q)] \quad (3.55)$$

one can have the  $q$ th harmonic complex field amplitude

$$\tilde{A}_q(\vec{r}) = -i \frac{\mu_0 \omega_q^2}{2\tilde{k}_q} \int_0^z \tilde{P}_q(A_1) e^{i\Delta k_q z} e^{-\alpha_q z} dz \quad (3.56)$$

in which  $\Delta k_q = \frac{\omega_q}{c}n_{real}(\omega_q) - qk_1$  is the phase mismatch and  $\alpha_q = \frac{\omega_q}{c}n_{imag}(\omega_q)$  the absorption coefficient of the  $q$ th harmonic, respectively. The field amplitude of the driver laser  $\tilde{A}_1$  stays virtually unchanged during propagation since the extremely low conversion efficiency to the

high harmonic fields. One can safely assume the phase of  $\tilde{A}_1$  is constant and equals to zero. Thus,  $\tilde{A}_1$  can be simply written as a real valued  $A_1$  as in Eq. (3.56).

In the case that there is no absorption, Eq. (3.56) becomes

$$\tilde{A}_q(\vec{r}) = -i \frac{\mu_0 \omega_q^2}{2\tilde{k}_q} \int_0^z \tilde{P}_q(A_1) e^{i\Delta k_q z} dz \quad (3.57)$$

and the perfect phase matching condition is then

$$\frac{d}{dz}[\Delta k_q z] = \frac{d}{dz}[\varphi_{P,q}(z) - \varphi_q(z)] = 0 \quad (3.58)$$

in which  $\varphi_{P,q}(z) = \frac{\omega_q}{c} n_{real}(\omega_q) z$  is the phase of the polarization generating the  $q$ th harmonics and  $\varphi_q(z) = \frac{\omega_q}{c} z$  is the phase of  $q$ th harmonic field generated before current position. From Eq. (3.58), one can see that perfect phase matching means the polarization and the harmonic field have the same phase velocity, which means the newly generated harmonic field is always in phase with the harmonic field generated before.

Ionization always happens in the HHG process. The plasma created in the HHG process changes the overall refractive index. The free electron density of the plasma create in most HHG experiments is small. Therefore, the absorption of the plasma is neglected since the plasma frequency is lower than the laser frequency and the HHG field. Taking into account the contribution from the neutral gas and the plasma, the overall refractive index  $n_{real}$  of the gas medium for the driving laser field is

$$n_{real}(\omega_1) = 1 + \frac{e^2 N}{2\epsilon_0 m_e} \left( \frac{1-p}{\omega_r^2 - \omega_1^2} - \frac{p}{\omega_1^2} \right) \quad (3.59)$$

where  $p$  is the ionization probability and  $\omega_r$  is the resonance frequency specific to the species of the gas used for HHG. The refractive index for the high-order harmonics is close to 1, i.e.,  $n_{real}(\omega_q) \approx 1$ . Under the phase matching condition  $n_{real}(\omega_1) = n_{real}(\omega_q)$ , we have

$$p = \left( \frac{\omega_1}{\omega_r} \right)^2 \quad (3.60)$$

which means that one can control the ionization probability to achieve phase matching.

Different from a plane wave, the laser fields used for HHG experiments are usually Gaussian beams. Therefore, it is also important to look at the phase matching when using a Gaussian beam. It was proven that, in order to achieve phase matching when Gaussian beam is used, the

gas target for HHG process must be placed at position  $z$  given by

$$z = z_R \left[ \frac{\alpha I_0}{q} \pm \sqrt{\left( \frac{\alpha I_0}{q} \right)^2 - 1} \right] \quad (3.61)$$

where  $I_0$  is the intensity of the driving laser field,  $\alpha$  is the coefficient that relates the intrinsic phase to the intensity of the driving laser field. One can see that for the solution to be real,  $I_0 \geq q/\alpha$ .  $\alpha$  has different values for short-trajectory electrons and long-trajectory electrons, which can be exploited to selectively phase match the HHG from either short or long trajectories.

### 3.1.4 Experimental apparatus and experimental methods for high harmonic generation

In this section, the experimental apparatus for HHG constructed by the author is discussed in detail. Overall, the ultrafast pulses are focused down to achieve the intensity required for HHG. The generated XUV beam is measured with an XUV spectrometer. The optics mounts and other components for the experiments are mounted on optical breadboards, which are placed on top of an optical table with pneumatic vibration isolation stands. The XUV photons generated are well located in the range of high absorption in air allowing only very short propagation distance. In order to avoid absorption by air, the XUV portion of the beam path needs to be placed in a vacuum environment. The vacuum pumps of the beamline are decoupled from the optical setup for optimum vibration isolation and thus allowing good passive stability of the optical setup.

#### Vacuum system

The XUV beam has very short absorption length in air as shown in Fig. 3.6. As a result, the XUV beam path has to be placed in a vacuum environment. The vacuum system consists of two custom designed experimental vacuum chambers, an XUV spectrometer chamber and an electron time-of-flight spectrometer as shown in Fig. 3.8. The first vacuum chamber (HHG chamber) houses the HHG gas target and optics for the IR driver pulses. Meanwhile, the second vacuum chamber (TM chamber) houses the optics for other experiments, e.g., a toroidal mirror (TM), which will be discussed later in the thesis. The XUV grating and the XUV CCD camera are located inside the XUV spectrometer chamber.

In general, constructing vacuum systems with a vacuum level required for XUV beam propagation is not particularly technically challenging. However, the distinct feature of a vacuum system for HHG experiments is that the gas target for HHG continuously feeds gas



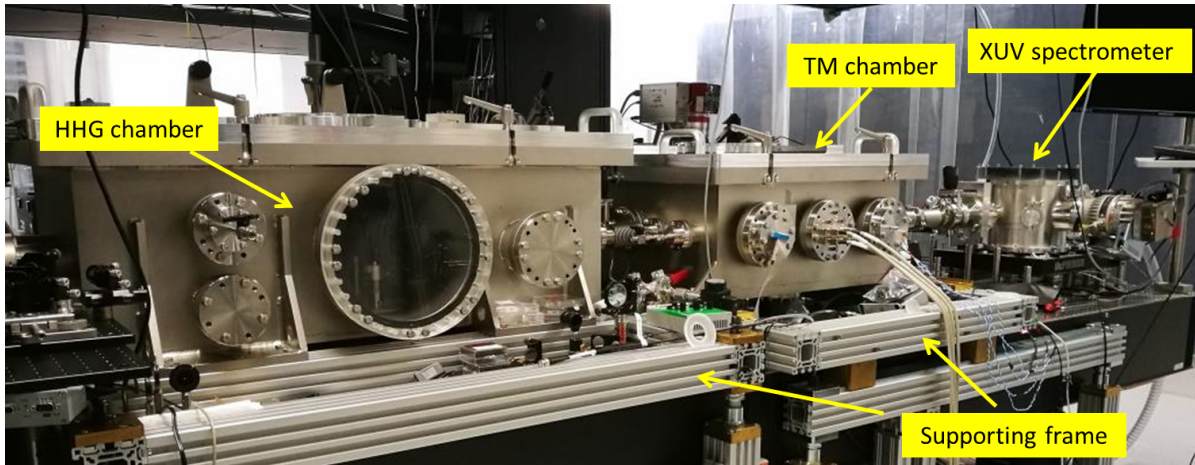


**Fig. 3.5** Photo of the vacuum chambers and the XUV spectrometer. From left to right: the first chamber is the chamber housing the HHG gas target (HHG chamber), the second chamber is the chamber housing the toroidal mirror XUV optics (TM chamber), and the third chamber is the XUV spectrometer.

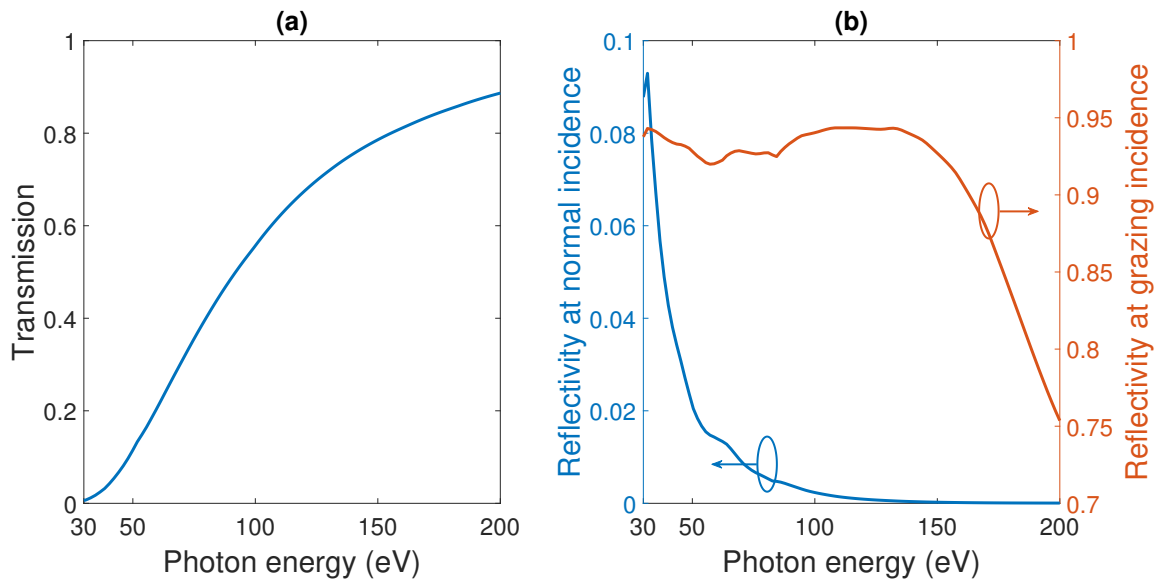


**Fig. 3.6** XUV transmission and reflectivity of materials. (a) XUV transmission through  $100\ \mu\text{m}$  of air at 1 bar. (b) XUV reflectivity of gold coated mirror at different incident angles. At normal incidence (blue), the reflectivity is very low. At  $2^\circ$  incident angle (grazing incidence), the reflectivity is rather high and flat over a broad bandwidth (red).

into the vacuum environment, which means that the vacuum system has a severe leak. Vacuum pumps with high pumping capacity need to be utilized to maintain the desired vacuum level. A Pfeiffer Vacuum HiPace 1500 turbo pump which has a pumping speed of 1450 l/s is mounted onto the HHG chamber to this end. In order to achieve a better vacuum level in the other sections of the vacuum system, small pinholes are used between the two vacuum chambers for differential pumping. There are in total two turbo pumps, including one Pfeiffer Vacuum HiPace 400 and one Pfeiffer Vacuum HiPace 300, mounted onto the second vacuum chamber. These vacuum pumps have pumping speeds of 355 l/s and 260 l/s, respectively. Another Pfeiffer Vacuum HiPace 300M turbo pump is used to maintain the good vacuum at the site of the MCP detector in the time-of-flight spectrometer. The vacuum environment at the XUV spectrometer is maintained with a Agilent TV 301 Navigator turbo pump which has a pumping speed of 250 l/s. Three Edwards XDS35i scroll pumps are used to provide the pre-vacuum for the turbo pumps. Each scroll pump has a pumping speed up to  $35 \text{ m}^3\text{h}^{-1}$ . Under the typical experiment condition, i.e., the HHG gas target is backed with 100 mbar of argon gas, the vacuum in the first chamber is  $\sim 10^{-4}$  mbar and the vacuum in the second chamber is  $\sim 10^{-5}$  mbar. At the site of the MCP detector of the time-of-flight spectrometer, the vacuum reads  $\sim 10^{-6}$  mbar which is good enough for MCP operation. The vacuum inside the XUV spectrometer is also  $\sim 10^{-6}$  mbar.

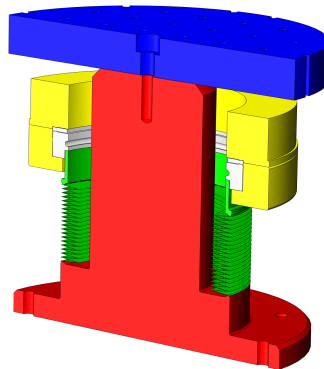


**Fig. 3.7** Design of the vibration isolation vacuum feedthrough. The optical breadboard (blue) is supported by the post (red) which is rigidly fixed to the optical table. Meanwhile, the vacuum chamber (yellow) is connected to the post via a flexible bellow (green). The vacuum enclosure is completed with flexible connection which decouples the vibration of the vacuum chamber to the optical breadboard.

Usually, an optical breadboard in vacuum is mounted rigidly to the vacuum chamber. The vacuum chamber is then positioned on the optical table or mounted onto the floor. In both cases, the mechanical vibrations from the vacuum pumps cause the entire optical setup to vibrate. Notice that the experimental setup is also used for attosecond pulse characterization and attosecond spectroscopy experiments, which require an optical setup with interferometric stability on the attosecond level. However, the vibrations from turbo pumps make interferomet-

ric stability of the whole optical setup of this level impossible. Additional active stabilization feedback loop needs to be implemented for experiments. Active stabilization feedback loop of an interferometer is usually realized by sending a continuous-wave (CW) laser, e.g., a He-Ne laser, through both arms of the interferometer. The interference fringes created by combining the beams from both interferometer arms are then used as a signal for active stabilization. The typical drawback of an active feedback loop is there is always a bandwidth limitation. Another difficulty to the interferometer stems from the fact that one of the interferometer arms is opaque for the CW laser. In one of the interferometer arms, a thin metallic filter used for separating the XUV beam from the IR driving beam also prevents the CW laser beam from transmission. Due to this, an active stabilization feedback loop covering all the optics is difficult to implement.

The vibration decoupling design, as shown in Fig. 3.7, provides superb passive stability to the optical setup which allows us to avoid using an active stabilization feedback loop. The vacuum chambers are mounted on separate aluminum-profile frames which are fixed onto the floor. Meanwhile, the optical breadboard in each chamber is supported by three posts which are mounted on the optical table. The vacuum enclosure is completed by means of flexible bellows, which connect the vacuum chamber body to the posts. The configuration decouples the vibrations from the vacuum pumps to the optical layout and allows the optical setup to have outstanding passive stability. In the meantime, another design feature provides flexibility to the experimental apparatus. Brass slide plates are placed between the second vacuum chamber and the supporting frame, which allows one to easily slide the second vacuum chamber along two directions in the horizontal plane. The entire system can then be configured according to various requirements of different experiments.

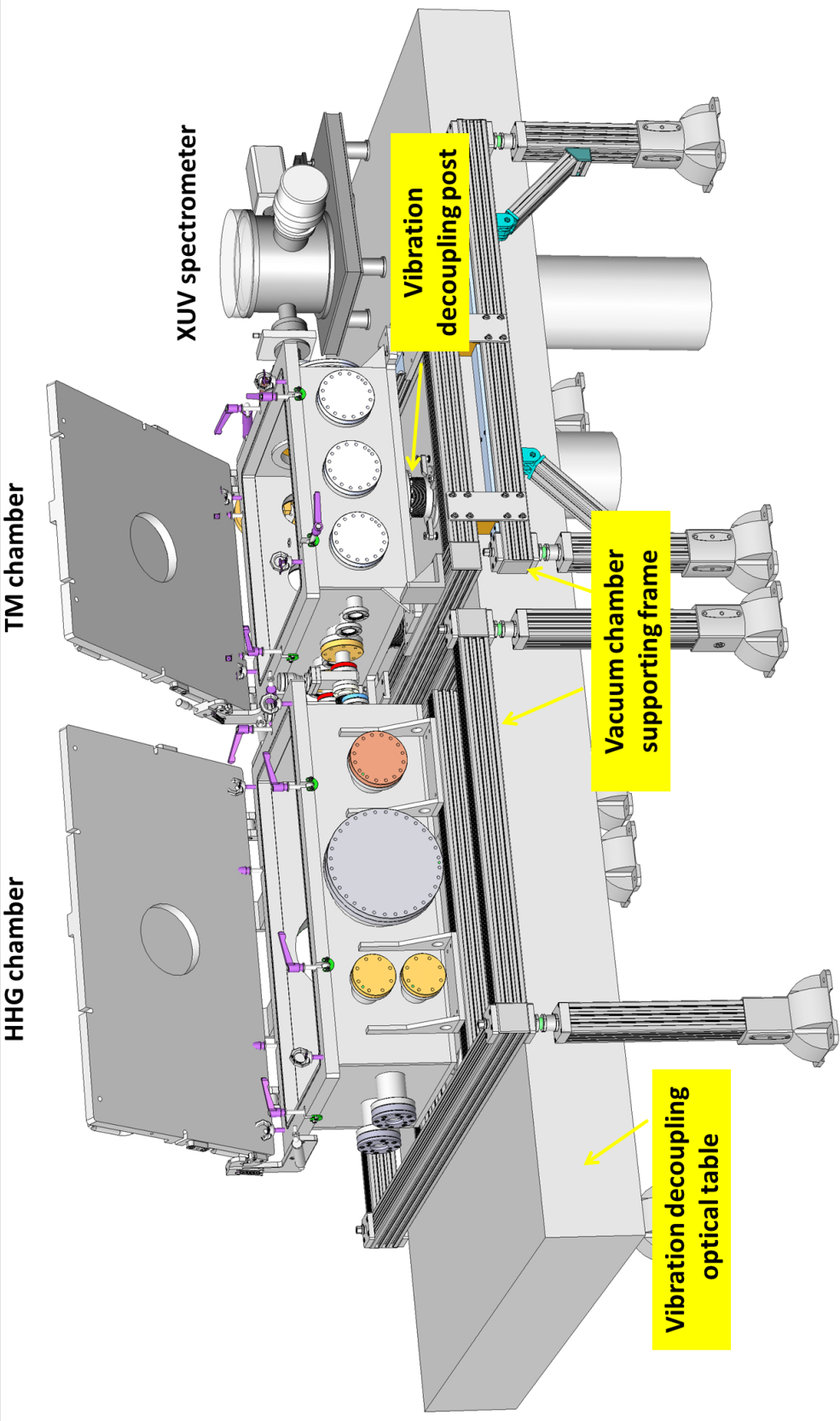


Fig. 3.8 CAD drawing of the experimental setup configuration

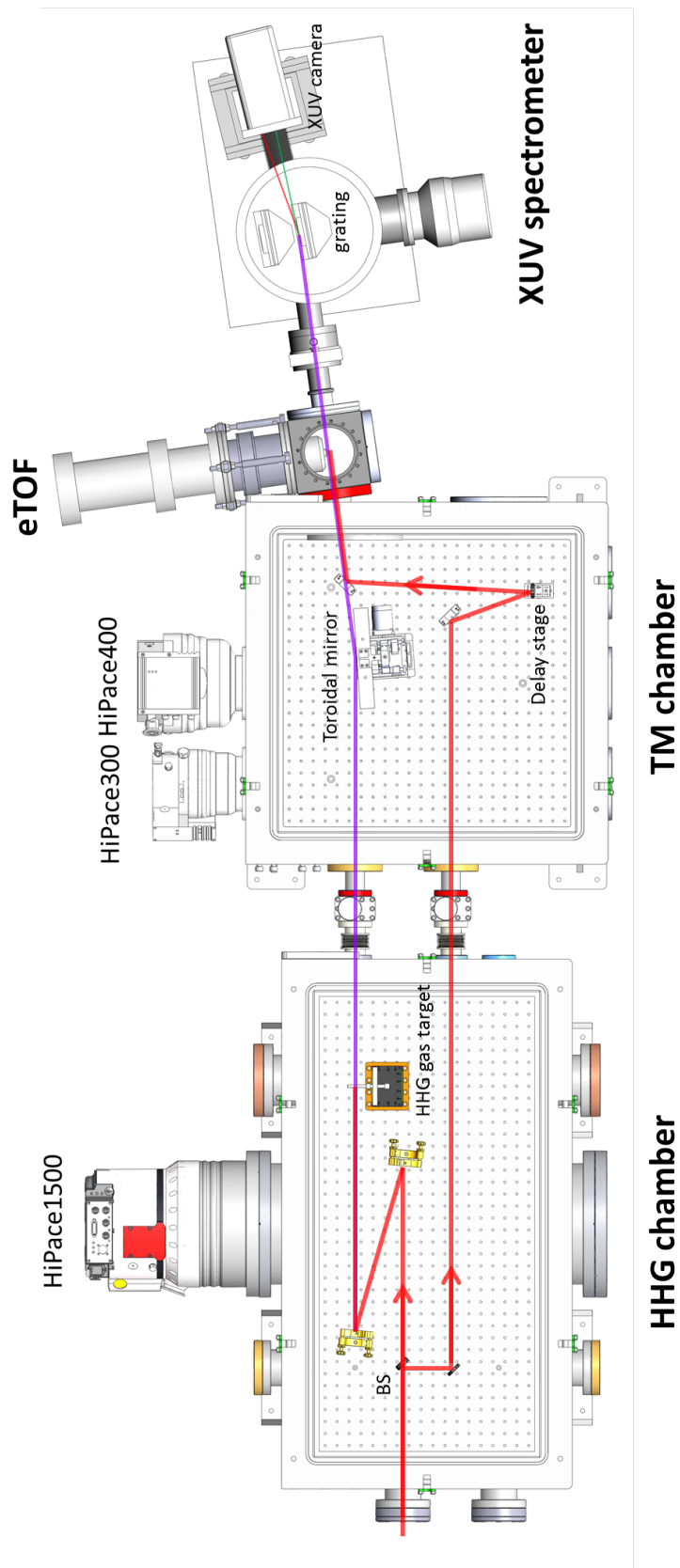
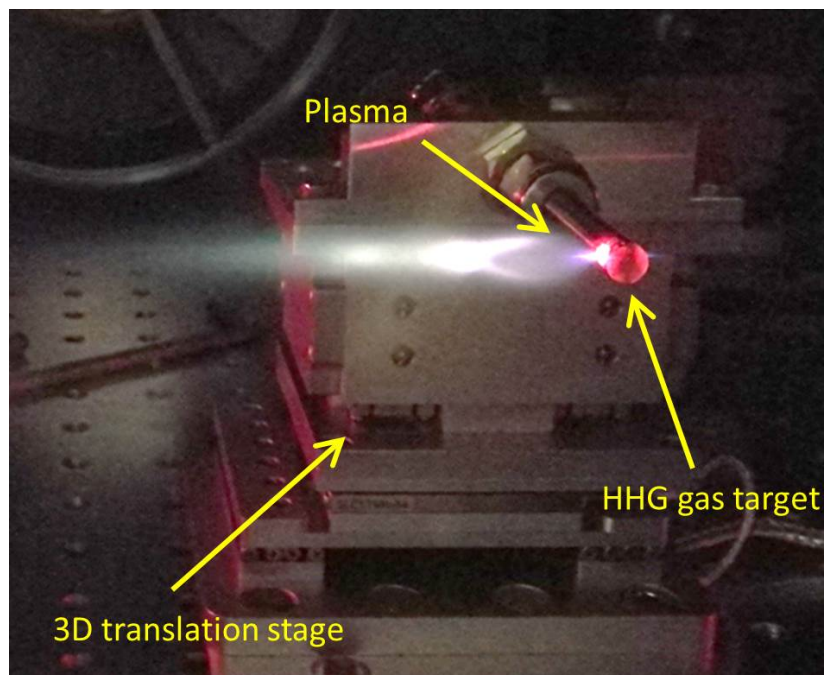


Fig. 3.9 Optical configuration of the experimental apparatus.

### Optical beam path layout

Depending on the targeted experiment, either 35-fs long pulses directly from the Ti:sapphire CPA system or sub-6 fs few-cycle pulses from the HCF compressor (HCF pulses) can be used for HHG. The entire optical configuration inside the experimental apparatus is shown in Fig. 3.9. The entrance window of the vacuum chamber is a piece of 1-mm-thick fused silica plate, whose dispersion also needs to be taken into account when using the few-cycle pulses. The energy of the CPA pulses for the experiments can be adjusted with a variable attenuator consisting of a half-waveplate and a polarizer. Usually, a reflecting thin-film polarizer is used for this purpose due to the high damage threshold and low dispersion. For the case of HCF pulses, it becomes more difficult to use waveplates and thin-film polarizers due to the broad bandwidth of few-cycle pulses. Usually, an iris diaphragm is used to control the pulse energy. This, however, brings about some problem since the iris diaphragm changes the pulse energy and the beam profile at the same time. The change of the beam profile inevitably changes the focal profile/position and affects the HHG process in various other ways. The interaction makes it more difficult to control the experiment and analyze the experimental outcomes.



**Fig. 3.10** Picture of the HHG gas target. The gas target follows a conventional semi-finite gas-cell design. It is a steel tube with 4-mm inner diameter and sealed at one end. Two pre-drilled 1-mm holes on the tube allow the focused laser beam to pass through. In the picture, one can see the plasma plume created by the focused laser.



The laser pulses are then focused into a gas target for HHG. A spherical mirror is used for focusing. Several factors, e.g., the required intensity, a long Rayleigh length, and keeping the entire dimension of the whole beamline setup within a reasonable size, need to be taken into consideration when choosing the focal length.

The gas target follows a conventional gas tube design. It is a steel tube with 4-mm inner diameter and sealed at one end. Two pre-drilled 1-mm holes on the tube allow the focused laser beam to pass through. The tube is mounted on a three-dimensional translation stage to optimize the HHG signal. The gas target is moved in the plane perpendicular to the laser propagation direction for centering the drilled hole to the laser beam and along the laser propagation direction to fulfill the desired phase matching condition. The backing gas pressure is monitored with a gas gauge right outside of the vacuum chamber. It needs to be noticed that the backing pressure is not necessarily the gas pressure in the HHG interaction volume. Calibration is required to determine the relation between the backing pressure and the real gas pressure for HHG.

After the XUV generation, the beam will encounter no optics before it reaches the XUV spectrometer. Common optics used for laser applications are not suitable for XUV beams. XUV photons will be severely absorbed by common optics. Only specialized XUV optics can be used in this wavelength range, and XUV optics are typically only used in reflection.

### **XUV spectrometer**

The XUV spectrometer used in our beamline is a McPherson 251MX XUV spectrometer from as shown in Fig. 3.11. The spectrometer is equipped with two concave varied line-spacing (VLS) flat-field gratings. Using the concave grating with varied groove spacing, the diffracted rays focus sharply onto a plane. The grating holder allows switching between different gratings under vacuum operation via the grating switching handle. One grating has a nominal groove density of 300 groove/mm and covers 20-80 nm (15.5-62 eV) spectral range. While the second grating has a nominal groove density of 1200 groove/mm and covers spectral range of 5-20 nm (62-248 eV). There is another currently unmounted grating available in our lab for other experiments. The third grating has 2000 groove/mm and covers the even higher photon energy range of 1-5 nm (248-1240 eV). At the entrance of the spectrometer, a filter wheel is located, which contains several thin metallic filters. After the HHG gas target, the XUV beam and the laser pulses propagate collinearly towards the XUV spectrometer. Since the HHG efficiency is extremely low, which is on the order of  $\eta = 10^{-6}$ , the XUV signal observed with the XUV spectrometer will be buried under the driving laser background signal. The metallic filters block the laser pulses while allowing substantial transmission of the XUV beam. The XUV beam will then go through an adjustable slit and a fixed opening. These two apertures fix the

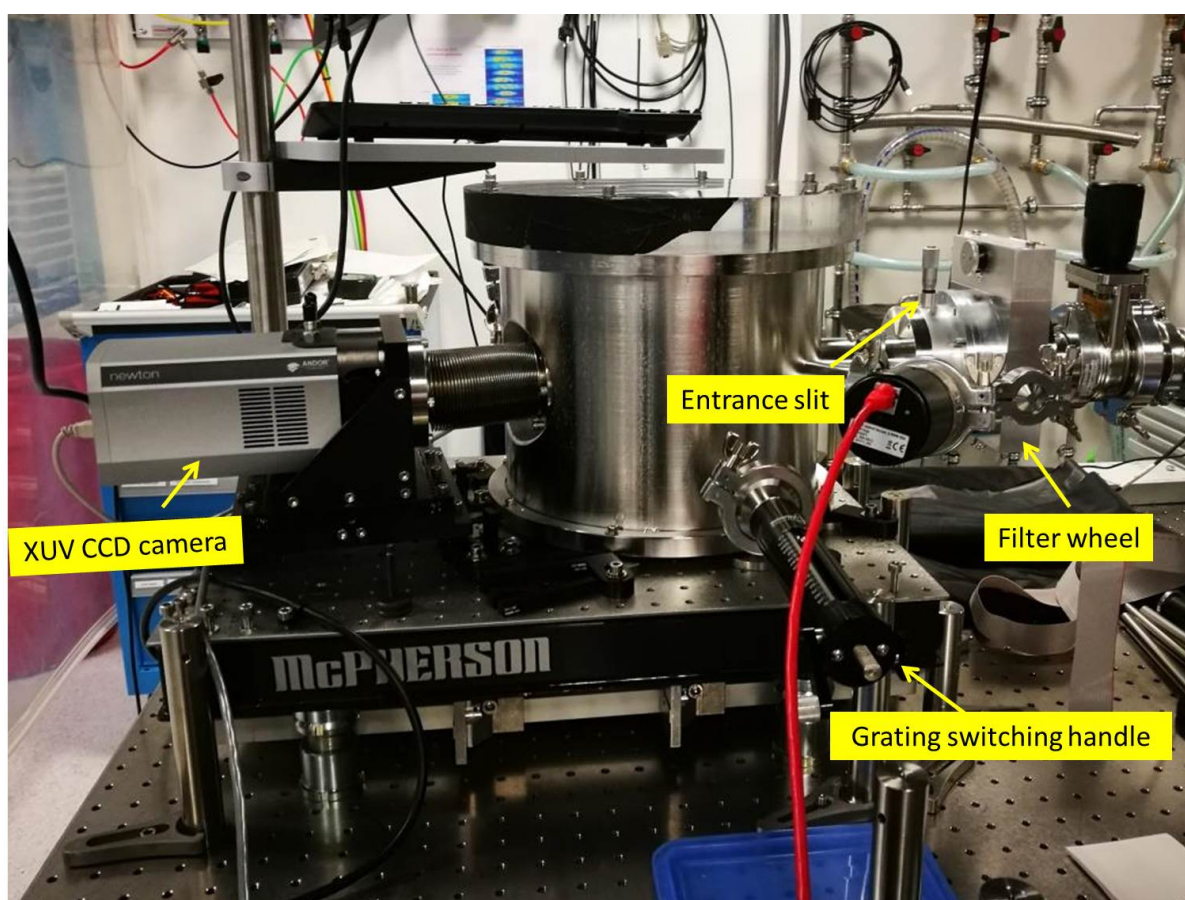


**Fig. 3.11** McPherson 251MX XUV spectrometer equipped with an Andor Newton 940 XUV CCD camera



beam pointing and the incident angle on the grating. Another aperture is mounted on each of the grating mount which allows one to center the grating respect with the incident beam. The XUV grating is used in grazing incidence to achieve sufficient reflectivity, since, under small incident angle, materials usually show strong absorption for XUV photons as shown in Fig. 3.6(b). After the XUV pulses are dispersed by the grating, the XUV spectrum is then detected with a XUV CCD camera. The XUV camera is a Newton 940 back-illuminated CCD with 2048 by 512 pixels from Andor Technology Ltd. The pixel size is  $13.5 \mu\text{m}$  by  $13.5 \mu\text{m}$ . The camera can be cooled down to  $-60^\circ\text{C}$  with air-cooling and  $-100^\circ\text{C}$  with water-cooling for dark current suppression. A zeroth-order baffle is placed in front of the CCD camera to block the zeroth diffraction order of the grating. It is used to prevent the zeroth diffraction order of the grating from reaching the detector and burying the first diffraction order of the grating in which one is interested.

To measure the HHG spectrum with the XUV spectrometer, one important issue worth extra mentioning is a wavelength calibration is one important issue which worth extra attention. In a usual compact spectrometer used to measure the laser spectrum, the geometry of the spectrometer, i.e. the relative location between the grating and the detector is fixed. Once the calibration is carried out for this kind of spectrometers, it can be reused for succeeding experiments. Even if the calibration is compromised for some reasons, it is easy to find a wavelength standard in the laboratory for recalibration. For example, He-Ne laser can provide a narrow spectral line at 632.8 nm, while the spectrum of common fluorescent lamps has a set of spectral lines from mercury (Hg), e.g., 435.8 nm and 546 nm. However, to correct for the frequency dependent response of the detector, one would need a calibration lamp.

In contrast, wavelength calibration for an XUV spectrometer is a lot more complicated. The source in this spectral range is either an expensive gas discharge source or a large photon-science facility such as a synchrotron. In our XUV spectrometer, in order to cover the wide spectral range, the CCD camera has to move along the grating image plane for measuring different wavelength regions. Moreover, the fact that the location of the spectrometer needs to change for different experiments makes the situation even more complicated. A slight change on the incident beam pointing into the spectrometer and a slightly different detector position will add up to the wavelength calibration error. A self-calibration for each measurement is crucial to keep the experimental results valid. In fact, the metallic thin filter in front of the slit can be exploited to serve another purpose. The thin filters have an absorption edge in the XUV, which can be used as the wavelength calibration reference. Making use of absorption edges is not as straightforward as it seems. The problem at hand is that, for multi-cycle driver pulses, the HHG spectrum is not a continuum rather than a set of spectral peaks. Making use of the absorption edge requires that the spectrum is non-zero surrounding the absorption edge. On

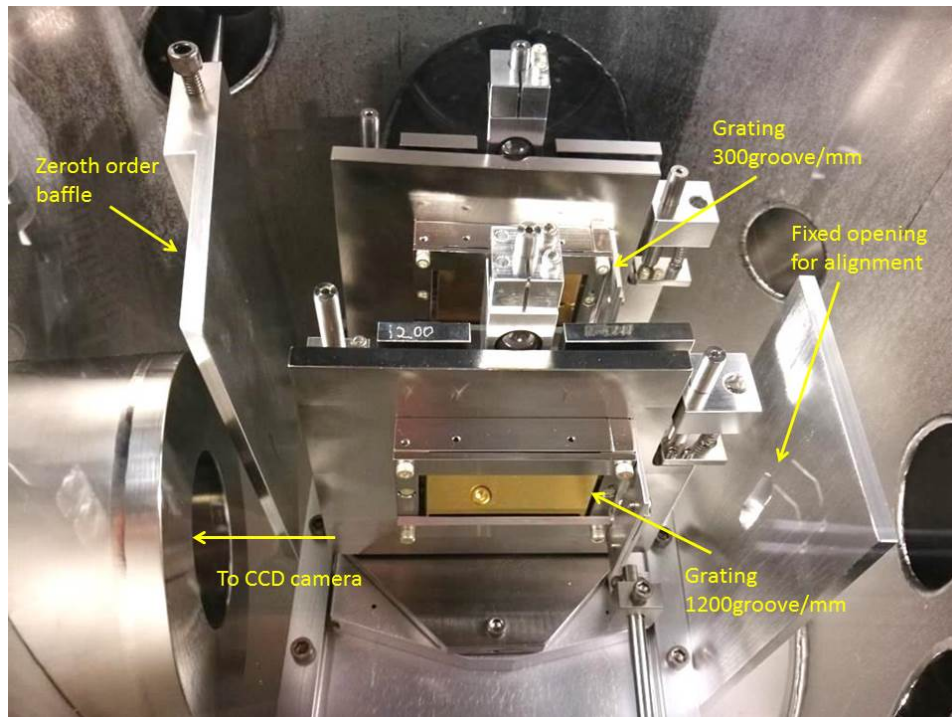


**Fig. 3.12** Photo of the McPherson 251MX XUV spectrometer gratings. There are two varied line-spacing (VLS) flat-field grating mounted inside the spectrometer. One has nominal groove density of 300 groove/mm and covers the spectral range of 20-80 nm (15.5-62 eV). The other grating has nominal groove density of 1200 groove/mm and covers the spectral range of 5-20 nm (62-248 eV). The grating mounting configuration allows one to switch between two gratings under vacuum environment via the grating switching handle as shown in Fig. 3.11. The zeroth order block can be moved in with a mechanical manipulator under vacuum environment to block the zeroth diffraction order of the grating. Since the zeroth diffraction order carries lots of energy which would bury out the first diffraction order signal if not blocked.

the other hand, one can make use of the harmonic peak structure of the HHG spectrum for wavelength calibration. The HHG spectrum consists of spectral spikes locating at odd harmonic order of the fundamental frequency. However, the photon energy of the fundamental beam is difficult to determine when ultrashort and maybe not perfectly compressed pulses are used. Here, the wavelength calibration is performed without assuming the fundamental photon energy. The first diffraction order of the grating is used for XUV spectrum measurement. In addition, the second diffraction order of the grating is usually also visible in some range due to the fact that every grating in the XUV spectrometer covers more than one octave. Although there is still no absolute wavelength reference, the 1st diffraction order and the 2nd diffraction order of the same HHG order can be regarded as a relative wavelength reference. Combined with the diffraction grating equation, the wavelength calibration can be performed. By switching between different metallic filters, the wavelength calibration can be further improved.

### 3.1.5 HHG experimental results

Isolated attosecond XUV pulse generation is based on the HHG process. To construct and test a new attosecond beamline, HHG experiments with multi-cycle pulses were performed as a first step. The HHG beam profile can be observed by placing the CCD in the zeroth diffraction order of the grating, see Fig. 3.13. The measurement was performed with 10-fs HCF pulses. The pulse energy is 0.53 mJ and the beam is focused with a  $f=500$  mm spherical mirror. The HHG gas target is backed with 200 mbar of neon. Two stacked 300-nm thick aluminum filters are used to block the IR driving beam. The vertical shape edges in the figure are the image of the spectrometer entrance slit. Two speckles on the beam profile stem from imperfections of the thin metallic filters. The slit is at its maximum opening of 3 mm, which can be used to estimate the beam size of the XUV beam at the slit. The beam is centered at the slit and has not been blocked by any other apertures, which means the beam is well aligned inside the XUV spectrometer. The zeroth diffraction order is used not only as an indicator of good alignment but also an indicator of HHG phase matching. The beam profile shown in Fig. 3.13 is very close to a Gaussian beam profile, which indicates that the beam is well phase-matched for short-trajectory HHG.

Although the HHG spectrum is usually visualized in 1-D, it is also beneficial to look at the 2-D image of the diffracted HHG signal via the CCD camera. A 2-D CCD image is shown in Fig. 3.14. The experimental conditions are identical to the conditions for Fig. 3.13 except for the gas target position. In Fig. 3.13, the gas target is positioned after the laser focus for selecting the short-trajectory HHG. While in Fig. 3.14, the gas target is located in a position that the long-trajectory HHG and short-trajectory HHG both present. The solid yellow rectangle indicates the short-trajectory HHG which is located close to the center of the beam. Meanwhile,

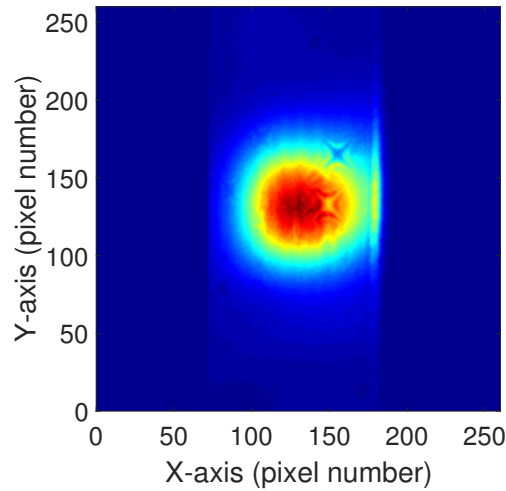


**Fig. 3.13** HHG beam profile observed via the zeroth diffraction order beam from the grating. The measurement was performed with 10-fs HCF pulses. The pulse energy is 0.53 mJ and the beam is focused with a  $f=500$  mm spherical mirror. The HHG gas target is backed with 200 mbar of neon. Two 300-nm thick aluminum filters are used to block the IR driving beam. The vertical shape edges in the figure are the image of the spectrometer entrance slit.

the dashed yellow rectangle marks the long-trajectory HHG which is spatially and spectrally displaced from the short-trajectory HHG [72]. The red vertical line shows the absorption edge of the aluminum thin filter which locates at  $\sim 73$  eV.

One of the most important steps in the data acquisition is to perform the wavelength calibration, i.e., to convert the pixel number to the corresponding wavelength. As stated above, one can make use of the 1<sup>st</sup> and the 2<sup>nd</sup> diffraction grating to accomplish the wavelength calibration. Here, the calibration procedure is briefly introduced. In Fig. 3.15, two measurements of an identical HHG spectrum are shown. 35-fs long laser pulses with pulse energy of  $\sim 1$  mJ is focused into the HHG gas target, which is backed with 200 mbar of neon gas. The focal length of the mirror is 250 mm. Different filters placed in front of the XUV spectrometer lead to the different measured spectra. In Fig. 3.15(a), the XUV beam is filtered by a 300-nm thick zirconium filter. Whereas, in Fig. 3.15(b), the XUV beam is filtered by a 300-nm thick zirconium filter and a 500-nm thick silicon filter. Zirconium filter are used in both cases for blocking the IR driving field. Silicon has its L-absorption edge at 100 eV, see Fig. 3.16(b), which is indicated by a red line in Fig. 3.15(a). It can be clearly seen that, in Fig. 3.15(b), any harmonic lines with energy above 100 eV are absorbed by the silicon filter. The yellow arrows indicate the 1<sup>st</sup> diffraction order and the 2<sup>nd</sup> diffraction order of the harmonic order which is closest to the silicon absorption edge. In the following, the 1<sup>st</sup> diffraction order of this particular harmonic order is referred to as H1 while the 2<sup>nd</sup> diffraction order is referred to as H2. In this way,

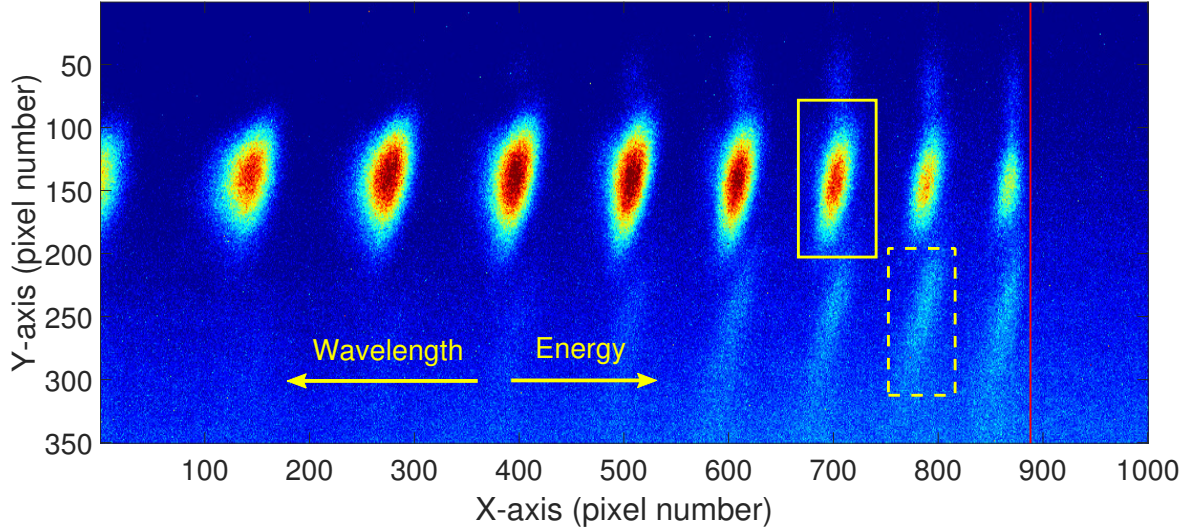


**Fig. 3.14** 2-D image of the diffracted HHG signal via the CCD camera. The experiment conditions are identical as the conditions for Fig. 3.13 except for the gas target position. The solid line yellow rectangular indicates the short-trajectory HHG, which locates close to the center of the beam. At the same time, the dashed line yellow rectangular marks the long-trajectory HHG. The red vertical line shows the absorption edge of the aluminum thin filter located at  $\sim 73$  eV.

one can be certain about the spectral spikes chosen are indeed different diffraction orders of one single harmonic line. Since the XUV beam experiences more attenuation in the second measurement, it takes more exposure time for the measurement. It takes 1 s of exposure for Fig. 3.15(a), while the exposure time of Fig. 3.15(b) is 3 s.

Usually, one can integrate over the center portion of the beam to locate the peak more accurately. Integration over only the center portion of the beam excludes the contribution from the long-trajectory HHG. The HHG spectrum taken with only zirconium filter (blue) and the HHG spectrum taken with both zirconium filter and silicon filter (red) are shown together in Fig. 3.16(a). The arrows point at the same positions as the arrows in Fig. 3.15(b). In Fig. 3.16(b), the transmission curves of the zirconium filter, the silicon filter and the combination of them are shown. In the energy range shown, zirconium does not have any sharp absorption edge while silicon has a very steep L-edge at 100 eV.

The grating used for measuring the HHG signal shown in Fig. 3.16(a) is the grating with nominal groove density of 1200 grooves/mm and covering 20-80 nm. In Fig. 3.17, the scheme of the grating is shown [74]. The groove spacing  $\sigma$  varies along the grating and is given by

$$\sigma = \sigma_0 / \left( 1 + \frac{2b_2}{R}w + \frac{3b_3}{R^2}w^2 + \frac{4b_4}{R^3}w^3 \right) \quad (3.62)$$



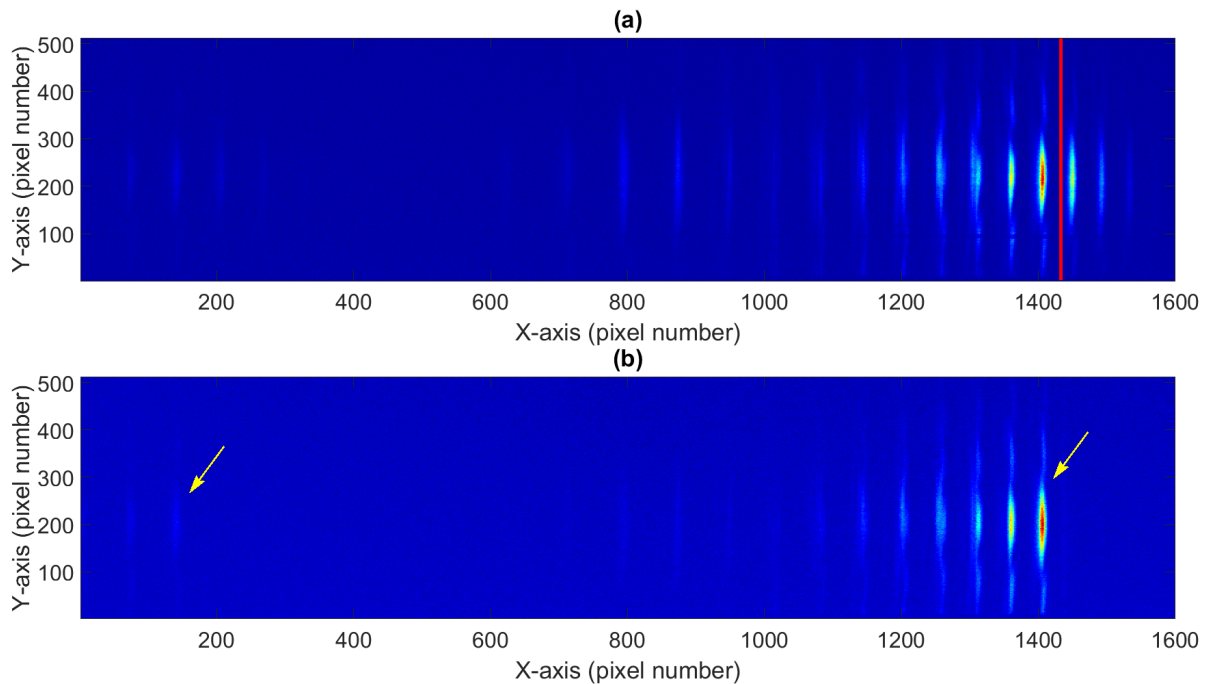


**Fig. 3.15** 2-D image of HHG signal used for wavelength calibration. The HHG spectra are both generated with 35-fs laser pulses with 1 mJ of pulse energy. The HHG gas target is backed with 200 mbar of neon gas. The focal length of the focusing optics is 250 mm. (a) the HHG spectrum is filtered with a 300-nm thick zirconium filter. The red line marks the silicon L- absorption edge at 100 eV. (b) the HHG spectrum is filtered with a 300- nm- thick zirconium filter and a 500- nm- thick silicon filter. The yellow arrows indicate the harmonic order used for wavelength calibration.

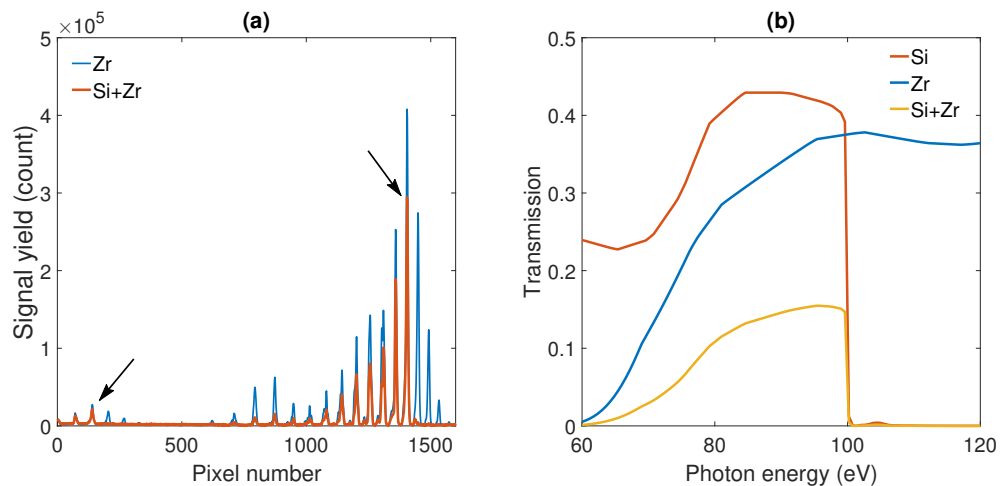


**Fig. 3.16** HHG signal for wavelength calibration and filter transmission. (a) the HHG signal obtained by integrating the 2-D HHG signal, as shown in Fig. 3.15, over the center portion of the beam. The blue curve shows the HHG signal filtered with only the 300 nm zirconium. The red curve shows the HHG signal filtered with both 300 nm zirconium and 500 nm silicon. (b) the transmission of 300 nm zirconium (blue) and 500 nm silicon (red) are shown. The transmission of the combination of both filters is shown as the yellow curve.

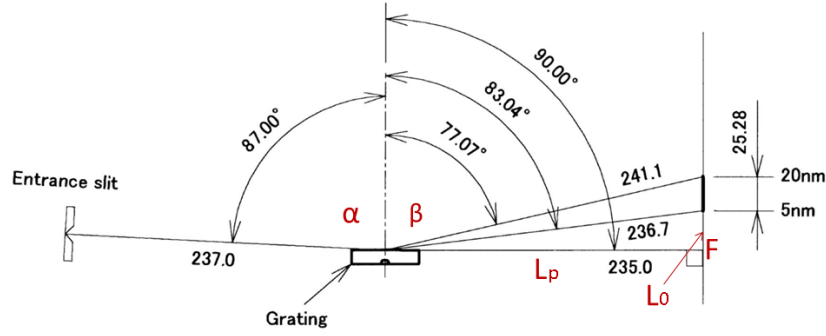


**Fig. 3.17** Schematic of the XUV diffraction grating.  $\alpha$  is the incidence angle,  $\beta$  is the diffraction angle,  $L_p$  is the distance between the center of the grating and the focal plane. The focal plane is parallel to the normal of the grating.  $F$  is the foot of the perpendicular to the focal plane.  $L_0$  is the distance between  $F$  and the CCD.

where  $\sigma_0$  is the nominal groove spacing,  $w$  is the distance measured from the center of the grating to the groove,  $R = 5649$  mm is the radius of curvature of the grating surface,  $b_2, b_3$  and  $b_4$  are the varied-spacing ruling parameters which are  $b_2 = 20$ ,  $b_3 = 4.558 \times 10^2$  and  $b_4 = -1.184 \times 10^4$ , respectively. In spite of the varied groove spacing, the wavelength-dependent diffraction angle  $\beta$  can be simply calculated with the diffraction grating equation using the nominal groove spacing  $\sigma_0$ . The diffraction angle is determined by

$$m\lambda = \sigma_0(\sin \alpha + \sin \beta) \quad (3.63)$$

The distance between  $F$  and the image of H1 is  $L_1$ , and the distance between  $F$  and the image of H2 is  $L_2$ . The wavelength of the harmonic order which is closest and smaller than 100 eV is  $\lambda_0$ . Thus, one can obtain

$$k\lambda_0 = \sigma_0(\sin \alpha + \sin \beta_k) \quad (3.64)$$

$$\cot \beta_k = \frac{L_k}{L_p} \quad (3.65)$$

where  $k = 1, 2$  referring to H1 and H2, respectively. From the measured HHG signal as in Fig. 3.16(a), one can find the length difference  $\Delta L$  between  $L_1$  and  $L_2$ , which is given by

$$\Delta L = |L_2 - L_1| = psize |pnum_2 - pnum_1| \quad (3.66)$$

in which  $psize = 13.5 \mu\text{m}$  is the pixel size of the CCD camera and  $pnum_k$  ( $k = 1, 2$ ) is the pixel number of H1 and H2 on the CCD camera. Taking into account Eq.s (3.64) and (3.65), one can determine the value of  $\lambda_0$  and, more importantly,  $\beta_1$ . Once  $\beta_1$  is known,  $\lambda_1$  is known. Afterwards, the wavelength corresponding to any other position on the detector can be obtained.

In fact, the wavelength calibration is mainly about finding out the distance between  $F$  and the CCD,  $L_0$ , which is the only uncertain parameter in the geometry. One can also perform the above procedure for other harmonic orders and then average over several calculated  $L_0$ . After converting the pixel number axis in Fig. 3.16(a) to photon energy axis, the HHG spectrum is obtained as shown in Fig. 3.18.

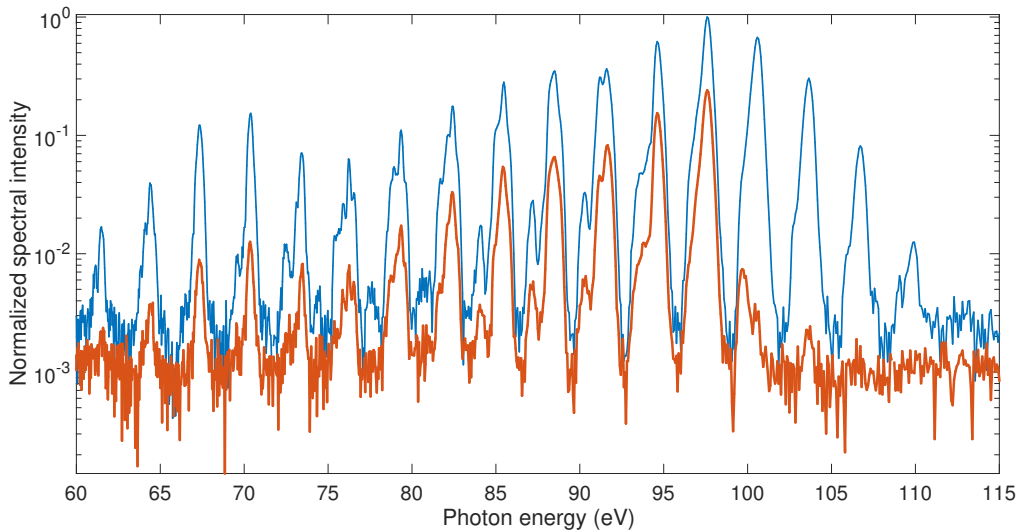


**Fig. 3.18** HHG spectrum obtained after photon energy calibration. The spectra are both normalized with respect to the HHG spectrum filtered with only zirconium filter (blue). The HHG signal is the same one as shown in Fig. 3.16(a). The blue curve shows the HHG spectrum filtered with only the 300 nm zirconium. The red curve shows the HHG spectrum filtered with both 300 nm zirconium and 500 nm silicon.

Neon gas is used as the XUV generation medium in the figures above. Besides neon, other noble gases, e.g., argon and krypton, have been used for HHG in our experiments. In Fig. 3.19, the HHG spectrum generated with argon is shown. The HHG spectrum is generated with 35-fs laser pulses with 1 mJ of pulse energy. The HHG gas target is backed with 280 mbar of argon gas. The focal length of the focusing optics is 500 mm. Two 300-nm thick aluminum filters are used to block the IR driving pulses. Moreover, krypton gas has also been used as HHG medium and the obtained spectrum is shown in Fig. 3.20. The HHG spectrum is generated with 9-fs pulses from the HCF compressor with 0.2 mJ of pulse energy. The HHG gas target is backed with 40 mbar of krypton gas. The focal length of the focusing optics is 500 mm. The XUV beam is filtered with two 300-nm thick aluminum thin foils.

Heavier noble gases have lower ionization potentials and thus they can withstand lower laser intensity before total depletion of the ground-state population. Lower laser intensity means the generated XUV photons have lower photon energy, which can be seen from the



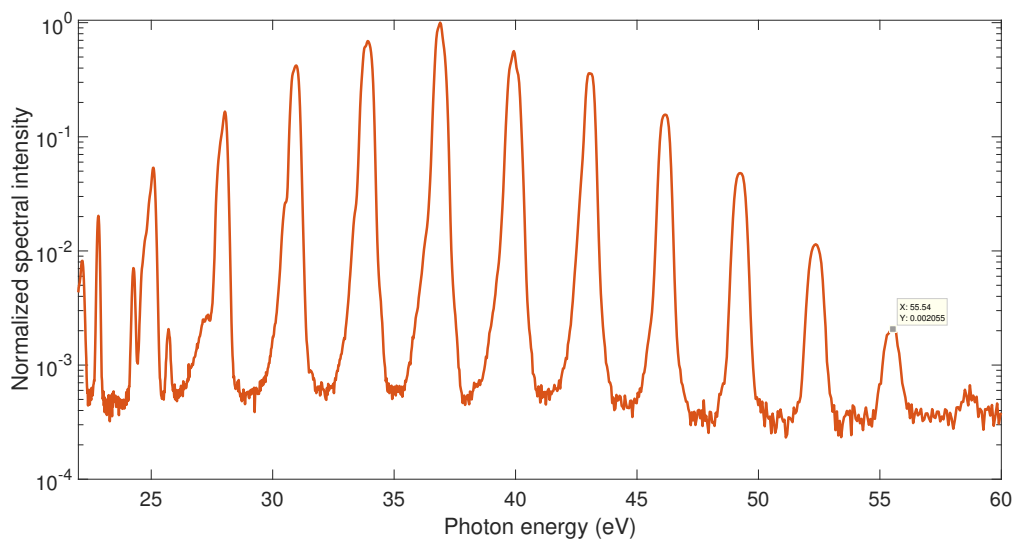


**Fig. 3.19** HHG spectrum obtained with argon. The HHG spectrum is generated with 35-fs laser pulses with 1 mJ of pulse energy. The HHG gas target is backed with 280 mbar of argon gas. The focal length of the focusing optics is 500 mm. Two 300 nm-thick aluminum filters are used to block the IR driving pulses.

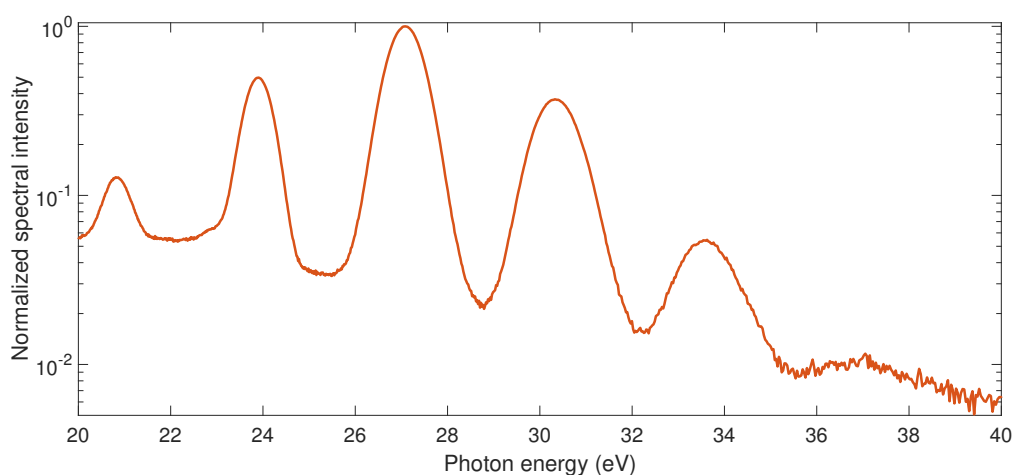


**Fig. 3.20** HHG spectrum obtained with krypton. The HHG spectrum is generated with 9-fs pulses from the HCF compressor with 0.2 mJ of pulse energy. The HHG gas target is backed with 40 mbar of krypton gas. The focal length of the focusing optics is 500 mm. The XUV beam is filtered with two 300-nm thick aluminum thin foils.

HHG spectra obtained from different noble gases, i.e., neon, argon and krypton. Krypton gas has the lowest ionization potential among the three. The HHG generated has the lowest photon energy. In the opposite case, neon has the largest ionization potential among the three and the HHG from neon has the highest photon energy. There is another interesting aspect to see from Fig. 3.18, Fig. 3.19 and Fig. 3.20. The widths of the HHG spectral peaks become broader as the driving laser duration reduces. When the laser pulse duration is short enough, the HHG spectral peaks are then broad enough to overlap with each other and form a XUV continuum which corresponds to isolated attosecond pulses .

High-energy XUV photons can be generated via HHG with noble gas with large ionization potential. In Fig. 3.21, a HHG spectrum covering up to 180 eV is shown. The HHG spectrum is generated with 35-fs laser pulses with 1 mJ of pulse energy. The HHG gas target is backed with 200 mbar of neon gas. The focal length of the focusing optics is 500 mm. One 300-nm thick zirconium filter is used to block the IR driving pulses.

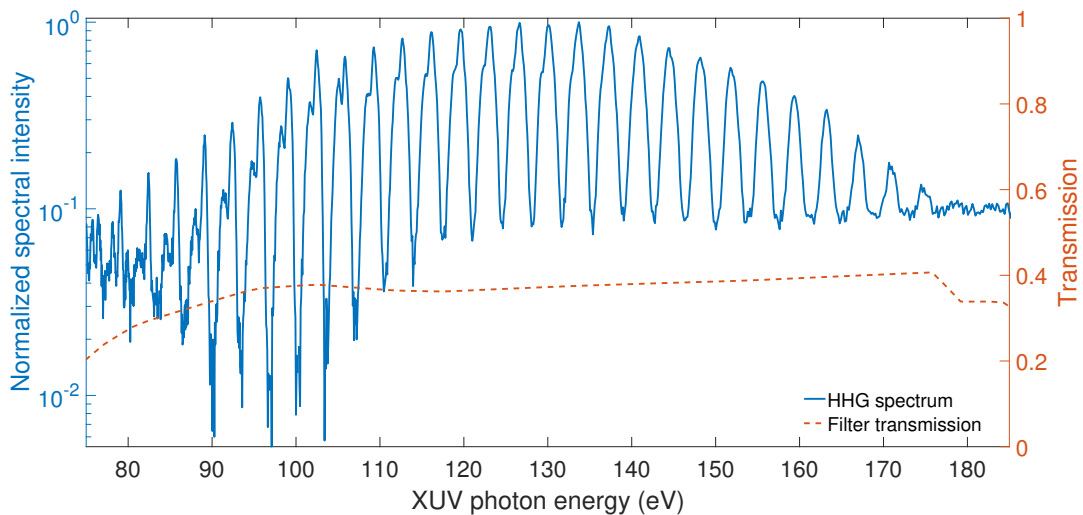


**Fig. 3.21** HHG spectrum covers up to 180 eV obtained with neon gas. The HHG spectrum (blue) is generated with 35-fs laser pulses with 1 mJ of pulse energy. The HHG gas target is backed with 200 mbar of neon gas. The focal length of the focusing optics is 500 mm. One 300 nm-thick zirconium filter is used to block the IR driving pulses. The transmission curve is also shown (red).

## 3.2 Narrow-bandwidth multilayer mirror monochromator for XUV pulses

Coherent XUV radiation is generated by the HHG process. The XUV radiation forms a pulse train of attosecond XUV pulses (APT) and may span over a very large spectral bandwidth. When

the length of the pulse train is reduced to a single pulse, the isolated attosecond XUV pulses provide unprecedented attosecond time resolution. On the other hand, monochromatic XUV sources with tunability are preferred in a large number of experiments, such as time-resolved and angle-resolved photoelectron spectroscopy [31], that is required to observe ultrafast dynamics occurring on a tens to hundreds of femtoseconds time scale. Extreme temporal resolution is not required in these experiments, whereas the spectral resolution is as important as the temporal resolution. To obtain monochromatic XUV radiation from HHG, various techniques have been proposed. For instance, a time-delay compensated monochromator (TDCM) [75], consisting of a pair of gratings that compensate for the tilt of the pulse-front, can select a single harmonic order within a wide spectral range. However, the throughput of the TDCM is low (typically on the order of a few percent) and it requires temporal characterization of the extracted XUV radiation. Another method for XUV radiation monochromatization is by means of multilayer mirrors. For instance, a monochromator equipped with one multilayer mirror covering the range from 27 eV to 130 eV was previously designed [76]. The entire bandwidth is covered with multilayer XUV mirrors with different coatings. This multilayer-mirror-based monochromator has a large tunable bandwidth. However, the reflection bandwidth is too broad to provide adequate spectral resolution, e.g., for time-resolved photoelectron spectroscopic studies of ultrafast surface chemistry. Another multilayer-mirror-based monochromator, which possesses much narrower reflection bandwidth but smaller tunable bandwidth, has been designed by Prof. Thorsten Uphues' group. They designed the multilayer mirror coating and have performed a full simulation on the characteristics of the multilayer mirrors. The author of the present thesis has been working together with Tanja Neumann from the Uphues group to carry out the experimental characterization of the newly designed and built-up multilayer mirror monochromator.

### 3.2.1 Design of a narrow-bandwidth multilayer mirror monochromator

The multilayer coating of a multilayer mirror consists of several layer pairs and each layer pair consists of a high refractive index layer and a low refractive index layer. The reflectivity of the entire stack is determined by the interference between the reflections from the interfaces of the coating layers. When the multiple reflections interfere constructively, the reflectivity reaches the maximum value. Meanwhile, the wavelength which interferes constructively changes as the incidence angle on the multilayer mirror changes. As a result, the reflectivity peak of a multilayer mirror can be controlled by tuning the incidence angle. The coefficient of reflection  $r$  and transmission  $t$  from the interface between two layers are given by the Fresnel equations. When the incidence angle is  $\theta_i$  and the refractive angle is  $\theta_t$ ,  $r$  and  $t$  for the  $s$ -polarized beam

are

$$r_s = -\frac{\sin(\theta_i - \theta_t)}{\sin(\theta_i + \theta_t)} \quad (3.67)$$

$$t_s = \frac{2 \sin \theta_t \cos \theta_i}{\sin(\theta_i + \theta_t)} \quad (3.68)$$

while for the  $p$ -polarized beam,  $r$  and  $t$  are

$$r_p = \frac{\tan(\theta_i - \theta_t)}{\tan(\theta_i + \theta_t)} \quad (3.69)$$

$$t_p = \frac{2 \sin \theta_t \cos \theta_i}{\sin(\theta_i + \theta_t) \cos(\theta_i - \theta_t)} \quad (3.70)$$

In principle, the overall reflectivity of the multilayer coating can be calculated one surface after the other. However, in practice, the reflection of a symmetric multilayer coating is usually calculated with the matrix transfer method, in which the electromagnetic fields at the two sides of each layer is related by a characteristic matrix  $M$ . Assuming the characteristic matrix of the  $j$ th layer of the coating is  $M_j$ , the overall characteristic matrix of a multilayer coating with  $p$  layers is given by

$$M = M_1 \cdot M_2 \cdot M_3 \cdots M_p = \begin{bmatrix} m_{11} & m_{12} \\ m_{21} & m_{22} \end{bmatrix} \quad (3.71)$$

in which  $m_{ij}$  are the matrix elements. Once  $M$  of the entire system is obtained, the coefficient of amplitude reflection  $r$  for a  $s$ -polarized beam is given by [77]

$$r = \frac{p_0 m_{11} + p_0 p_s m_{12} - m_{21} - p_s m_{22}}{p_0 m_{11} + p_0 p_s m_{12} + m_{21} + p_s m_{22}} \quad (3.72)$$

in which

$$p_0 = \sqrt{\frac{\epsilon_0}{\mu_0}} n_0 \cos \theta_i \quad (3.73)$$

$$p_s = \sqrt{\frac{\epsilon_0}{\mu_0}} n_s \cos \theta_t \quad (3.74)$$

where  $n_0$  is the refractive index of the medium where the input field locates,  $n_s$  is the refractive index of the substrate,  $\theta_i$  is the incidence angle and  $\theta_t$  is the refraction angle of the outgoing beam.

In our case, a Mo/Si coating is used for the multilayer mirrors in the narrow-bandwidth monochromator. The multilayer stacks consists of  $N=75$  Mo/Si layer pairs. The peak reflectivity is at a photon energy of  $E=91.6$  eV by design, when the incident angle is  $15^\circ$ . The bandwidth of the reflection of a single multilayer mirror is  $\Delta E < 0.8$  eV, which leads to the reflectivity of the

monochromator is  $\sim 0.6$  eV. Meanwhile, by filtering from the HHG cut-off region, the reflection bandwidth supports a transform-limited pulse duration of  $\sim 3$  fs, which provides sufficient temporal resolution for femtosecond dynamic studies. The designed multilayer mirror provides XUV wavelength tunability from 90 eV to 100 eV which can be seen from the calculated reflectivity which is shown in Fig. 3.22.

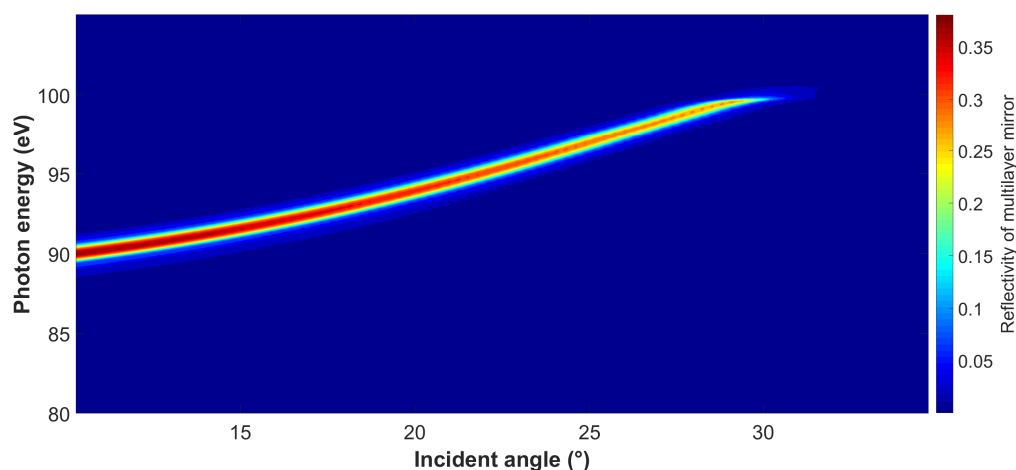


**Fig. 3.22** Reflectivity of one multilayer mirror. The wavelength with the peak reflectivity varies as the incident angle changes.

In order to maintain the beam propagation direction during tuning for subsequent spectroscopic experiments, two multilayer mirrors are used consecutively as shown in Fig. 3.23. In order to achieve adequate intensity required for experiments, the second XUV mirror in the monochromator is a spherical mirror, which is also used to focus the XUV beam. Besides the intensity, the focusing optics is used to correct the wavefront of the XUV beam and thus improve the temporal resolution of the experiments since the XUV beam generated by HHG is divergent. The two mirrors are both mounted on rotary stages and translation stages, which allow us to move both mirrors accordingly to change the output XUV wavelength while maintaining the beam propagation direction and maintaining the focal position. When the mirrors are rotated for tuning the reflected wavelength, the distance between the mirrors along the input beam direction has to change since the transverse distance between the mirrors is kept constant. Changing the distance between the mirrors actually can be accomplished with one translation stage. However, this is not sufficient to maintain the focal position for the subsequent spectroscopy experiments as the effective focal length of a spherical mirror changes with the incident angle. Hence, a second translation stage is added to move the second mirror

for maintaining the focal position. The monochromator, as shown in Fig. 3.24, is placed inside the TM vacuum chamber shown in Fig. 3.5.

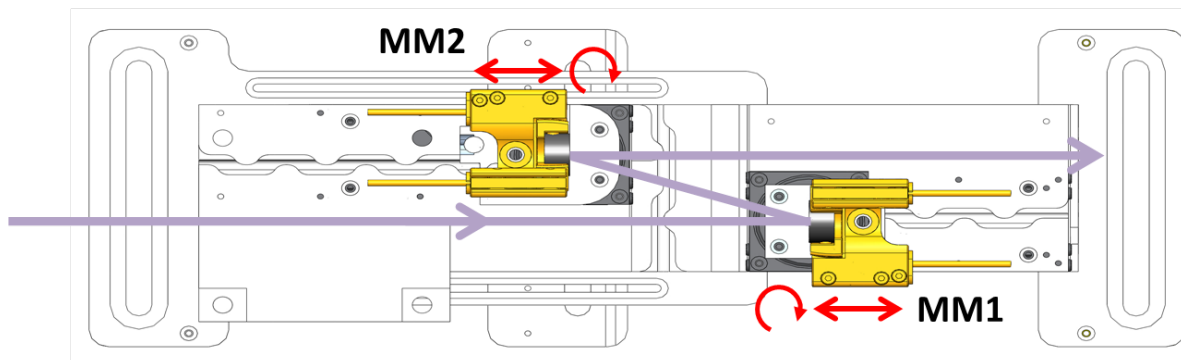


**Fig. 3.23** Schematic of the optical beam path in the XUV multilayer monochromator. The XUV beam enters from the left side and exits to the right side. Both of the multilayer mirrors can be rotated and translated. The first multilayer mirror *MM1* is a flat mirror while the second multilayer mirror *MM2* is a spherical mirror.

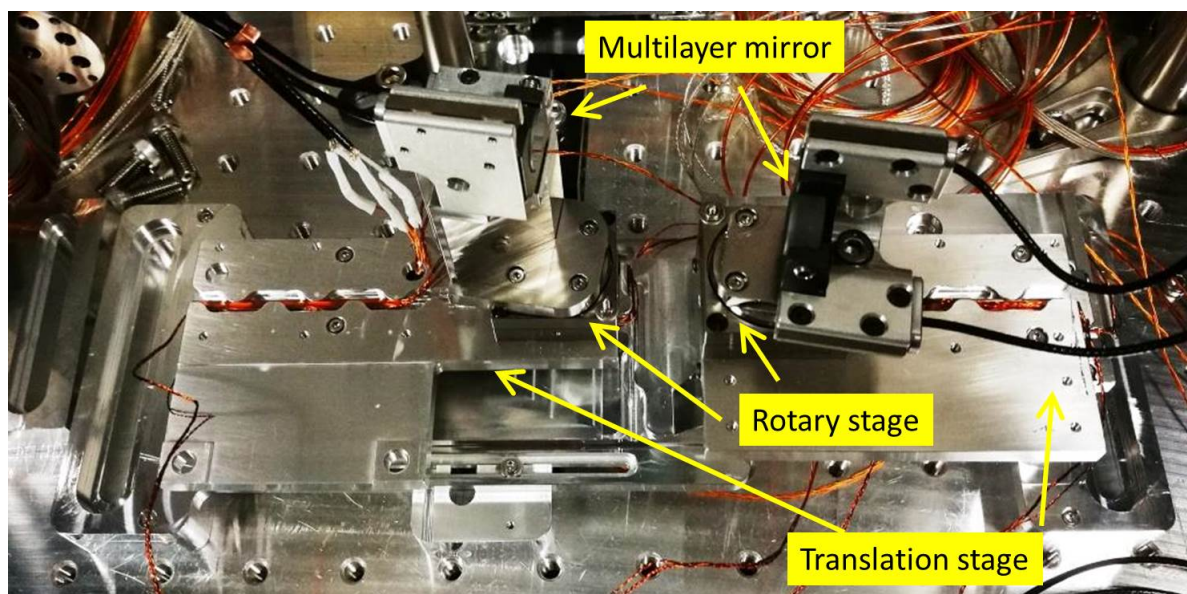


**Fig. 3.24** Photo of the multilayer mirror monochromator. The XUV beam enters from the left side and exits to the right side. The rotation stages required for XUV tuning and the translation stages can clearly be seen in the photo.

### 3.2.2 Experimental characterization of the multilayer mirror monochromator

The performance of the multilayer mirrors at  $15^\circ$  incidence angle was characterized by the Physikalisch-Technische Bundesanstalt (PTB). The experimental measured reflectivity of the monochromator and the calculated one are both shown in Fig. 3.25. The reflectivity obtained from simulation is centered at 91.6 eV and the bandwidth is 0.64 eV. Meanwhile, the experimentally measured reflectivity is centered at 91.8 eV and the bandwidth is 0.59 eV, which matches well with the desired bandwidth of  $<0.8$  eV. Meanwhile, there is a  $\sim 0.2$  eV difference of reflectivity peak between the simulated value and the experimentally measured one, which may originate from the manufacturing imperfection. In order to characterize the reflectivity of the monochromator over the entire tunability range, the XUV beam originating from the HHG experimental apparatus discussed in section 3.1.5 is used to further characterize the monochromator. The spectrum of the XUV beam which was used for characterization is shown in Fig. 3.18 in Section 3.1.5.

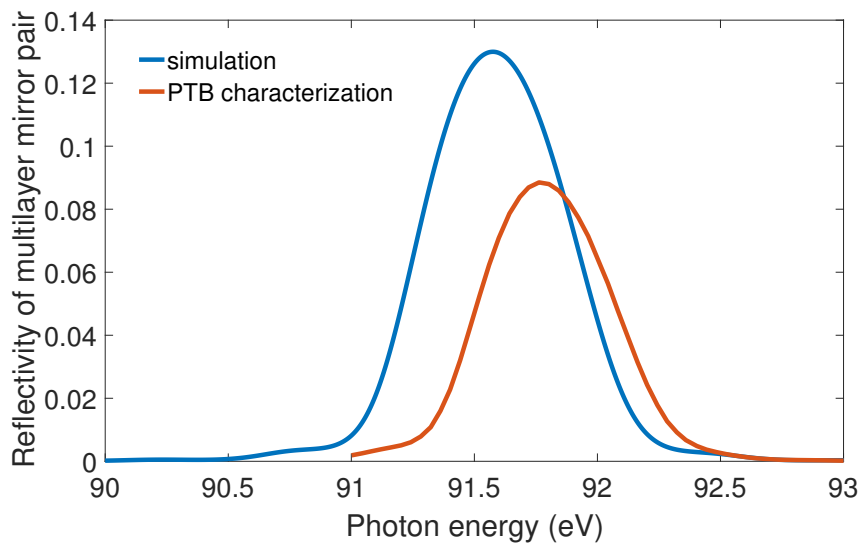


**Fig. 3.25** Reflectivity of the monochromator at  $15^\circ$  incidence angle. The experimental measured reflectivity (red) of the monochromator and the calculated one (blue) are both shown. The reflectivity obtained from simulation is centered at 91.6 eV and the bandwidth is 0.64 eV. Meanwhile, the experimentally measured reflectivity is centered at 91.8 eV and the bandwidth is 0.6 eV, which matches well with the designed bandwidth of  $<0.8$  eV. The experimental characterization of the reflectivity is carried out by PTB.

The XUV beam is sent through the monochromator and the monochromatized output is measured with the 251MX XUV spectrometer. The multilayer mirrors are tuned to select out the highest energy peak of the HHG spectrum, which is the harmonic order located at



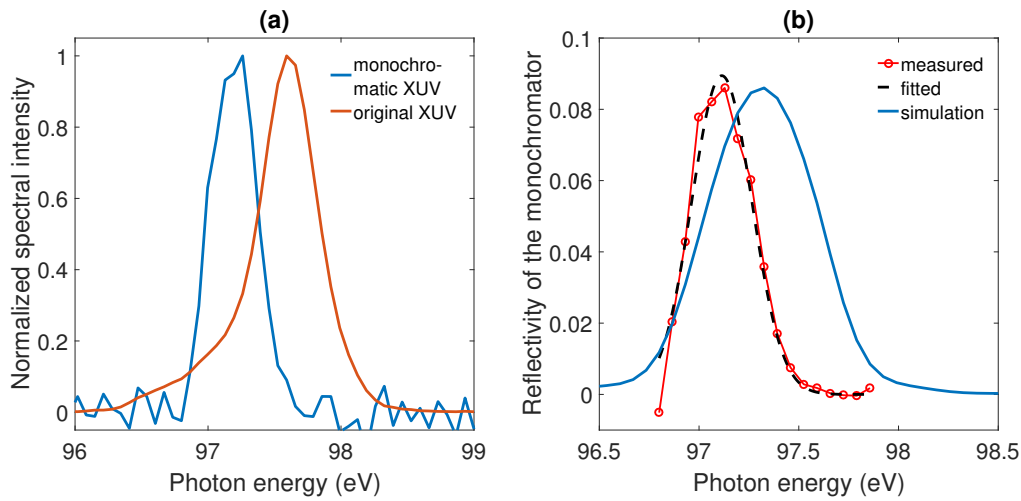


**Fig. 3.26** Monochromatic XUV spectrum and the monochromator reflectivity. (a) the original XUV spectrum is shown as red curve, which is one harmonic order in Fig. 3.18. The blue curve is the spectrum after the monochromatic XUV beam from the monochromator with incidence angle at  $25.5^\circ$ . The bandwidth of the monochromatic XUV spectrum is  $\sim 0.4$  eV. (b) the monochromator reflectivity obtained by comparing the two spectra in (a) is shown as red circled curve. The Gaussian fit of the reflectivity is shown as black dashed line. The reflectivity centered at 97.1 eV and the bandwidth is 0.9 eV. For comparison, the simulated reflectivity of the monochromator at  $25.5^\circ$  incidence angle is shown as blue curve. The measured reflectivity is scaled to the simulated one.

97.6 eV. The incident angle on the multilayer mirrors was  $25.5^\circ$ . In Fig. 3.26(a), the original XUV spectrum is shown as red curve, which is one harmonic order, while the blue curve is the spectrum of the monochromatic XUV beam from the monochromator which is centered at 97.2 eV with a FWHM bandwidth of  $\sim 0.4$  eV which is narrower desired value ( $< 0.6$  eV) thanks to the fact that the reflectivity curve filter out the rising edge of the HHG peak. In general, the zirconium filter transmission, the grating diffraction efficiency and the CCD detection quantum efficiency are all frequency dependent. However, the spectra in Fig. 3.26(a) only cover such narrow spectral bandwidth within which the three factors are assumed to be independent on the frequency. As a result, the monochromator reflectivity, which is the only frequency dependent factor, can be calculated by comparing the original XUV spectrum and the monochromatic XUV spectrum. In Fig. 3.26(b), the measured monochromator reflectivity is shown as red line with circles. Meanwhile, the black dashed line is the Gaussian fit of the reflectivity, which gives the reflectivity peak position and the FWHM bandwidth which are 97.1 eV and 0.36 eV (adjusted  $R^2$  is 0.969), respectively. For comparison, the simulated reflectivity of the monochromator at  $25.5^\circ$  incidence angle is also shown in Fig. 3.26(b). The simulated reflectivity is centered at 97.3 eV with the FWHM bandwidth of 0.89 eV. As in the case of  $15^\circ$  incidence angle, there is a 0.2 eV discrepancy between the measured and the simulated value, which may originated from manufacturing imperfection. The experimental result indicates that



the simulated reflectivity matches well with the measured one except for the discrepancy due to manufacturing imperfection which is even present in the PTB characterization.

At this point, the reflectivity profile at one incident angle, which matches very well with the designed reflectivity, is measured and narrow-bandwidth ( $\sim 0.4$  eV) XUV radiation is obtained with the monochromator. To complete the full characterization of the monochromator, further measurements on the reflectivity at different incidence angles as well as measurements on the XUV flux throughput are scheduled and currently ongoing.

### 3.3 Isolated attosecond pulse generation

Isolated attosecond pulses are events with ultrashort temporal durations which correspond to ultrabroad spectral bandwidth. It is rather difficult to achieve such a broad bandwidth in the visible to infrared range. Although sub-femtosecond pulse generation in the visible wavelength range has been demonstrated [78], it takes great efforts for such kinds of experiments. For pulses with the same pulse duration  $\Delta t$ , the required absolute spectral bandwidth  $\Delta \nu$  is identical regardless of the central frequency  $\nu_0$ . However, the relative bandwidth  $\Delta \nu / \nu_0$  decreases as the center frequency of the pulses increases. In general, the field generated via HHG is in the XUV range, in which the frequency is much higher than that of laser outputs. Currently, HHG is the only known process that can generate isolated attosecond pulses. As discussed in previous sections, the recombination step in the HHG process happens within less than half a laser cycle and therefore is indeed a phenomenon occurring on an attosecond time scale. We also know that HHG with a long laser pulse actually produces a train of attosecond pulses separated by half a laser cycle. The main challenge of isolated attosecond pulse generation is to single out one individual pulse from the attosecond pulse train.

Various gating methods have been proposed and demonstrated to achieve isolated attosecond pulses. Amplitude gating exploits the fact that the cutoff region of typical HHG spectra obtained from few-cycle pulses is a continuum, which corresponds to a single XUV burst in the time domain [79–81]. Amplitude gating methods require laser pulses shorter than two cycles and most of the XUV photons, those locating in the HHG plateau, are abandoned. In two-color gating [82–84], a second harmonic field is added to the driving laser field. The second harmonic field breaks the symmetry of the fundamental driving laser field, which increases the separation between pulses in the attosecond pulse train to a whole laser cycle. This loosens the challenging requirement of pulse duration to a single-cycle. The attosecond lighthouse method [85–87] on contrary separates the attosecond pulses spatially. The laser pulse phase front was prepared using a glass wedge in such a way that it rotates continuously during the pulse duration. Different attosecond pulses generated in different cycles within a laser pulse propagate into

different direction. A hard aperture placed in the far field is used to select only one attosecond pulse. Polarization gating (PG) makes use of the strong HHG yield dependence on the driving laser polarization [88–90]. The HHG yield decreases rapidly as the driving laser field deviates from linear polarization. A pulse with time-varying ellipticity allows to control the HHG yield within the laser pulse. Another set of methods dubbed (generalized) double optical gating [(G)DOG] combines the ideas of two-color polarization gating and polarization gating [91–93]. The polarization gating and double optical gating will be discussed in greater detail in the next section since they are employed in our experiment where we initially used rather long  $>6$  fs driver pulses.

### 3.3.1 Polarization gating and double optical gating

As mentioned already, the HHG process is extremely sensitive to the polarization state of the driving laser. As the ellipticity increases, the HHG yield decreases drastically. There is a difference between the exact dependence curve for the high-order harmonics and the threshold harmonics [94, 95]. Threshold harmonics refer to the harmonic orders with energy close to the ionization potential of the generation gas. The high-order harmonic yield peaks at linear polarization while the low-order harmonics exhibit a double-hump shape around linear polarization. Here, only the case for the high-order harmonics is discussed. The HHG yield can drop by one order of magnitude, when the ellipticity increases from 0 to 0.2 [96]. This can be understood qualitatively with the semiclassical picture. In a driving field, which is not linearly polarized, there is a transverse component of the laser field to push the freed electron sideways. As a result, the electron will eventually miss the parent ion, and the HHG yield is suppressed due to the reduced recombination amplitude.

If one can prepare a driving laser pulse, in which the leading and trailing portion is circularly polarized and only the center portion is linearly polarized, the temporal window for generation of XUV radiation is then shorter than the laser pulse. With short enough time window, isolated attosecond pulses can be generated. Such a method for achieving isolated attosecond pulse generation is called polarization gating.

A pulse with time-varying polarization state can be formed experimentally, e.g., by combining two circularly polarized pulses with opposite helicity. The two pulses propagating in the  $z$  direction, which are left- and right-circularly polarized, are given by

$$\vec{E}_l(t) = E_0 e^{-2\ln(2)\left(\frac{t-T_d/2}{\tau_p}\right)^2} [\hat{i}\cos(\omega_0 t + \varphi_{CE}) + \hat{j}\sin(\omega_0 t + \varphi_{CE})](-1)^n \quad (3.75)$$

$$\vec{E}_r(t) = E_0 e^{-2\ln(2)\left(\frac{t+T_d/2}{\tau_p}\right)^2} [\hat{i}\cos(\omega_0 t + \varphi_{CE}) - \hat{j}\sin(\omega_0 t + \varphi_{CE})](-1)^n \quad (3.76)$$

where  $T_d$  is the delay between the two pulses,  $\tau_p$  is the duration of the pulses. It is instructive to decompose the pulses into two orthogonally and linearly polarized components as in Fig. 3.27. One component is responsible for actually generating the XUV pulses while the other component gates the HHG process. The former is called the driving field, while the latter is termed gating field.

$$E_d(t) = E_0 \left[ e^{-2\ln(2)\left(\frac{t+T_d/2}{\tau_p}\right)^2} + e^{-2\ln(2)\left(\frac{t-T_d/2}{\tau_p}\right)^2} \right] \cos(\omega_0 t + \varphi_{CE}) \quad (3.77)$$

$$E_g(t) = E_0 \left[ e^{-2\ln(2)\left(\frac{t+T_d/2}{\tau_p}\right)^2} - e^{-2\ln(2)\left(\frac{t-T_d/2}{\tau_p}\right)^2} \right] \sin(\omega_0 t + \varphi_{CE}) \quad (3.78)$$

The time-varying ellipticity  $\xi$  is

$$\xi = \frac{\left| e^{-2\ln(2)\left(\frac{t+T_d/2}{\tau_p}\right)^2} - e^{-2\ln(2)\left(\frac{t-T_d/2}{\tau_p}\right)^2} \right|}{e^{-2\ln(2)\left(\frac{t+T_d/2}{\tau_p}\right)^2} + e^{-2\ln(2)\left(\frac{t-T_d/2}{\tau_p}\right)^2}} = \frac{\left| 1 - e^{-4\ln(2)\left(\frac{T_d}{\tau_p}\right)t} \right|}{1 + e^{-4\ln(2)\left(\frac{T_d}{\tau_p}\right)t}} \quad (3.79)$$

We assume now that the HHG process is only possible inside the polarization gate, where the ellipticity  $\xi \leq \xi_{th}$ .  $\xi_{th}$  is the threshold ellipticity. Then the temporal width of the polarization gate is

$$\delta t_G = \frac{\xi_{th}}{\ln(2)} \frac{\tau_p^2}{T_d} \quad (3.80)$$

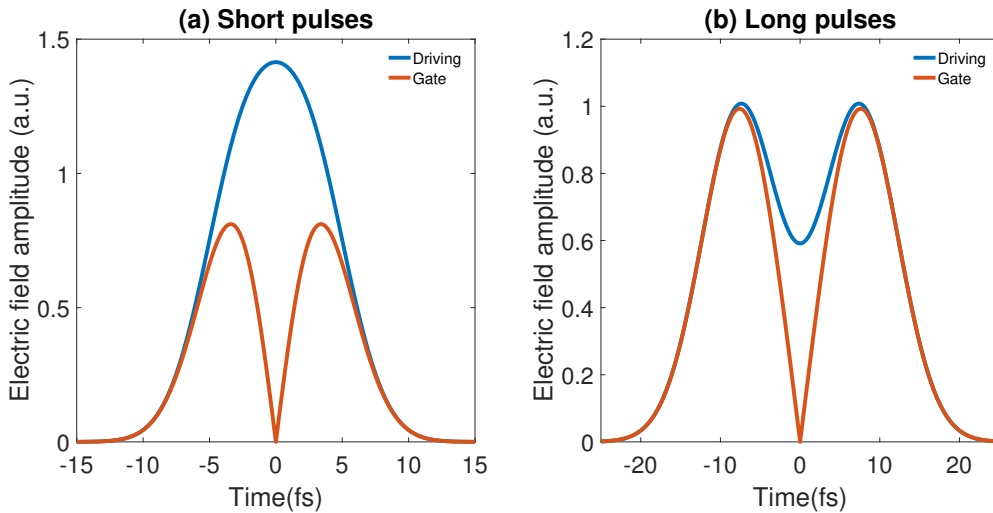


**Fig. 3.27** Driving electric field in polarization gating. The electric field is decomposed into a driving field (blue trace) and a gating field (red). The polarization gate width is identical while the pulse durations are different in the two figures. (a) The pulse duration is 8 fs and the delay is 8 fs, (b) the pulse duration is 10 fs and the delay is 18 fs.

For Ti:sapphire pulses, the laser cycle is  $T_0 = 2.7$  fs, as a result the polarization gate should not be longer than  $T_0/2 = 1.35$  fs. Either using pulses with shorter duration or increasing the delay between the two pulses can reduce the gate width to the desired value. Usually, the shortest pulse duration available is determined by the laser system, which is not easy to change. Varying the delay between two pulses is a much more straightforward approach. Meanwhile, the amplitude of the driving laser field inside the polarization gate is

$$E_{d,max} = 2E_0 e^{-\frac{\ln(2)}{2} \left(\frac{T_d}{\tau_p}\right)^2} \quad (3.81)$$

When  $T_d \gg \tau_p$ , the laser field inside the gate is much weaker than the field outside, compare Fig. 3.27, which means a lot of pulse energy is wasted and not used for HHG. More problematic, the much stronger field outside of the polarization gate can fully ionize the gas medium, which makes HHG from the field inside the gate impossible due to ground-state depletion or phase-matching problems. This means there is an upper limit for the pulse duration when applying polarization gating, e.g., when argon gas is used as HHG medium, the pulse duration should not be longer than 7 fs [40].

Double optical gating is completed by adding a second harmonic field to the polarization gating scheme. The two-color gating alone extends the separation between the attosecond bursts in the pulse train to one optical cycle instead of two. The width of the polarization gate of a full laser cycle  $T_0 = 2.7$  fs is then enough to gate out a single attosecond pulse. It means that longer laser pulses can be used to generate isolated attosecond pulses compared to pure polarization gating. Meanwhile, it also means that with pulses of the same duration, a shorter delay can be used and effectively more of the laser pulse energy is used for XUV generation.

### 3.3.2 Experimental apparatus and methods for isolated attosecond pulse generation

The experimental setup for generating the polarization gating field consists of a quartz plate and a quarter waveplate. The quartz plate serves twofold purposes. Due to the birefringence of quartz, the input pulse is split into two pulses, i.e., the ordinary wave and the extraordinary wave. When the angle between the polarization plane of the input laser and the optical axis of the quartz plate is  $45^\circ$ , the input is split into two pulses with identical amplitude while being polarized perpendicular to each other. Meanwhile, the two pulses are delayed since the refractive index is different for ordinary wave and extraordinary wave. A quartz plate of 0.1-mm thickness introduces 3 fs of delay to the two pulses provided the pulse is centered at 800 nm. Varying the effective thickness of the quartz plate via rotating the plate, the delay

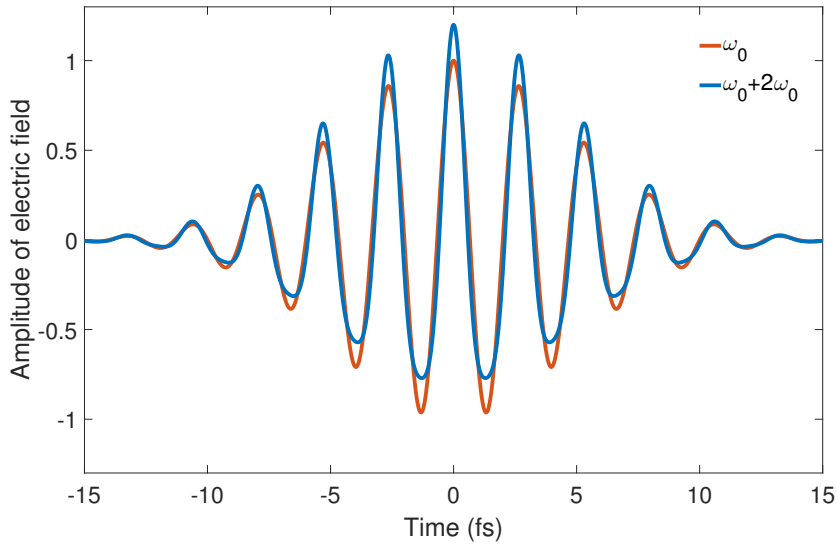
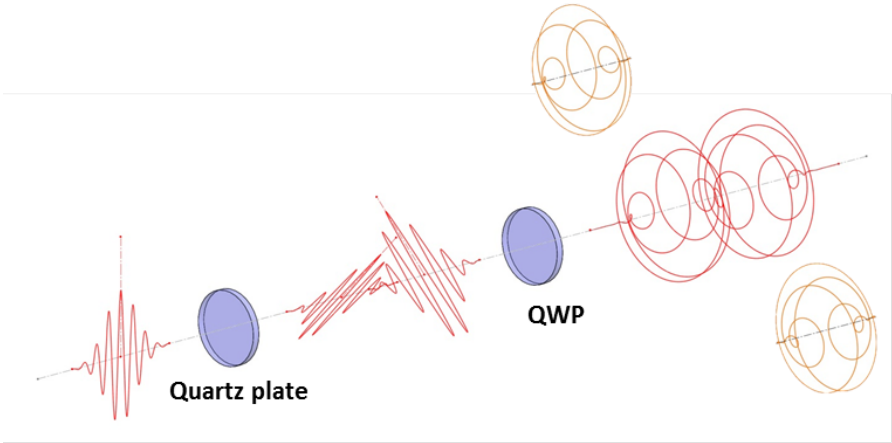


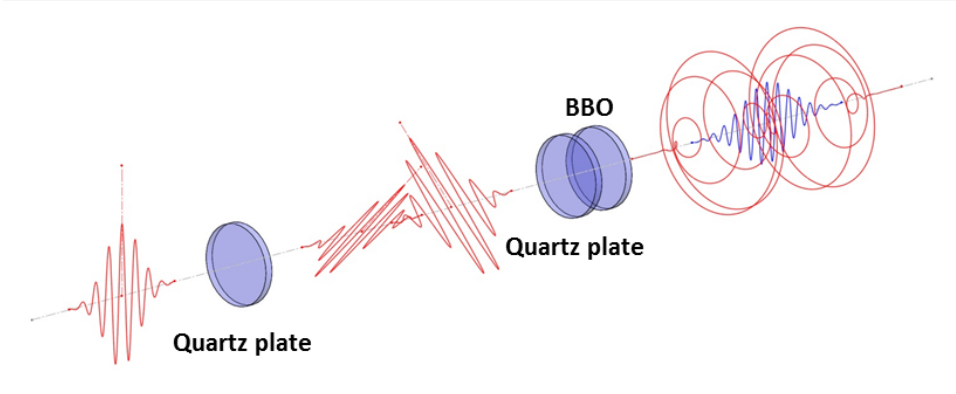
**Fig. 3.28** Two-color electric field. The fundamental field (red) and the two-color field (blue) are shown. The amplitude of the second harmonic field is 10% of the fundamental field. The second harmonic field breaks the symmetry of the electric field.

between the pulses can be adjusted. Quartz has a small refractive index difference between the ordinary wave and the extraordinary wave, which allows fine delay control. The two pulses are then sent through an achromatic quarter waveplate. The quarter waveplate is placed in such a way that the optical axis of the waveplate is parallel to the input pulse's polarization plane before the first quartz plate. The quarter waveplate converts the two pulses into circularly polarized ones. The two pulses then have left and right circular polarization.

The setup for double optical gating (DOG) is very similar to the setup above. A quartz plate is used to split and delay the pulses as in polarization gating. However, the quarter waveplate is replaced by another quartz plate and a piece of BBO for second harmonic generation. The second quartz plate and the BBO together form an effective quarter waveplate. The 5.3 fs pulses provided by the hollow core fiber compressor mentioned in chapter 2 were not yet available at the time when this experiment was performed. The pulses used with double optical gating to generate isolated attosecond pulses had 9-fs duration due to limited bandwidth of the chirped mirror compressor used previously. The delay between the pulses can be obtained via Eq. (3.80). The polarization gate width is about one laser cycle which leads to the delay of about 8.6 fs which sets the lower limit of the delay. As a result, a 0.3-mm thick quartz plate is used to split and delay the pulses. The delay introduced by the quartz plate is 9 fs. A 0.1-mm thick BBO is used for generating the second harmonic field. The BBO is oriented to maximize the second harmonic field along the polarization plane of the input pulses. The pulse energy of the second harmonic field is a few percent of the fundamental field. The thickness of the



(a) Polarization gating



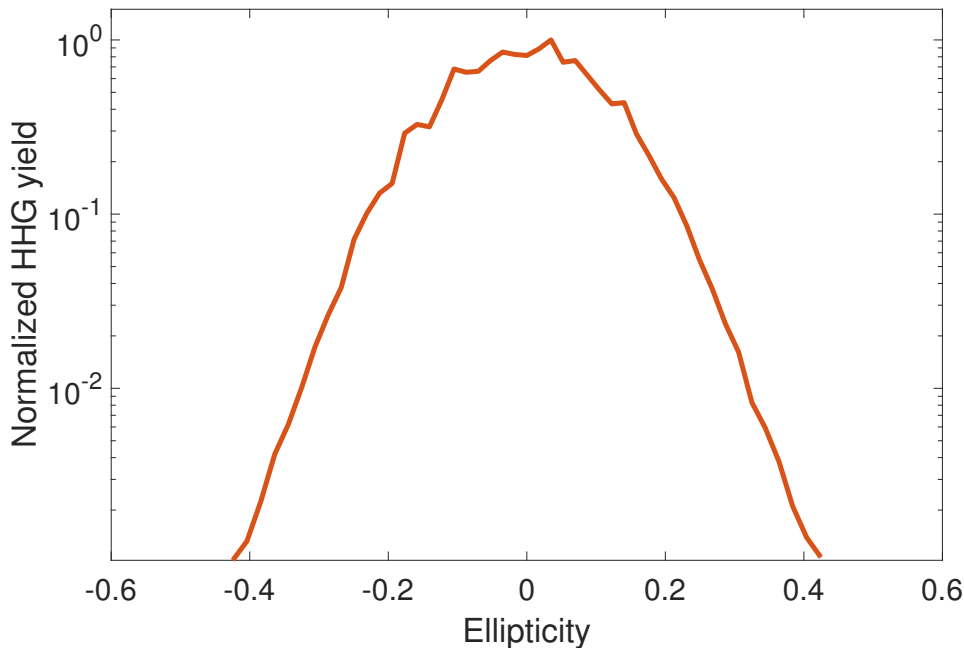
(b) Double optical gating

Fig. 3.29 Schematic of polarization gating and double optical gating.

second quartz plate is then chosen accordingly to form a quarter waveplate in combination with the BBO. Since the experimental apparatus is in the process of being built up and therefore the parameters are being explored, flexibility is one of the main concerns in designing the experimental setup. As a result, the quartz plates prepared for the experiment have thicknesses in increments of 0.1 mm. Then the quartz plate is rotated to obtain the desired thickness in between the discrete steps.

Due to the broad bandwidth of the few-cycle pulses, silver mirrors are used in the experiment. However, the drawback of metallic mirrors is that the s-polarized component and the p-polarized component have a relative phase shift after reflection. A circularly polarized beam after reflection is then no longer circularly polarized. As a result, in the experiments, the silver mirrors are used close to normal incidence to minimize the distortion of the polarization state of the laser pulses.

### 3.3.3 Experimental results of isolated attosecond pulses generation



**Fig. 3.30** Dependence of HHG yield on the ellipticity of the laser pulses. The XUV beam is generated by focusing 0.25 mJ of 9-fs laser pulses into the HHG gas target which is backed with 150 mbar of argon gas. Two 300-nm thick aluminum filters are used to filter the XUV beam. The HHG signal is detected by placing the CCD at the zeroth diffraction order position, which means that the HHG signal yield including signal from all the harmonic orders.

The realization of the polarization gating and the double optical gating depends on the fact that HHG yield is extremely sensitive to the polarization state of the driving laser pulses. When the ellipticity of the driving laser pulses increases, the HHG yield decreases drastically. The dependence of the HHG yield on the ellipticity is examined experimentally. The measured result is shown in Fig. 3.30. The XUV beam is generated with 0.25 mJ of 9-fs laser pulses. The gas target is backed with 150 mbar of argon gas. Two 300-nm thick aluminum filters are used to filter the XUV beam. The HHG signal is detected by placing the CCD at the zeroth diffraction order position, which states that the HHG signal yield shown in Fig. 3.30 including signal from all the harmonic orders. An achromatic QWP is rotated to control the ellipticity of the laser pulses. The experimentally measured result is consistent with results shown in the literature. When the ellipticity increases from 0 to 0.2, the HHG yield reduces by one order of magnitude.

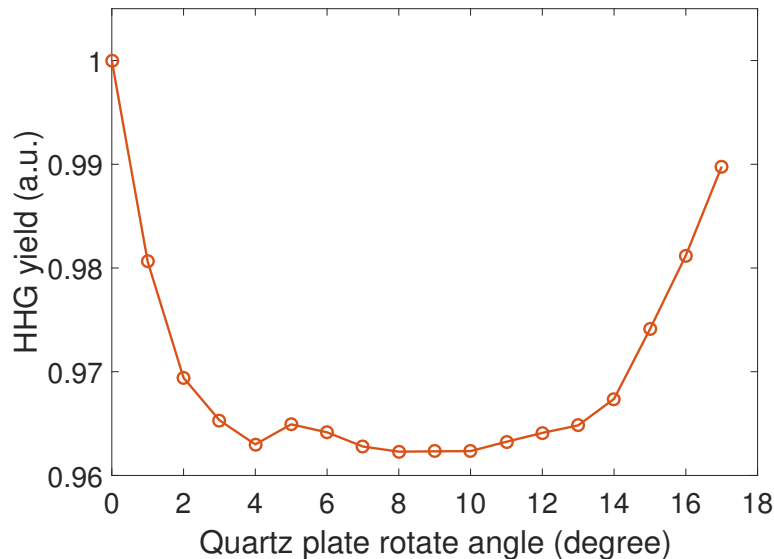


**Fig. 3.31** Dependence of HHG yield on rotation angle of the quartz plate. As the quartz plate rotates, the polarization state of the output pulses changes which leads to the changes of the HHG yield.

As mentioned above, the duration of the laser pulses used in polarization gating should not be longer than 7 fs. Since the 5.3-fs pulses from the HCF compressor are not yet available, the double optical gating (DOG) method is adopted in our isolated attosecond pulse generation experiments. In our experimental setup, the thicknesses of the two quartz plates and the BBO are 0.4 mm, 0.3 mm and 0.1 mm, respectively. The first quartz plate splits the initial laser pulse into two pulses. The second quartz plates and the BBO together forms an effective quarter waveplate. The second quartz plate is rotated to obtain the desired effective thickness which matches the thickness of the BBO to form the effective QWP. By rotating the quartz plate and thus changing the effective thickness, the polarization state of the pulses after the BBO



also varies. When the first quartz plate is missing and thus only one pulse passes through the effective QWP, the resultant HHG yield varies as the second quartz plate rotates which is shown in Fig. 3.31. When the appropriate effective thickness is achieved and an effective QWP is formed, the HHG yield reaches its minimum as the laser pulse becomes circularly polarized.

When the first quartz plate is added to the setup, the temporal gate, in which the HHG is allowed, decreases as the effective QWP is being approached. The width of the generated HHG peaks increases as this temporal gate decreases. The increase in width of the HHG spectral peaks is also observed experimentally as shown in Fig. 3.32. In Fig. 3.32, as the XUV emission gate decreases, the spectrum changes from the red curve to the blue curve. The shift of the HHG peaks is due to the slight shift of central wavelength of the driving laser.

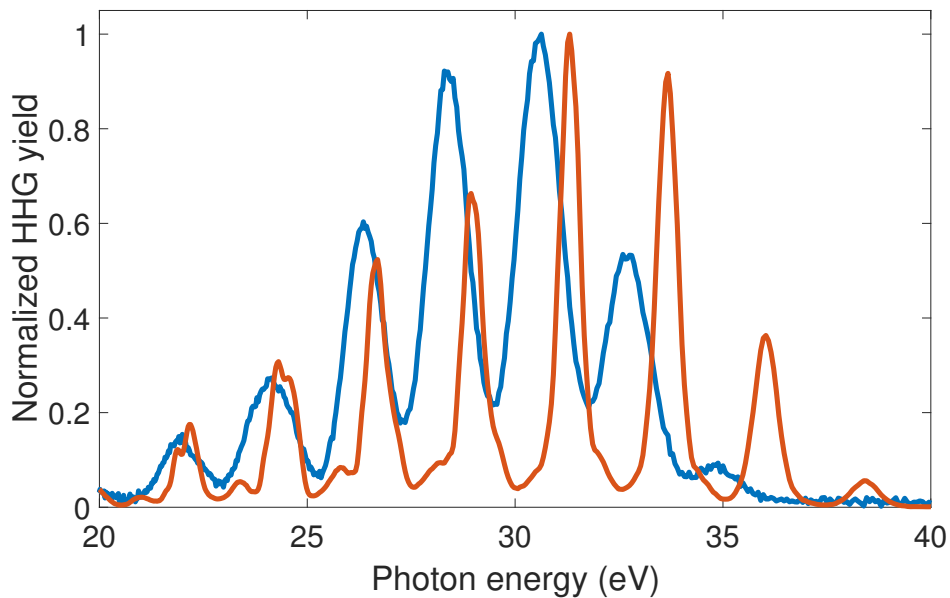


**Fig. 3.32** Width of HHG spectral peaks dependence on the double optical gating field. As the quartz plate rotates, the polarization state of the output pulses changes. This leads the changes on the temporal gate in which HHG is allowed. As the temporal gate decreases, the width of HHG spectral peaks increases, i.e., the spectrum changes from the red one to the blue one.

Eventually, when all the optics are well adjusted, the temporal gate is so narrow that only one attosecond pulse is generated. An isolated attosecond pulses (IAP) corresponds to an XUV continuum spectrum. The continuum obtained in our experiments is shown in Fig 3.33. The input pulse energy is 0.37 mJ and the pulses are focused with a  $f = 500$  mm spherical silver mirror. The gas target is backed with 100 mbar of argon gas. Two 300 nm aluminum filters are used to block the driving IR field.

The typical HHG peak structure indicates that the HHG process happens multiple times during the entire laser pulse. Meanwhile, the XUV continuum is a strong indication of having

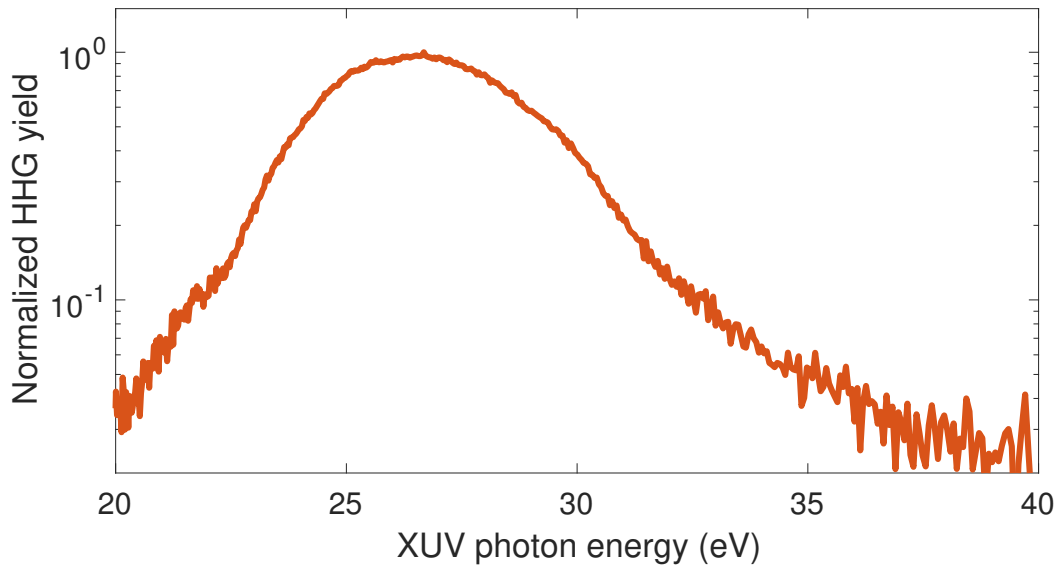


**Fig. 3.33** XUV continuum obtained with double optical gating. The transform-limited pulse duration of the XUV continuum is shorter than 300 as.

generated isolated attosecond pulses. The XUV continuum shown in Fig 3.33 corresponds to a transform-limited pulse duration less than 300 as.

As mentioned before, CEP stability and control is crucial for isolated attosecond pulse generation. When the CEP of the CPA pulses is stabilized, a thin wedge pair is inserted into the beam to control the CEP at the XUV generation site, i.e., the HHG gas target. The XUV continuum can only be generated at certain CEP values at which only one single XUV burst is allowed inside the polarization gate. By continuously inserting the wedges, the CEP of the laser pulses changes accordingly. In Fig. 3.34, it shows the XUV spectrum varies as the CEP is scanned. The CEP value deviation between two neighboring plots is  $\sim 0.7\pi$ . The XUV continuum repeats itself when the CEP is changed by  $2\pi$ . The key significance of a stable and controlled CEP on the XUV spectral shape is another good indication that isolated attosecond pulses are generated. However, the final confirmation of the generation of isolated attosecond pulses is obtained only by characterizing the pulses with the attosecond pulse characterization methods introduced in the next chapter.

### 3.4 Summary

In this chapter, the efforts to generate isolated attosecond XUV pulses and monochromatized XUV radiation for time-resolved photoelectron spectroscopy are described. The HHG experimental apparatus, including the vibration isolated vacuum system and the XUV spectrometer

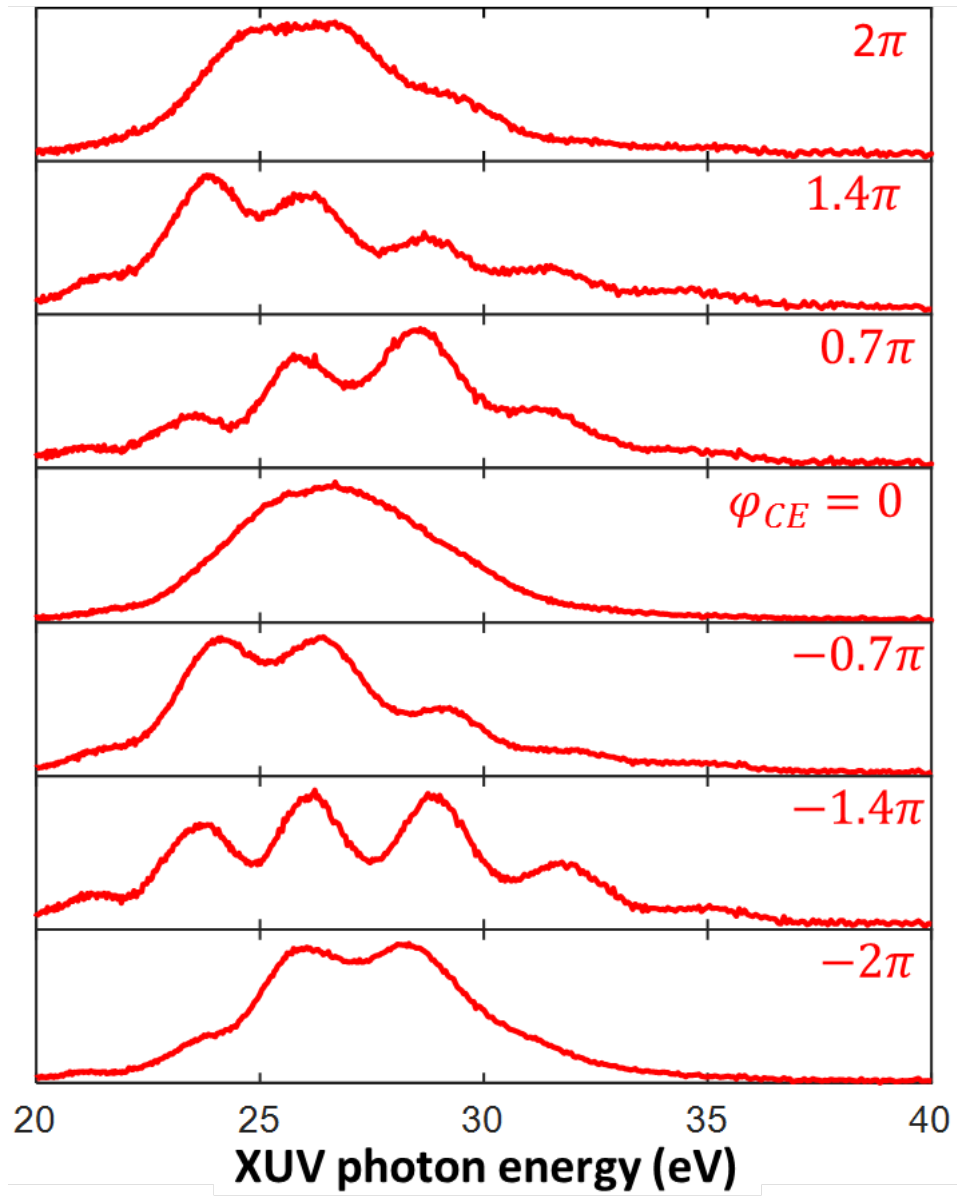


**Fig. 3.34** Variation in the XUV spectrum as the CEP of the laser pulses changes. The XUV spectrum varies as the CEP of the laser pulses changes. The CEP is varied by changing the thickness of a wedge.

are discussed in details. The HHG experiments with the laser pulses from the CPA system and the few-cycle pulses from the HCF compressor have been carried out. XUV radiation has been generated from various noble gases, including krypton, argon and neon. Especially XUV photons up to 180 eV have been generated from neon. In the meantime, a narrow-bandwidth multilayer-mirror-based monochromator for XUV pulses has been characterized, which has shown the simulated reflectivity and the measured one matches well. Monochromatized XUV radiation centered at 97.2 eV with 0.4 eV FWHM bandwidth has been obtained experimentally. Meanwhile, with the help of double optical gating, an XUV continuum has been obtained. The XUV continuum supports a transform-limited pulse shorter than 300 as. Strong dependence of the XUV continuum on the driving pulses CEP is also observed. The CEP dependence of the XUV continuum strongly indicates that isolated attosecond XUV pulses have been generated.



# Chapter 4

## Attosecond pulse characterization

### 4.1 Attosecond pulse characterization methods

Attosecond pulse trains can be generated by HHG using mJ-level many-cycle driver pulses, e.g., as delivered from our Ti:sapphire CPA laser system. Isolated attosecond pulses can be generated with shorter few- to single-cycle pulses with the help of several gating methods, as discussed in Section 3.3. Characterization of the attosecond XUV pulses is required before these pulses can be used for time-resolved attoscience experiments. Characterizing events with such ultrashort time durations is not an easy task. In measuring femtosecond pulses, the common practice is to use the signal pulse to sample itself by means of autocorrelation techniques as discussed in *Chapter 2*. Nonlinear optical processes are required in these methods for femtosecond pulse characterization. However, this is extremely difficult and in many cases impossible for characterizing attosecond pulses. The XUV flux available from HHG currently is typically not sufficient for inducing a nonlinear effect in material and thus allowing XUV autocorrelation measurements. Note that, in fact, XUV autocorrelation, FROG and attosecond-XUV-pump/attosecond-XUV-probe spectroscopy have been demonstrated [97]. In contrast, various methods based on IR-XUV cross-correlation have been developed for attosecond pulse characterization. Some of these methods are only applicable for measuring attosecond pulse trains while the others can be applied to retrieve both attosecond pulse trains and isolated attosecond pulses. The method called reconstruction of attosecond beating by interference of two-photon transition (RABBITT) [98] can be used to characterize attosecond pulse trains under some assumptions. It extracts the HHG phase information from the sideband oscillation. While the complete reconstruction of attosecond bursts (FROG-CRAB) [99] is applicable to both attosecond pulse trains and isolated attosecond pulses. This method makes use of the algorithms well developed for FROG [52]. However, in order to apply the FROG retrieval algorithm, which relies strongly on the Fourier transform, several approximations

are necessary. These approximations limit the application range of the method. For these reasons, a few retrieval algorithms, e.g., the volkov transform generalized projections algorithm (VTGPA) [100] and the phase retrieval by omega oscillation filtering (PROOF) [101], that do not use the Fourier transform, have been developed.

### 4.1.1 Reconstruction of attosecond beating by interference of two-photon transitions

When an XUV attosecond pulse train interacts with a noble gas medium, except for the difference from the gas atom's ionization potential, photoelectrons having the same energy distribution as the attosecond pulse train are generated. The HHG harmonic peak structure is clearly visible in the photoelectron spectrum, as shown in Fig. 4.14. When an intense laser pulse overlaps with the XUV pulse train in time and in space, the laser pulse induces free-free transitions involving the absorption or emission of  $n$  photons after the initial ionization by the XUV photons [102]. The free-free transitions lead to photoelectrons with energy separation of one laser photon energy, in contrast to the two laser photon energy separation in the pure XUV photoelectron spectrum created by the odd harmonics. In the photoelectron spectrum, the free-free transitions appear as sidebands between the XUV harmonic lines. The kinetic energy of the photoelectrons in the combined IR-XUV field is

$$K_{q,n} = (\hbar\omega_X + n\hbar\omega_{IR}) - (I_p + U_p) \quad (4.1)$$

in which  $I_p$  is the ionization potential of the target gas, and  $K_{q,n}$  is the kinetic energy of a photoelectron which ionized by the  $q$ th order harmonics and then absorbs  $n$  fundamental photons. When the laser intensity is moderate and thus the free-free transitions only involve the  $n = -1$  and  $n = +1$  processes, the sideband intensity can be written as [103]

$$S(\tau_d) \propto \int_{-\infty}^{\infty} I_X(t - \tau) I_{IR}(t) dt \quad (4.2)$$

With known  $I_{IR}(t)$  and measured  $S(\tau_d)$ , the width of  $I_X(t)$  can be deduced. However, the phase difference between different harmonic orders is ignored in the discussion above. As a result, this method does not provide a full attosecond pulse train reconstruction. When taking into account the phase of each harmonic, the intensity of the resulting XUV pulse train is

$$I_X(t) = \left| \sum_N A_q e^{i[\omega_q t + \phi_q]} \right|^2 \quad (4.3)$$

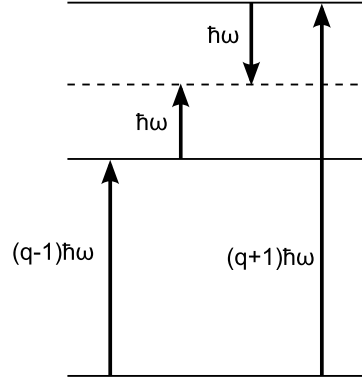


**Fig. 4.1** Principle of sideband formation used in RABBITT.

where  $A_q$  and  $\varphi_q$  are the amplitude and phase of the  $q$ th harmonic, respectively. We assume that the harmonic fields and the IR field are all monochromatic. Moreover, we only consider the situation when the laser intensity is moderate and thus only the one-photon free-free transition is involved, the amplitude of the electron wave at the sideband energy  $E_q = q\hbar\omega_{IR} - I_p$  is

$$b_q(\omega, \tau_q) = \int_{-\infty}^{\infty} dt [M_{q,q-1}M_{q-1,g}\varepsilon_{q-1}(t)E_{IR}e^{i\omega_{IR}(t-\tau_d)} + M_{q,q+1}M_{q+1,g}\varepsilon_{q+1}(t)E_{IR}e^{-i\omega_{IR}(t-\tau_d)}]e^{-i\omega t} \quad (4.4)$$

where  $\tau_d$  is the delay between the XUV beam and the IR beam.  $M_{f,i}$  is the transition matrix element from the initial state  $|i\rangle$  to the final state  $|f\rangle$ .  $g$  in  $M_{q-1,g}$  means ground state.  $E_{IR}$  is the amplitude of the IR laser field.  $\varepsilon_{q-1}(t)$  and  $\varepsilon_{q+1}(t)$  are the  $(q-1)$ -th and  $(q+1)$ -th harmonic fields, respectively,

$$\varepsilon_{q-1}(t) = E_{q-1} e^{i(\omega_{q-1}t + \varphi_{q-1})} \quad (4.5)$$

$$\varepsilon_{q+1}(t) = E_{q+1} e^{i(\omega_{q+1}t + \varphi_{q+1})} \quad (4.6)$$

We assume

$$M_{q,q-1}M_{q-1,g} = M_{q,q+1}M_{q+1,g} = M_1M \quad (4.7)$$

and

$$E_{q-1} = E_{q+1} = E_X \quad (4.8)$$

to simplify the analysis. The amplitude of the electron wave can be expressed as

$$b_q(\omega, \tau_q) = M_1ME_XE_{IR}[e^{i\varphi_{q-1}}e^{-i\omega_1\tau_d} + e^{i\varphi_{q+1}}e^{i\omega_1\tau_d}] \quad (4.9)$$



Then the intensity of the sideband is

$$I_q(\tau_q) \propto |b_q(\omega, \tau_q)|^2 = 2(M_1 M)^2 I_x I_{IR} [1 + \cos(2\omega_1 \tau_d + \varphi_{q+1} - \varphi_{q-1})] \quad (4.10)$$

In a RABBITT experiment, we scan through the delay  $\tau_d$  and record the sideband oscillation signal. The phase difference between two neighboring harmonics  $\varphi_{q+1} - \varphi_{q-1}$  then can be extracted from the position of the sideband oscillations. With the intensity and the phase of the harmonics have both been measured, the attosecond pulse train is fully characterized. This method is called reconstruction of attosecond beating by interference of two-photon transitions (RABBITT).

### 4.1.2 Complete reconstruction of attosecond burst

Different from RABBITT, which can only be applied to attosecond pulse trains, the method CRAB is also able to measure isolated attosecond pulses [99, 104]. Similar to the RABBITT technique, CRAB is also based on the photoionization happening when both an XUV field and an IR field are present. In spite of the different requirement on experimental conditions, the difference between the two methods is mainly the way of extracting the spectral phase from the measured data .

The XUV field is written as

$$\varepsilon_X(t) = E_X(t) e^{i[\omega_X t + \varphi_X(t)]} \quad (4.11)$$

regardless if the XUV field is an attosecond pulse train or isolated attosecond pulses. Following a similar procedure as the one used to obtain the photoionization transition amplitude in *Chapter 2*, the transition amplitude by the XUV field to the final state with momentum  $\vec{v}$  at time  $t$  is

$$b(\vec{v}, t) = i \int_{-\infty}^t dt' \vec{\varepsilon}_X(t') \cdot \vec{d}[\vec{v} - \vec{A}_X(t) + \vec{A}_X(t')] e^{-i(\frac{|\vec{v} - \vec{A}_X(t) + \vec{A}_X(t')|^2}{2} + I_p)t} \quad (4.12)$$

Since the XUV field is usually weak, one typically has  $\vec{A}_X(t) \ll \vec{v}$ . When observed a long time after the ionization, the XUV field is zero and the amplitude of transition becomes

$$b(\vec{v}) = i \int_{-\infty}^{\infty} dt \vec{\varepsilon}_X(t) \cdot \vec{d}(\vec{v}) e^{-i(\frac{v^2}{2} + I_p)t} = i \vec{d}(\vec{v}) \int_{-\infty}^{\infty} dt \vec{\varepsilon}_X(t) \cdot e^{-i(\frac{v^2}{2} + I_p)t} \quad (4.13)$$

Noticing that  $\omega = \frac{v^2}{2} + I_p$ ,  $b(\vec{v})$  is expressed as

$$b(\vec{v}) = i \vec{d}(\vec{v}) \int_{-\infty}^{\infty} dt \vec{\varepsilon}_X(t) e^{-i\omega t} = i \vec{d}(\vec{v}) \cdot \vec{E}_X(\omega) \quad (4.14)$$

where  $\vec{E}_X(\omega)$  is the Fourier transform of the XUV field  $\vec{\mathcal{E}}_X(t)$ . This shows that the information of the XUV field spectrum is encoded in the photoelectron spectrum.

Now consider the field is the combination of the XUV field and the IR field

$$\vec{\mathcal{E}}(t, \tau_d) = \vec{\mathcal{E}}_X(t - \tau_d) + \vec{\mathcal{E}}_{IR}(t) \quad (4.15)$$

where  $\tau_d$  is the delay between the XUV field and the IR field. The transition amplitude by the combined field to the final state with momentum  $\vec{v}$  at time  $t$  is

$$b(\vec{v}, t) = i \int_{-\infty}^t dt' \vec{\mathcal{E}}(t') \cdot \vec{d}[\vec{v} - \vec{A}(t) + \vec{A}(t')] e^{-i \int_{t'}^t dt'' \frac{1}{2} [\vec{v} - \vec{A}(t) + \vec{A}(t'')]^2 - i I_p t'} \quad (4.16)$$

Since the ionization rate induced by the XUV field is dominating, the field  $\vec{\mathcal{E}}(t)$  in the integral can be simply replaced with  $\vec{\mathcal{E}}_X(t)$ . Meanwhile, the vector potential contribution is mainly from the IR field. As a result, the transition amplitude at  $t \rightarrow \infty$  can be written as

$$b(\vec{v}, \tau_d) = i \int_{-\infty}^{\infty} dt' \vec{\mathcal{E}}_X(t - \tau_d) \cdot \vec{d}[\vec{v} + \vec{A}_{IR}(t)] e^{-i \int_t^{\infty} dt' \frac{1}{2} [\vec{v} + \vec{A}_{IR}(t')]^2 - i I_p t} \quad (4.17)$$

Eq. (4.17) can also be written as

$$b(\vec{v}, \tau_d) = i \int_{-\infty}^{\infty} dt' \vec{\mathcal{E}}_X(t - \tau_d) \cdot \vec{d}[\vec{v} + \vec{A}_{IR}(t)] e^{i \Phi_G(\vec{v}, t)} e^{-i(\frac{1}{2} + I_p)t} \quad (4.18)$$

in which

$$\Phi_G(\vec{v}, t) = - \int_t^{\infty} dt' [\vec{v} \cdot \vec{A}_{IR}(t') + \frac{1}{2} A_{IR}^2(t')] \quad (4.19)$$

is the quantum phase of the electron due to its interaction with the laser field. In experiments, the photoelectron spectrum rather than the transition amplitude is measured. By varying the delay  $\tau_d$ , a spectrogram can be obtained

$$S_e(v, \tau_d) = |b(\vec{v}, \tau_d)|^2 = \left| \int_{-\infty}^{\infty} dt' \vec{\mathcal{E}}_X(t - \tau_d) \cdot \vec{d}[\vec{v} + \vec{A}_{IR}(t)] e^{i \Phi_G(t)} e^{-i(K + I_p)t} \right|^2 \quad (4.20)$$

where  $K = \frac{1}{2}v^2$  is the electron kinetic energy. Ignoring the linear phase  $i I_p t$ , which corresponds to a frequency offset, we have

$$S_e(v, \tau_d) = |b(\vec{v}, \tau_d)|^2 = \left| \int_{-\infty}^{\infty} dt' \vec{\mathcal{E}}_X(t - \tau_d) \cdot \vec{d}[\vec{v} + \vec{A}_{IR}(t)] e^{i \Phi_G(t)} e^{-i K t} \right|^2 \quad (4.21)$$

$S_e(v, \tau_d)$  is the photoelectron spectrogram, which can be measured experimentally. The phase information of the XUV field is included in the trace. Algorithms to extract the phase informa-

tion from the measured photoelectron spectrogram are adopted from those used in the FROG retrieval. As a result, the CRAB method is usually also called FROG-CRAB.

The FROG spectrogram is expressed as

$$S(\omega, \tau_d) = \left| \int_{-\infty}^{\infty} E(t - \tau_d) G(t) e^{-i\omega t} dt \right|^2 \quad (4.22)$$

in which the temporal gate  $G(t)$  is independent of the frequency. However, the transition dipole  $\vec{d}[\vec{v} + \vec{A}_{IR}(t)]$  depends on both momentum and time. Moreover, the quantum phase  $\Phi_G(\vec{v}, t)$  also depends on both momentum and time. The dependence on momentum and time of these two terms makes it impossible to make use of the FROG algorithms to extract the phase information from the measured photoelectron spectrogram. This problem is tackled by making two approximations. First, the transition dipole  $\vec{d}[\vec{v} + \vec{A}_{IR}(t)]$  is approximated by the saddle point value  $\vec{d}[\vec{v} + \vec{A}_{IR}(\tau_d)]$ . Second, the dependence of  $\Phi_G(\vec{v}, t)$  on momentum is removed by replacing  $\vec{v}$  with  $\vec{v}_0$ , which is the central momentum of the photoelectron. The second approximation is called the central momentum approximation. Now, the trace becomes

$$S_e(v, \tau_d) = d^2[\vec{v} + \vec{A}_{IR}(\tau_d)] \left| \int_{-\infty}^{\infty} dt' \varepsilon_X(t - \tau_d) e^{i\Phi_G(\vec{v}_0, t)} e^{-iKt} \right|^2 \quad (4.23)$$

and finally the FROG-CRAB trace used for phase extraction is

$$S(v, \tau_d) = \frac{S_e(v, \tau_d)}{d^2[\vec{v} + \vec{A}_{IR}(\tau_d)]} = \left| \int_{-\infty}^{\infty} dt' \varepsilon_X(t - \tau_d) e^{i\Phi_G(\vec{v}_0, t)} e^{-iKt} \right|^2 \quad (4.24)$$

The algorithms for FROG pulse retrieval, such as the principal component generalized projections algorithm (PCGPA), can be directly adopted [105]. After the iterative retrieval process, both  $\varepsilon_X(t - \tau_d)$  and  $\Phi_G(\vec{v}_0, t)$  are fully characterized. However, if the XUV field to be characterized has a broad bandwidth compared to central momentum, the two approximations made above are no longer valid. This limits the applicability of the FROG-CRAB method.

## 4.2 Experimental apparatus and methods for attosecond pulse characterization

Both RABBITT and FROG-CRAB measurements can be conducted with the same experimental apparatus. As discussed above, both methods are based on extracting information from the experimentally measured photoelectron spectrogram. The photoionization spectra are measured with the presence of both the IR field and the XUV field. Actually, almost all the

existing methods for attosecond pulse characterization are based on extracting information for experimentally measured photoelectron spectrogram. Different methods require different experimental conditions, e.g., different methods require different laser intensities of IR beam. The required laser intensity for PROOF is  $\sim 10^{11} \text{ W/cm}^2$ , while RABBITT requires  $< 10^{12} \text{ W/cm}^2$  and FROG-CRAB requires  $\sim 10^{12} \text{ W/cm}^2$ . More importantly, the main difference between different methods lies in the way of extracting information from the experimental data.

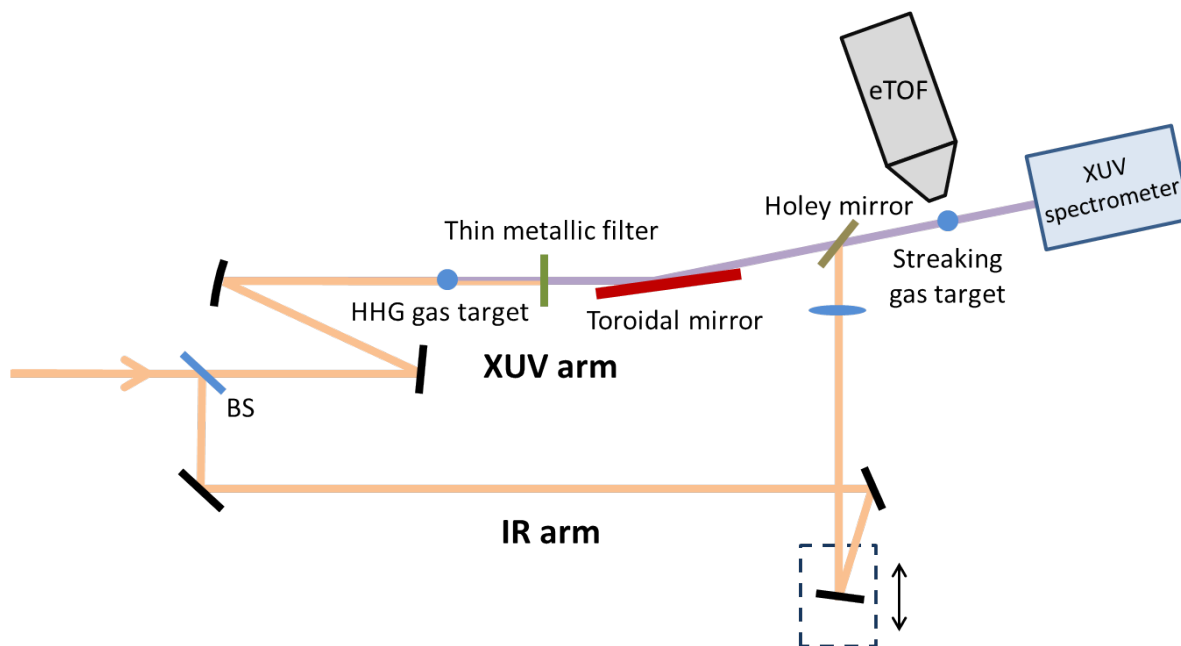


**Fig. 4.2** Schematic of the attosecond pulse characterization setup. The setup consists of a Mach-Zehnder interferometer, which splits and delays the pulses, an electron time-of-flight spectrometer (eTOF) and a XUV spectrometer. The interferometer consists of one XUV arm and one IR arm. In the XUV arm, XUV radiation is generated with HHG process and then focused with a toroidal mirror. A thin metallic filter is placed in front of the toroidal mirror to block the remaining IR field copropagating with the XUV field after the HHG source. In the IR arm, a translation stage is placed to control the arm length difference of the interferometer. The XUV field and the IR field are recombined with a holey mirror since no beam splitter is available for XUV radiation. The photoelectron spectrum from the streaking gas target is measured with the eTOF. The spectrum of the XUV radiation is also measured separately with the XUV spectrometer, which can be used as an independent reference of the photoelectron spectrum measured with the eTOF. BS: beam splitter.

The scheme of the experimental setup for attosecond pulse characterization is shown in Fig. 4.2. The optics configuration inside the HHG chamber and the toroidal mirror is shown in Fig. 4.4 and Fig. 4.3. The XUV generation setup was already discussed in *Chapter 3*. The setup consists of a Mach-Zehnder interferometer, which is for splitting and delaying the pulses, an electron time-of-flight spectrometer (eTOF) and a XUV spectrometer. The interferometer consists of the XUV arm and the IR arm. In the XUV arm, XUV radiation is generated with

HHG process and then focused with a toroidal mirror. A thin metallic filter is placed in front of the toroidal mirror to block the IR field copropagating with the XUV field. Since the thin filter is very fragile, it is moved into a "shelter" to avoid significant air flow in the vacuum pumping down and venting phase. In the IR arm, a translation stage is placed to control the arm length difference of the interferometer. Before reaching the beam combining optics, the IR beam is focused with a lens. Since the current experiments are performed with long laser pulses from the CPA system, a lens is used for focusing which simplifies the experimental setup. In contrast, when few-cycle pulses from the HCF compressor are used, the group delay dispersion (GDD) of a lens will severely distort the few-cycle pulses. As a result, only reflective optics is allowed in the beamline when few-cycle pulses are employed for experiments. The XUV field and the IR field is then recombined with a holey mirror since no beam splitter is available for XUV radiation. The center bored hole on the holey mirror allows the XUV beam to go through without interaction with any material, and the outer part of the IR beam is simply reflected by the mirror. The holey mirror is able to reflect  $\sim 80\%$  of incident energy. The focal points of the XUV beam and the IR beam overlap in the streaking gas target which is placed in the detection point of the eTOF. The photoelectron spectrum induced by the combined XUV field and IR field are measured with the eTOF, of which the axis is aligned parallel to the IR field polarization. The spectrum of the XUV radiation is also measured separately with the XUV spectrometer which has been discussed in *Chapter 3*.

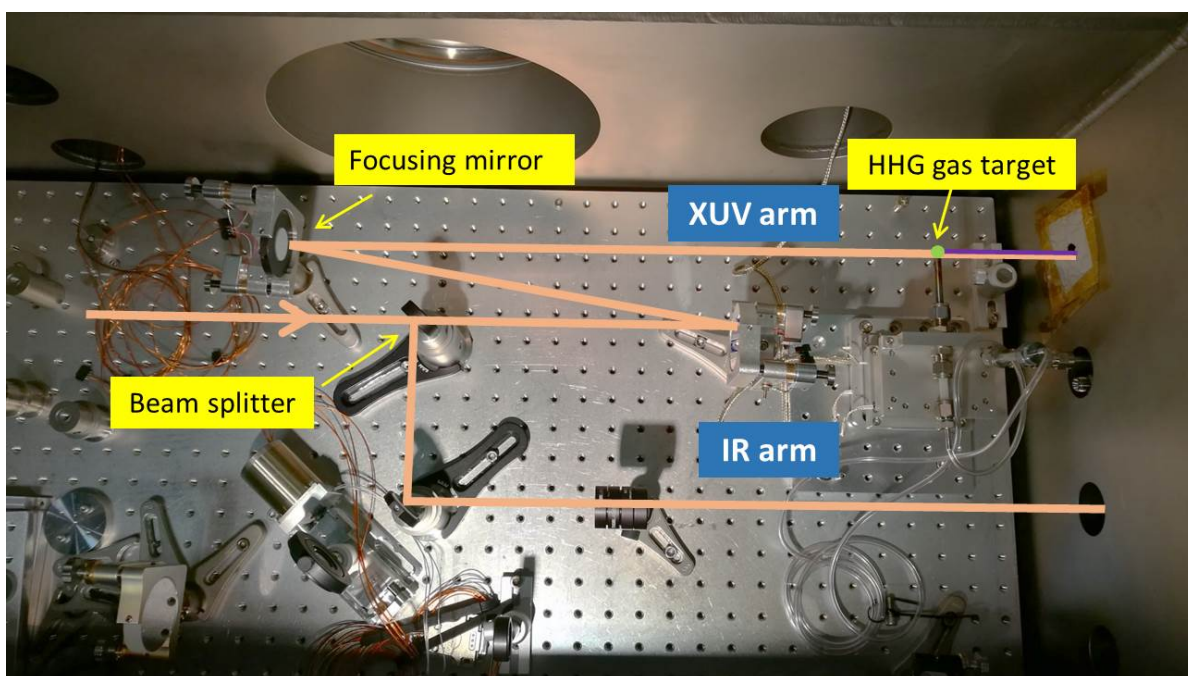


**Fig. 4.3** Optical configuration in the HHG chamber.



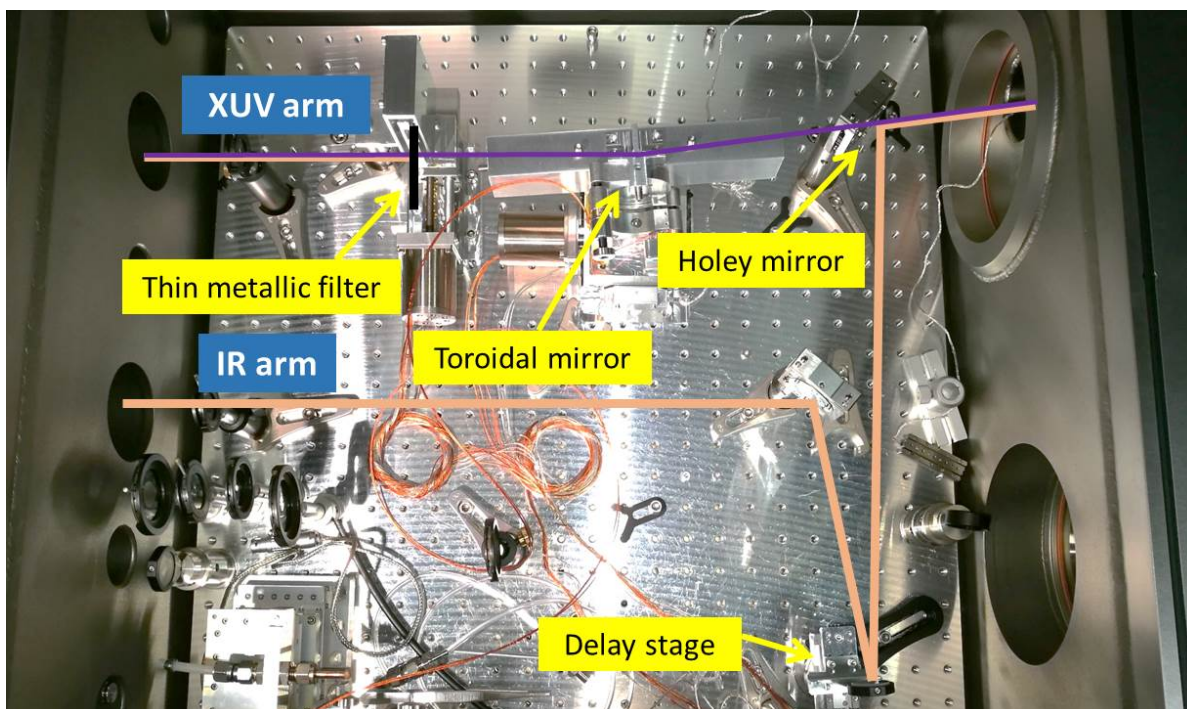
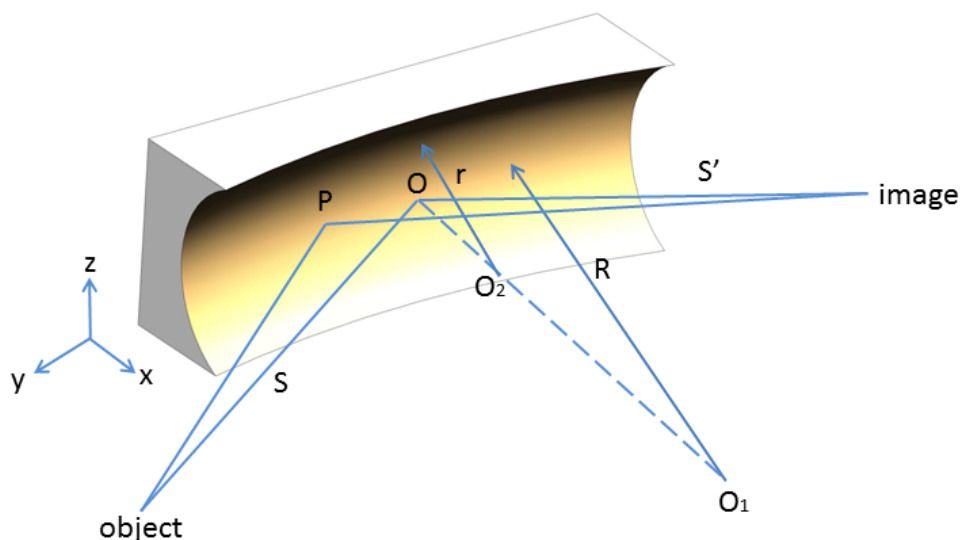


Fig. 4.4 Optical configuration in the toroidal mirror chamber.

### 4.2.1 Focusing with a toroidal mirror

In order to measure the photoelectron ionized by the XUV field, the XUV field has to be focused. Although the ionization probability by the XUV field is high, the overall number of photoelectrons is still quite low considering the extremely low flux of the XUV field. Besides, the eTOF acceptance volume is very small and photoelectrons outside of that volume cannot be detected. Therefore, it is necessary to limit the photoelectron generation region in a small volume to increase the signal-to-noise ratio. Moreover, a large photoelectron generation volume, especially outside of the acceptance volume reduces the spectral resolution of the eTOF.

Either toroidal mirrors or spherical mirrors can be used to focus XUV radiation in experiments. Spherical mirrors for XUV applications are multilayer mirrors, e.g., coated with Mo/Si as discussed in *Chapter 3*, which can be used with normal incidence. Since multilayer mirrors can be used in a similar way as normal laser mirrors, it is more convenient to design optical configurations with multilayer mirrors. Moreover, the reflection curve of multilayer mirrors can be custom tailored. However, the bandwidth of XUV multilayer mirrors is usually narrow, which means the mirrors cannot be used for outside of the designed XUV spectral range or for reflecting extremely short pulses (e.g., extending up into the "water window" spectral region). Another drawback of multilayer mirrors is that, compared to metallic mirrors, multilayer mirrors have lower reflectivity. In contrast, when metallic mirrors, usually gold



**Fig. 4.5** Schematic of a toroidal mirror.  $S$  and  $S'$  are the lengths of the entrance arm and the exit arm, respectively.  $O$  is the center of the mirror. The length of the entrance arm is measured from the object point to  $O$ , while the length of exit arm is measured from image point to  $O$ .  $P$  is an arbitrary point on the mirror.  $R$  and  $r$  are the radii of the mirror surface in the tangential plane and the sagittal plane, respectively. For the toroidal mirror used in our setup,  $R = 8000$  mm and  $r = 39$  mm.

mirrors, are used at grazing incidence, they can provide high reflectivity in a rather broad bandwidth. For instance, as shown in Fig. 3.6, gold mirrors used at  $2^\circ$  grazing incidence have reflectivity higher than 75% from 30 eV to beyond 200 eV. However, spherical mirrors cannot be used in grazing incidence due to the severe astigmatism at large incident angle. In contrast, toroidal mirrors can be used to achieve good focusing at grazing incidence.

The surface of a toroidal mirror is a portion of a torus. It has different radii of curvature along two different axes as shown in Fig. 4.5. The toroidal mirror in our experiment setup has radii  $R = 8000$  mm and  $r = 39$  mm. The reflecting surface area of the toroidal mirror is  $200\text{ mm} \times 20\text{ mm}$ . As shown in Fig. 4.6, the toroidal mirror mounting assembly consists of a kinetic mirror mount, a goniometer and a translation stage. The mirror mount allows the toroidal mirror to rotate about the  $y$ -axis and the  $z$ -axis. Meanwhile, the goniometer allows the toroidal mirror to rotate about the  $x$ -axis. With the translation stage, we can also move the toroidal mirror along the  $x$  direction. In Fig. 4.6, the thin metallic filter mount is also visible with the thin filter is moved inside the "shelter" for protection. The metallic filter is mounted also on a translation stage which allows us to move the filter in/out of the "shelter" as well as switch between different filters under vacuum environment.

Due to the different radii of curvature, the focal lengths in sagittal and tangential planes are different except at one specific incidence angle. The focal length in sagittal plane and in the

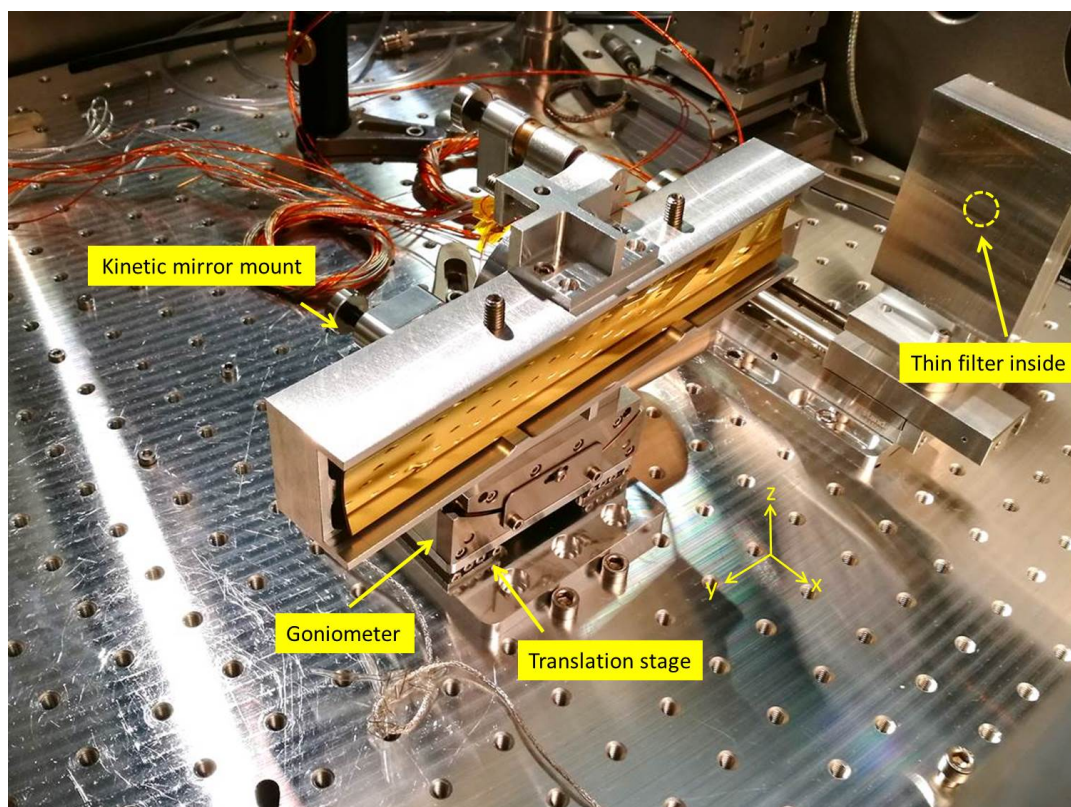


**Fig. 4.6** Toroidal mirror assembly in our experimental setup. The toroidal mirror mounting assembly consists of a kinetic mirror mount, a goniometer and a translation stage. They allow the toroidal mirror rotate about  $y$ -axis,  $z$ -axis and  $x$ -axis as well as move along the  $x$  direction. The thin metallic filter mount is also visible with the thin filter is placed inside the "shelter" for protection. The filter position is indicated with a dashed line circle.



tangential plane is [77]

$$f_{sag} = \frac{r}{2 \cos \alpha} \quad (4.25)$$

$$f_{tan} = \frac{R \cos \alpha}{2} \quad (4.26)$$

where  $\alpha$  is the incident angle. When  $\alpha = \alpha_0$  at which the focal lengths in both planes are the same, i.e., astigmatism is eliminated, we then have

$$\cos \alpha_0 = \sqrt{\frac{r}{R}} \quad (4.27)$$

Therefore, it can be calculated that the toroidal mirror in our setup has to be used with an incidence angle of  $86^\circ$ .

At this point, a stigmatic image is obtained since the aberration due to the second-order terms in the optical path function vanishes. However, the aberrations due to third-order terms still exist and will degrade the image quality. The coma aberrations in the tangential plane and in the sagittal plane are [106]

$$\Delta C_{tan} = \frac{3}{4} S D^2 \frac{M^2 - 1}{M} \tan \alpha \quad (4.28)$$

$$\Delta C_{sag} = \frac{1}{2} S D^2 \frac{M^2 - 1}{M} \tan \alpha \quad (4.29)$$

respectively, where  $M = S/S'$  is the ratio between the lengths of the entrance arm  $S$  and the exit arm  $S'$ ,  $D$  is the half-divergence of the source. It can be seen that, only when  $M = 1$ , i.e., the entrance arm equals to the exit arm, the coma aberration disappears. In this case, both arms are  $R \cos \alpha_0 = 558.6$  mm. Any deviation from this ideal case introduces coma aberration to the image. In our experimental setup, the beamline geometry prevents the toroidal mirror from being used in the ideal case. However, efforts have been made to minimize the difference between the entrance arm and the exit arm. The minimum ratio  $M_{min}$  is 1.73 with  $S = 760$  mm and  $S' = 440$  mm.

## 4.2.2 Electron time-of-flight spectrometer

As mentioned above, the characterization of attosecond XUV pulses relies on the measurement of photoelectron spectra. Various apparatus have been used to measure photoelectron spectra. An electron time-of-flight spectrometer (eTOF) is the most common apparatus used for attosecond pulse characterization [107]. The basic idea of a time-of-flight spectrometer is that particles with different momenta pointing towards the detector have different times of

flight from the common starting point to the detector. The simplest kind of eTOF consists of a field-free drift tube and an electron detector. The electron source, which is the interaction point of the XUV beam and the gas target in our case, is placed in front of the eTOF. The laser pulses generating the electrons are used as the time starting signal. When an electron arrives at the detector, the time of flight of the electron is recorded and the momentum of the electron can be calculated.

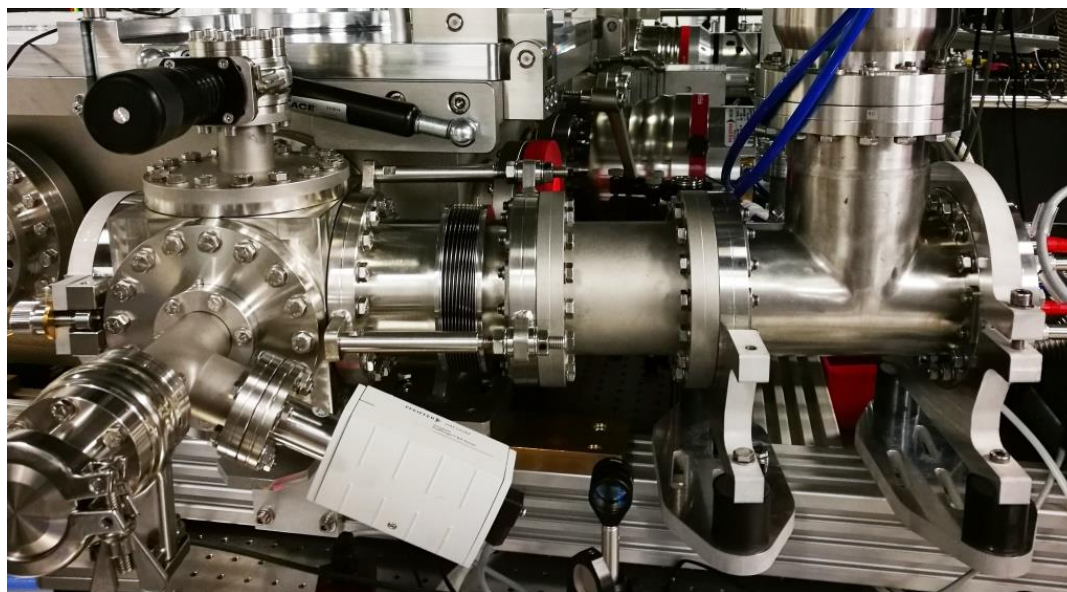


**Fig. 4.7** Electron time-of-flight spectrometer ETF11. The TOF is mounted to the chamber with a flexible bellow which allows position adjustment of the TOF entrance. The TOF axis is perpendicular to the XUV beam.

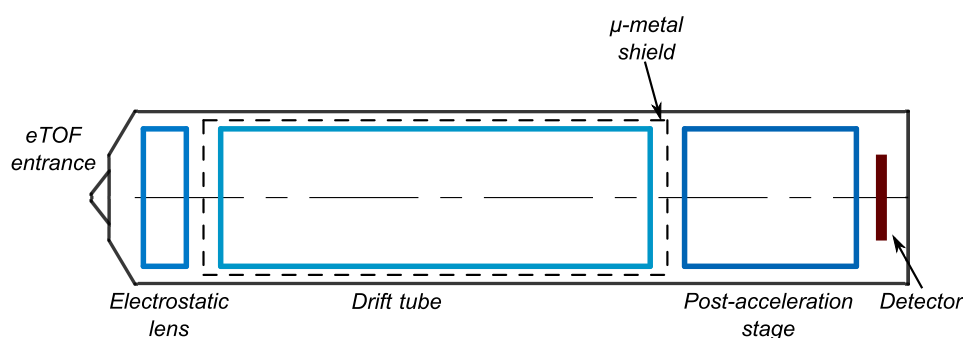


**Fig. 4.8** Schematic of a time-of-flight electron spectrometer

The eTOF employed in our experimental setup is Model ETF11 eTOF produced by STEFAN KAESDORF as shown in Fig. 4.7. It can be seen from the schematic drawing of the eTOF, Fig. 4.8, there are the two fundamental elements in an eTOF as stated above, a field-free drift tube and a detector. The drift region length is 294 mm. The drift tube is surrounded by

another tube made out of  $\mu$ -metal. The  $\mu$ -metal shields external magnetic fields, mainly the geomagnetic field from the electrons inside the drift tube.

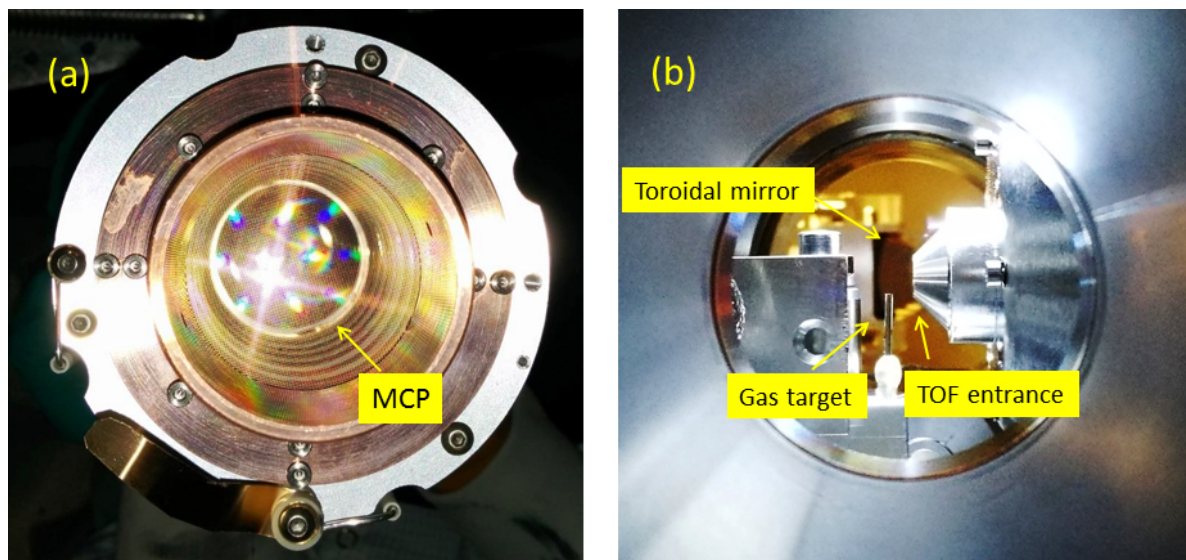


**Fig. 4.9** Photo of the MCP and the TOF. (a) photo of the MCP. The mesh which is also visible in the photo is part of the post-acceleration stage. (b) photo of the TOF entrance. The gas target is placed in front of the TOF entrance. The gas target is mounted on a translation stage which allows us move the gas target along the direction of the TOF axis. The toroidal mirror for XUV beam focusing is also visible in the photo.

The detector used in an eTOF is commonly a microchannel plate (MCP) detector. A microchannel plate is a slab made out of highly resistive material with diameter of tens of millimeters. Tiny tubes penetrating from one surface to the other are densely distributed over the whole slab, Fig. 4.12(c). The diameter of the tiny tubes is  $\sim 10 \mu\text{m}$  and the spacing between the tubes is  $\sim 15 \mu\text{m}$ . The inner wall of the tubes is coated with material for producing secondary electrons when it is bombarded by electrons with sufficient kinetic energy. The axis of the tiny tubes forms a small angle with the MCP surface normal to increase the electron multiplying efficiency. An MCP detector usually consists of two or three MCPs stacked together plus an anode. For a two-MCP stack, one input electron can produce more than  $10^6$  electrons at the backside of the stack. The multiplied electrons then induce a current signal on the anode which is then picked up by the detection electronics. The MCP used in our setup, as shown in Fig. 4.9(a), has a diameter of 40 mm and microchannel diameter of  $5 \mu\text{m}$  for faster response. The thickness of the MCP is 0.3 mm, which means the microchannel length to diameter ratio is  $L/D = 60 : 1$ . The maximum voltage that can be applied to the two-MCP stack is 2300 V. In our experiments, a voltage of 2150 V is enough for signal detection.

The entrance of the eTOF is a small opening, as shown in Fig. 4.9(b), which allows only the electrons with momentum nearly pointing in the direction of the detector to enter the

drift tube. At the eTOF entrance, an electrostatic lens is used to increase the acceptance angle. When the lens is activated, the acceptance angle is  $45^\circ$  for the electrons with the energy interested. For comparison, the acceptance angle without the electrostatic lens is estimated. The distance between the entrance and the detector is  $\sim 500$  mm. As a result, the acceptance angle can be calculated to be  $\sim 4.5^\circ$ . The lens has increased the acceptance angle by ten times. At the same time, the lens decreases the acceptance volume and makes it more difficult to align the XUV beam. The acceptance volume decreases from the diameter of the entrance, 3 mm, to only  $200 \mu\text{m}$ . With a fixed electron detection time resolution, the eTOF has a lower energy resolution for faster electrons. A retarding potential can be applied on the drift tube to slow down fast electrons for achieving the required resolution. However, the drawback of a retarding potential is that electrons with too low energy will be rejected by the drift tube and thus cannot be detected. One can perform the measurements on fast electrons and slow electrons separately. The fast electrons measurements are carried out with retarding potential, while the measurements on slow electrons are performed field-free. These measurements are then combined afterwards to form a single spectrum with enough resolution covering a broad bandwidth. On the other hand, slow electrons are vulnerable to a magnetic field influence. A "negative" retarding potential, i.e., a positive potential, can be applied to the drift tube to accelerate the electrons and thus lower the unwanted effects of an outside magnetic field. For our eTOF, the voltage range applicable to the drift tube is  $-180$  V to  $180$  V.

After the drift tube, the electrons will be accelerated in the post-acceleration stage. The voltage on the post-acceleration stage is  $1000$  V. The length of the post-acceleration stage is  $107.5$  mm. Further acceleration of the electrons lowers the effect on the electrons of the magnetic field penetrating into the rear side of the TOF. The post-acceleration also serves the purpose to increase the MCP electron detection efficiency since the typical electron detection efficiency of an MCP peaks at  $\sim 1$  keV.

A fast photodiode is used to detect the laser pulse and the detected signal is used as the start signal of the electron flight time. The fast photodiode used in our experiment has a bandwidth of  $12.5$  GHz, and the rising time is  $80$  ps, which is shorter than the rising time of MCP signals. For the stop signal of the electron flight time, i.e., the MCP signal, the situation becomes more complicated. Typically, a constant fraction discriminator (CFD) is needed to process the MCP detector signals. When electrons with identical energy arrive at the MCP detector, the MCP detector signal of each individual electron exhibits large amplitude fluctuation. If the signal arrival time is registered at a constant value, there is large timing walk, due to the signal amplitude fluctuation, which seriously degrades the time resolution. In contrast, a CFD is capable of registering the arrival time of the signal at a certain fraction of the signal amplitude, thereby minimizing the timing walk. The output signals from the CFD is then fed into a

time-to-digital converter (TDC). The digitized signals from the TDC can then be processed by a PC. At the meantime, in our experiments, the MCP signal is first amplified by a preamplifier. After that, the signal is directly recorded with an oscilloscope (Teledyne LeCroy-WaveRunner 640Zi) with 4 GHz analogue bandwidth and 20 Gs/s sampling rate.

In order to record the photoelectron time-of-flight spectrum, the oscilloscope is triggered with the signal from the fast photodiode. Usually, the electrons arrive at the MCP detector hundreds of nanoseconds after the trigger signal, and the electrons' arrival time window is also hundreds of nanoseconds. By setting the sweep window of the oscilloscope to an appropriate value, a waveform consisting of the MCP signal can be recorded. Repeating this process and adding up all the waveforms acquired, one can obtain the photoelectron time-of-flight spectrum. Usually, it takes 1000 sweeps to form a stable spectrum.

The measured photoelectron time-of-flight spectrum has to be converted to the photoelectron energy spectrum. In an ideal field-free eTOF, the time of flight to energy relation is simply

$$E_e = \frac{m_e L_d^2}{2} \frac{1}{t_f^2} \quad (4.30)$$

where  $E_e$  is the electron energy,  $L_d$  is the length of the drift region, and  $t_f$  is the time of flight. However, in practice the exact time of flight to energy relation is difficult to obtain since the electrostatic lens and the retarding potential affects the time of flight in a complicated manner, the zero of the time of flight is difficult to know, and the effect of magnetic field is always there. Despite of the difficulties, by making use of the known dimensions of the eTOF and the HHG spectrum, which has spectral peaks of known  $2\omega_0$  separation, the time-of-flight spectrum can be converted to a photoelectron energy spectrum.

Similar to the case mentioned in FROG measurements, when converting a spectrum from one domain to another domain, it is important to guarantee that the integral of the spectrum over each domain is a constant. When converting the photoelectron time of flight spectrum to photoelectron energy spectrum, the number of photoelectron signal counts must be identical before and after conversion, which means

$$\int_0^\infty I(t) dt = \int_0^\infty I(E) dE \quad (4.31)$$

or written in the derivative form

$$I(E) = -I(t) \frac{dt}{dE} \quad (4.32)$$

After converting the photoelectron time-of-flight spectrum to the photoelectron energy spectrum, the photoelectron energy spectral intensity requires further calibration since the TOF detection efficiency is not a constant over the entire energy range. In principle, this

calibration can be done by comparing the XUV spectrum measured with the XUV spectrometer and the photoelectron spectrum produced with the XUV beam. The calibration of the XUV spectrometer is performed separately, which takes into account the quantum efficiency (QE) of the XUV CCD camera, the grating diffraction efficiency, and the metallic filter transmission. Note that the photoionization probability by the XUV beam is also known quantity. Therefore, the TOF detection efficiency can be obtained.

### 4.2.3 Stability of the optical delay line

The characterization of attosecond pulses is based on the measurement of photoelectron spectra in the presence of both the XUV field and the IR field. The delay between these two fields is scanned with a step size of  $\sim 1/10$  of the IR laser cycle, which means the fluctuations of the difference between the interferometer arm lengths must be significantly smaller than  $1/10$  of the laser wavelength. For a Ti:sapphire laser, as used in our experiments, the laser cycle is  $T_0 = 2.7\text{ fs}$ , which means the step size should be  $\sim 0.3\text{ fs}$ . As discussed in *Chapter 3*, our experimental setup uses the vibration decoupling design, i.e., the optical breadboard with the interferometer is decoupled from the vacuum chamber and the vacuum pumps. The passive stability of the interferometer fulfills the experimental requirements and the stability has been characterized by interferometric measurements with a HeNe laser. The interference signal is detected with a photodiode. The arm length root-mean-square (RMS) difference is characterized to be less than  $15\text{ nm}$ , which indicates that the stability requirement of the experiments is fulfilled.

## 4.3 Experimental results of attosecond pulse characterization

The XUV beam is focused with the toroidal mirror. The focusing performance of a toroidal mirror is sensitive to the length of the entrance arm. According to Eq. (4.28) and (4.29), the coma aberration vanishes only when the length of the entrance arm is identical to the length of the exit arm. Due to the geometric limitation of our vacuum chambers, the ideal configuration of using the toroidal mirror is not applicable. However, the ratio between the entrance arm and the exit arm  $M$  is minimized to the value allowed by the setup.

The toroidal mirror focal profiles of two different  $M$  are shown in Fig 4.10. First, the entrance arm length  $S$  is set to  $1002\text{ mm}$  and thus  $M = S/S' = 1002\text{ mm}/387\text{ mm} = 2.59$ . The obtained focal profile after the toroidal mirror is shown in Fig. 4.10(b). In contrast, when the entrance arm length  $S$  is set to  $760\text{ mm}$  and thus  $M = S/S' = 760\text{ mm}/440\text{ mm} = 1.73$ , the focal



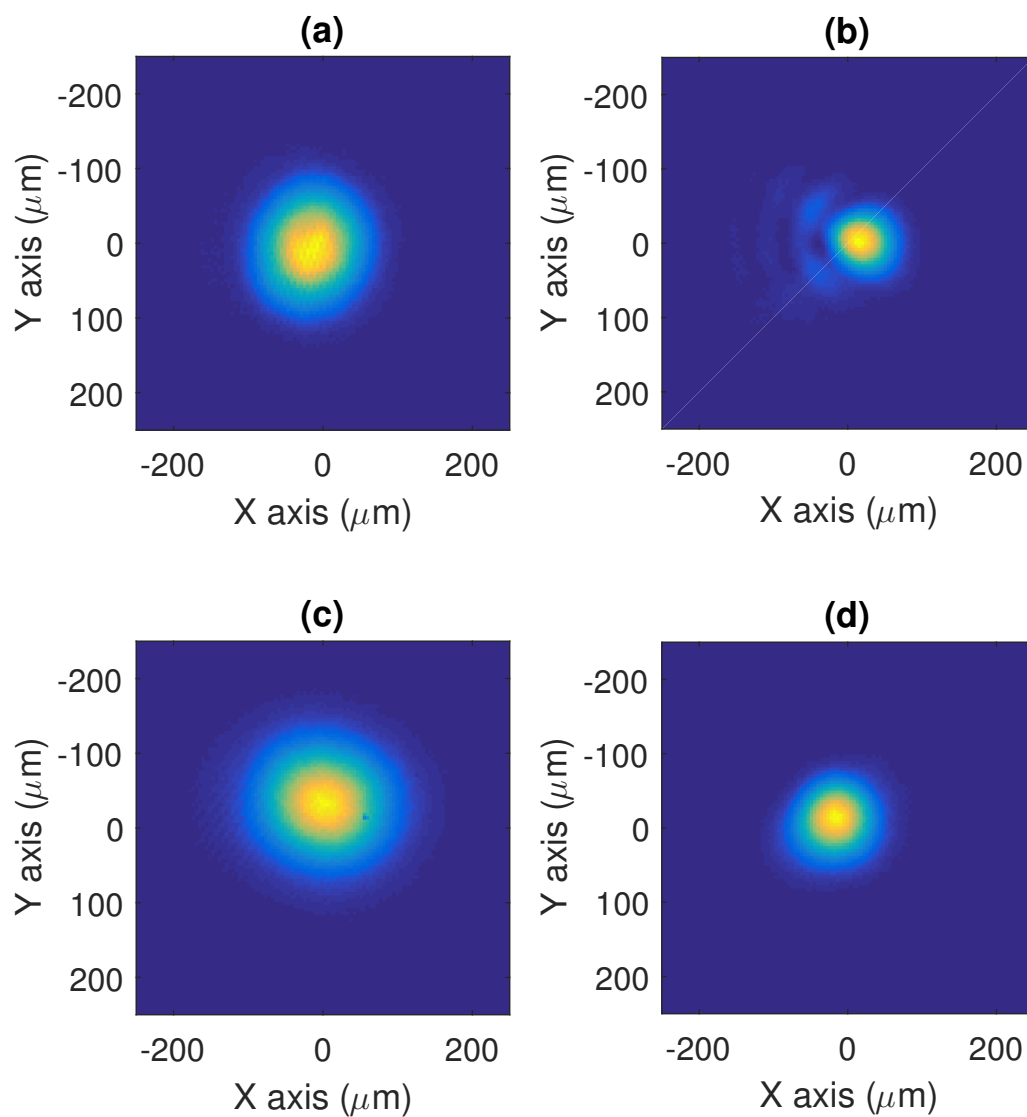


**Fig. 4.10** Toroidal mirror focal profile comparison when the ratio  $M$  between the lengths of the entrance arm  $S$  and the exit arm  $S'$  is different. (a) and (c) are the beam profiles at the HHG generation point. They are the focal points of the HHG focusing optics, a  $f = 500$  mm spherical mirror. The FWHM focal spot size in (c) is  $27.8 \mu\text{m}$ . (b) is the focal profile of the toroidal mirror when  $M = S/S' = 1002 \text{ mm} / 387 \text{ mm} = 2.59$ , the coma aberration is clearly visible. (d) shows the focal profile of the toroidal mirror when  $M = S/S' = 760 \text{ mm} / 440 \text{ mm} = 1.73$ . The FWHM focal spot size is  $17.3 \mu\text{m}$ .

profile after the toroidal mirror is improved substantially as shown in Fig. 4.10(d). Obviously, the focal profile quality becomes much better when  $|M|$  is closer to 1. In either case, the laser beam is focused first with a  $f = 500$  mm spherical mirror and then focused again with the toroidal mirror. The focal profiles of the first focusing mirror in the two cases are adjusted to as similar as possible shown in Fig. 4.10(a) and Fig. 4.10(c). The following photoelectron results are measured with the configuration in which  $M = 1.73$ .

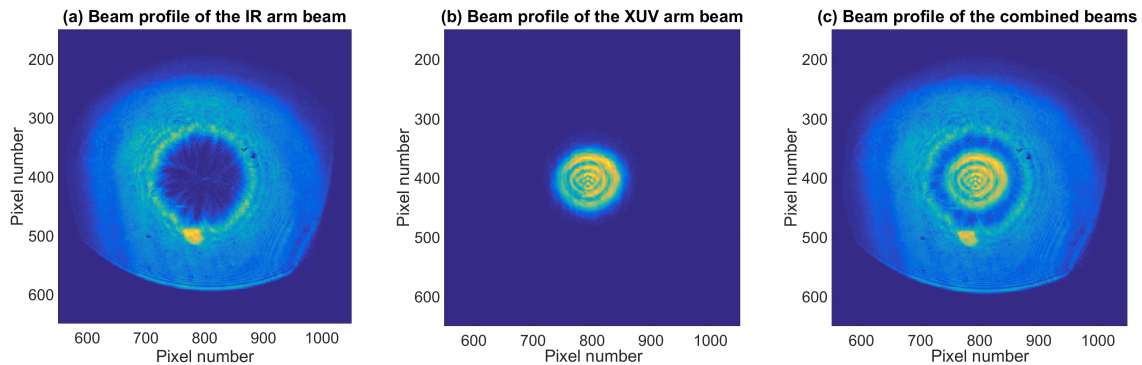


**Fig. 4.11** Combined beam profiles after the interferometer. (a) the beam from the IR arm of the interferometer (b) the beam from the XUV arm of the interferometer. (c) the beam profile of the combined beam which shows the XUV arm beam is centered with the IR arm beam.

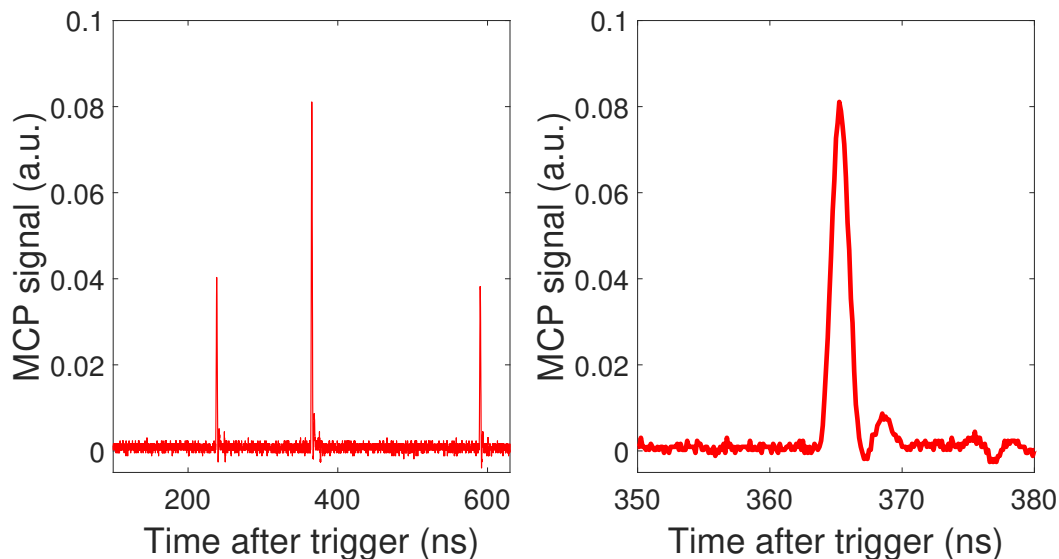


**Fig. 4.12** Raw MCP signal recorded with a 4-GHz oscilloscope. The polarity of the MCP signal is reversed. The real MCP signal is negative in voltage. (a) waveform obtained of a signal sweep, the waveform indicates that there are three signal counts within the sweep time window. (b) the shape of a MCP signal.



As discussed above, the XUV beam and the IR beam are combined with a holey mirror. The beam combining is aligned by first sending IR beams through both arms and overlap the beams from both arms. The combined beam profiles from both arms detected in a distant location are shown in Fig. 4.11. In Fig. 4.11(a) and Fig. 4.11(b), the beam profiles from the IR arm and the XUV arm of the interferometer are shown. The clip on the IR arm beam profile is due to some aperture in front of the beam camera. The holey mirror does not clip the beam in the IR arm. In Fig. 4.11(c), the combined beam profile shows that the XUV arm beam is centered with the IR arm beam.

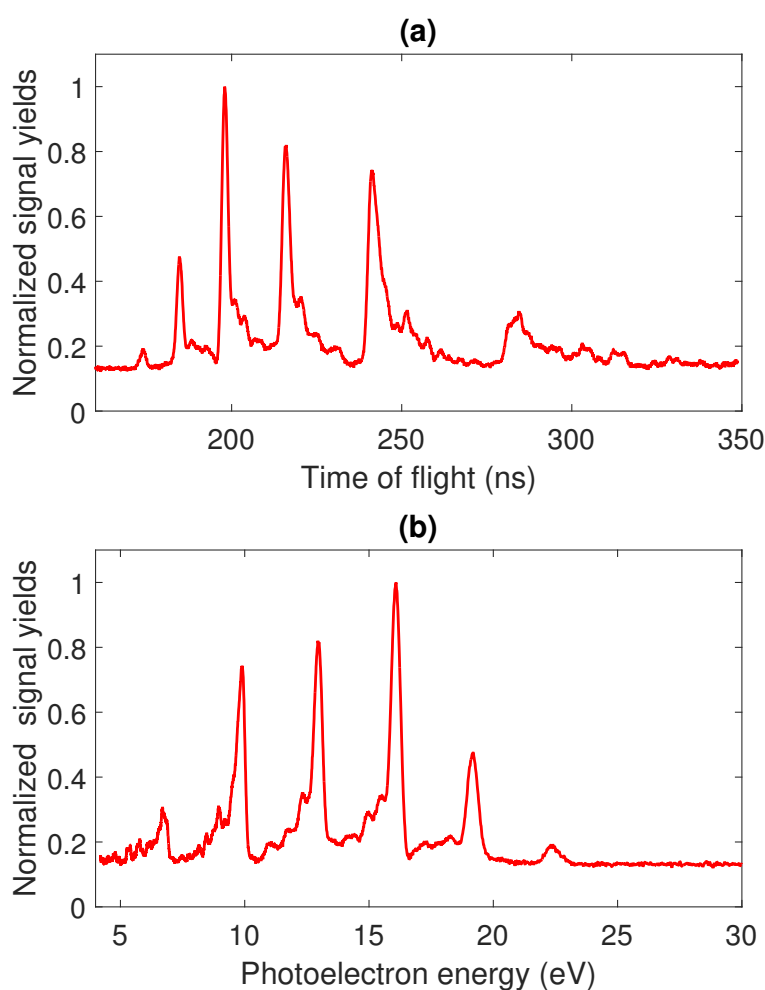


**Fig. 4.13** TOF spectrum conversion. (a) Raw time-of-flight spectrum, (b) converted photoelectron spectrum. The XUV radiation that induced the photoionization is generated via an HHG process. 35-fs laser pulses are focused with  $f = 500$  mm into a gas target backed with 125 mbar of argon gas. The laser pulse energy is 0.4 mJ. A 300-nm aluminum filter is used to block the IR beam. The streaking gas target is backed with  $\sim 1$  mbar of argon gas.

After the optical setup is aligned, the XUV field is used to generate photoelectrons which are detected by the eTOF. The MCP signals  $V(t)$  are typically negative in voltage. Here, the MCP signals recorded on the oscilloscope, as shown in Fig. 4.12, have the polarity reversed. The MCP signal recorded within one complete sweep of the oscilloscope is shown in Fig. 4.12(a). In Fig. 4.12(a), the waveform contains multi-electron-hits. Meanwhile, the shape of a MCP signal is shown in Fig. 4.12(b). By adding up waveforms from multiple sweeps, one can obtain the photoelectron time-of-flight spectrum. Note that, as shown in Fig. 4.12(b), the negative portion of one MCP signal waveform can overlap with and cancel the positive part of another waveform. This leads to signal loss and resolution reduction. As a result, before the adding up multiple MCP signal waveforms, the MCP signal waveform from each oscilloscope sweep is added to its own absolute value,  $V(t) + |V(t)|$ , to eliminate the negative portion in the signal shape.

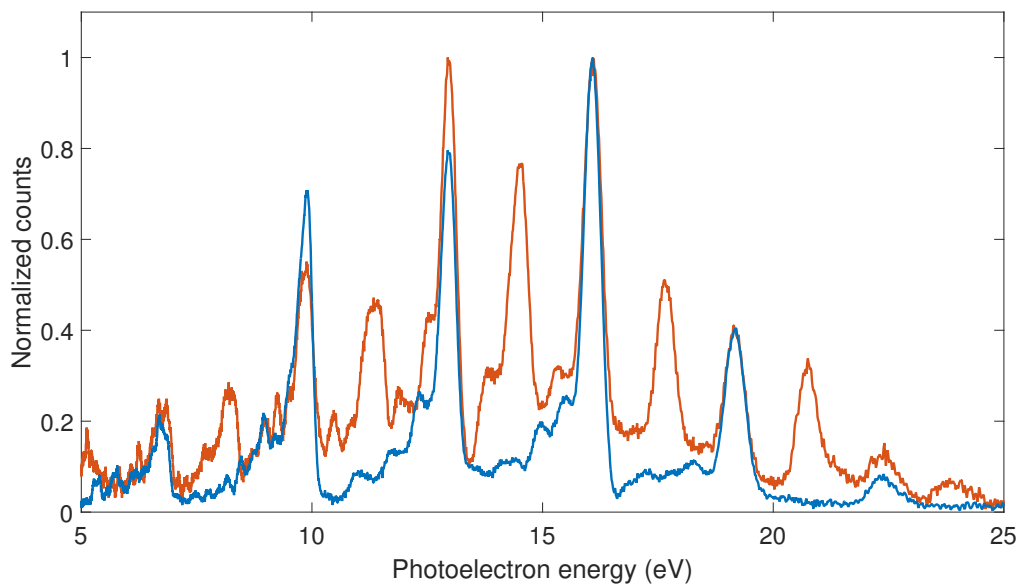


**Fig. 4.14** Photoelectron spectrum with XUV field (red trace) alone and with combined IR-XUV field (blue). The sideband structure due to the IR-field-induced continuum-continuum transitions is clearly visible. With the XUV field alone, the separation of the spikes is twice the fundamental photon energy. While with the combined IR-XUV field, the separation is halved to one fundamental photon energy.

The time-of-flight spectrum obtained by accumulating multiple waveforms on the oscilloscope is shown in Fig. 4.13(a). The electrons with higher kinetic energy arrive first and the arrival time peaks are not evenly spaced. 35-fs laser pulses are focused with  $f = 500$  mm in to a gas target backed with 125 mbar of argon gas for generating the XUV radiation. The laser pulse energy is 0.4 mJ. A 300-nm aluminum filter is used to block the IR beam. The streaking gas target is backed with  $\sim 1$  mbar of argon gas. By making use of the geometry of the eTOF

and the even-spacing HHG peaks, photoelectron time-of-flight spectrum can be converted to a photoelectron energy spectrum as shown in Fig. 4.13(b). The spectral peaks are evenly dispersed with separation of two fundamental photon energy as expected.

The photoelectron spectrum originating from the XUV field alone reproduces the HHG spectrum only with the difference of the ionization potential of the gas medium used for HHG. As discussed above, when an IR beam is spatially and temporally overlapped with the XUV field after fine adjustment, sideband signals appears in the photoelectron spectrum as shown in Fig. 4.14. The separation of the spectral peaks in the spectrum with sidebands has been narrowed down to one fundamental photon energy as expected. The XUV field used here is generated with the same conditions as the signal shown in Fig. 4.13. The pulse energy of the streaking IR field is  $\sim 30 \mu\text{J}$ , i.e.,  $\sim 8\%$  of the IR beam for HHG. By varying the delay between the IR field and the XUV field, the sideband signals change accordingly. At the point, the attosecond pulse characterization apparatus is completed.

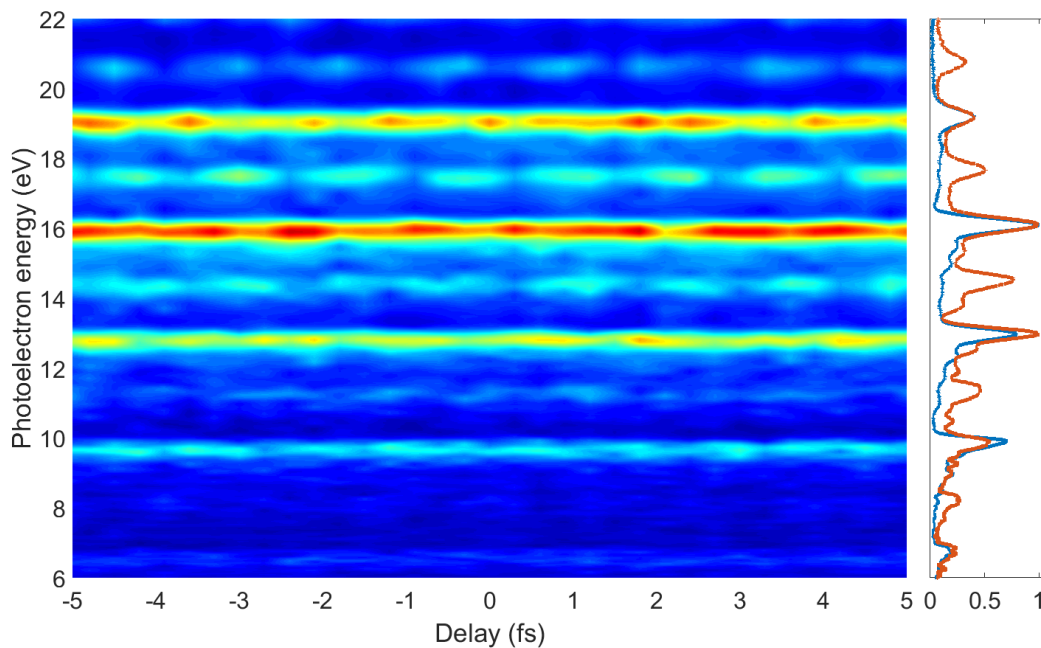


**Fig. 4.15** RABBITT photoelectron spectrogram measured with our experimental apparatus. The electron spectrum originated from only HHG is shown as blue curve on the side while the electron spectrum generated by the IR+XUV field is shown as red. The amplitudes of the sidebands oscillate with twice the IR frequency as function of delay.

After the setup is aligned, the photoelectron spectrogram can be measured. Since 35-fs laser pulses are used for current experiments, the spectrogram has to be evaluated with the RABBITT method. Thus, the photoelectron spectrogram is also referred to as the RABBITT trace. The spectrogram is obtained by scanning the delay between the XUV field and the IR

field and recording one photoelectron spectrum at each delay point. The experiment conditions are identical as used in obtaining the spectra in Fig. 4.14. The delay step size used is 0.3 fs. A measured RABBITT spectrogram is shown in Fig. 4.15. The amplitude of the spectral peaks corresponding to odd HHG orders do not change during the entire scan range. At the same time, the amplitudes of the sidebands oscillate at twice the fundamental laser frequency, which means the sideband oscillation period is  $\sim 1.35$  fs, as predicted by Eq. (4.10). The measured RABBITT spectrogram can be used to extract the spectral phases of the HHG orders using the RABBITT methods.

The photoelectron spectrogram produced with the XUV continuum as shown in Section 3.3 yet to measure, which is the task in the near future. The measured photoelectron spectrogram can then be used to fully reconstruct the XUV field with FROG-CRAB algorithm or the newly developed VTPGA algorithm [100].

## 4.4 Summary

In this chapter, the effort of constructing an attosecond XUV pulse characterization apparatus is described. First, the methods of attosecond XUV pulse characterization are discussed. The experimental apparatus and the method for implementing the characterization measurement is then further described in detail. Although focusing the XUV beam with a toroidal mirror, electron detection with eTOF, overlapping of the IR-XUV beams and the stability control of the delay are all quite technically challenging tasks, all the difficulties are successfully tackled. The presented RABBITT spectrogram indicates that a functional attosecond pulse characterization experimental apparatus has been successfully constructed.



# Chapter 5

## Conclusion and outlook

To study ultrafast dynamics by time-resolved measurements with sub-femtosecond resolution, a completely operational attosecond extreme ultraviolet (XUV) experimental apparatus has been constructed. This thesis describes the author's work on constructing the attosecond XUV experimental apparatus.

The attosecond XUV experimental apparatus consists of a few-cycle pulse laser source and an attosecond pulse generation and characterization setup. A commercial Ti:sapphire-based chirped-pulse amplification (CPA) laser system serves as the overall source of the beamline. The output pulse duration of the CPA laser system is 35 fs while the output pulse energy is 5 mJ. The laser system is actively carrier-envelope phase (CEP) stabilized. The laser pulse spectrum is broadened by means of propagation through a gas-filled hollow-core fiber (HCF). Neon gas is used as the nonlinear medium for spectral broadening which is mainly due to self-phase modulation during propagation. The HCF output pulses, spectrally broadened and temporally stretched, are recompressed with double-chirped mirrors. Typically, 2.1 mJ of the CPA laser pulse is fed into the HCF and the output pulse energy is 1.05 mJ. The compressed few-cycle pulses are characterized by SHG-FROG and the pulse duration is measured to be 5.3 fs, which corresponds to two laser optical cycles. The pulse characterization difficulties due to the broad bandwidth associated with few-cycle pulses have been tackled by exploiting the FROG trace frequency marginal correction.

Depending on the requirements of the experiments, either the CPA laser pulses or the few-cycle pulses are used for HHG in the attosecond pulse generation setup. The spectrum of the generated XUV radiation via HHG is measured with a XUV spectrometer. The XUV spectrometer is equipped with varied line spacing (VLS) flat field gratings and an XUV back-illuminated CCD camera as detector. XUV radiation has been generated from various noble gases, including krypton, argon and neon. Especially, XUV photons up to 180 eV have been generated from neon. Moreover, a narrow-bandwidth multilayer-mirror-based monochromator

for XUV pulses, which was designed and developed by our collaboration partners from Prof. T. Uphues group, was characterized in our XUV beamline. Monochromatized XUV radiation with bandwidth narrower than 0.5 eV was measured experimentally. Moreover, with the help of double optical gating, an XUV continuum was obtained. The XUV continuum supports a transform-limited pulse shorter than 300 as. Dependence of the XUV continuum on the driving pulses' CEP was also observed. The CEP dependence of the XUV continuum strongly indicates that isolated attosecond XUV pulses have been generated.

Full characterization of the attosecond pulses requires measurement of a photoelectron energy spectrogram in the presence of both the streaking IR and XUV fields. The attosecond pulse characterization setup was built to perform the photoelectron energy spectrogram measurements. In the attosecond pulse characterization setup, the XUV beam is focused by a gold coated toroidal mirror with grazing incidence. The delay between the XUV pulses and the IR pulses is controlled by varying the difference between the arm lengths of a Mach-Zehnder interferometer. The requirement of interferometric stability for attosecond streaking experiments is fulfilled passively thanks to an elaborate vibration decoupling design of our vacuum system. The photoelectron spectrum is measured with an electron time-of-flight spectrometer (eTOF). Although focusing the XUV beam with a toroidal mirror, electrons detection with eTOF, overlapping of the IR-XUV beam and the stability control of the delay are all quite technically challenging tasks, all the difficulties have been successfully tackled. The presented RABBITT spectrogram indicates that a functional attosecond pulse characterization experimental apparatus has now been successfully constructed. At this point, a completely operational attosecond extreme ultraviolet (XUV) experimental apparatus, including a few-cycle pulse laser source and an attosecond pulse generation and characterization setup, has been constructed.

Further improvements on the attosecond beamline are planned. First, the two-cycle pulses from the HCF compressor will be used directly for isolated attosecond pulses generation and FROG-CRAB traces produced by XUV continuum spectra will be measured. Efforts will also be spent on implementing the attosecond pulse reconstruction algorithm, e.g., the VTPGA which was newly developed by Phillip D. Keathley in our group. Double-chirped mirrors with customized design, which compensate high-order GDD, will be used to further compress the pulses from the HCF compressor. The output spectrum of the HCF can be further broadened by adding a second harmonic beam to the input. The output pulses from the HCF with octave-spanning spectrum can then be compressed with a spatial light modulator (SLM) down to the sub-cycle regime. Reconfiguration of the beamline, which allows better focusing quality using the toroidal mirror, will be carried out. To improve the photoelectron spectrum detection resolution, an already available eTOF with longer drift tube will be mounted on the setup. Various attosecond time-resolved pump-probe experiments can be conducted with

the experimental apparatus. The first planned experiments are femtosecond NIR-pump/XUV-probe spectroscopic studies of oxidation of CO on Pt(111) surface, and the time-resolved measurement of ultrafast surface charge transfer on  $c(4\times 2)S/Ru(0001)$  surface. In general, the attosecond beamline will serve as a powerful tool for attosecond time-resolved spectroscopy studies in the near future.





## Publication list

- [1] Roland E Mainz, Giulio Maria Rossi, Giovanni Cirimi, Yudong Yang, Oliver D Mücke, and Franz X Kärtner. High-dynamic-range arrival time control for flexible, accurate and precise parametric sub-cycle waveform synthesis. *Optics Express*, 25(4):3052–3068, 2017.
- [2] Nicolai Klemke, Giuseppe Di Sciacca, Yudong Yang, Giulio M. Rossi, Roland E. Mainz, Nicolas Tancogne-Dejean, Angel Rubio, Franz X. Kärtner, and Oliver Mücke. Generation of circularly polarized high-order harmonics in solids driven by single-color infrared pulses. In *Frontiers in Optics 2017*, page JTU3A.18. Optical Society of America, 2017. doi: 10.1364/FIO.2017.JTu3A.18. URL <http://www.osapublishing.org/abstract.cfm?URI=FiO-2017-JTu3A.18>.
- [3] Roland E Mainz, Giulio Maria Rossi, Giovanni Cirimi, Yudong Yang, Oliver D Mücke, and Franz X Kärtner. Shot-to-shot and long-term cep-stable front-end for a parallel optical waveform synthesizer. In *CLEO Pacific Rim, Singapore*, pages talk 3–2H–6, Aug 2017.
- [4] Nicolai Klemke, Giuseppe Di Sciacca, Yudong Yang, Giulio M. Rossi, Roland E. Mainz, Nicolas Tancogne-Dejean, Angel Rubio, Franz X. Kärtner, and Oliver Mücke. Circularly polarized high-order harmonics from solids driven by single-color infrared pulses. In *6th International Conference on Attosecond Physics (ATTO 2017), Xi'an, China*, page talk Wed 5:45pm, July 2017.
- [5] Giulio Maria Rossi, Roland E Mainz, Giovanni Cirimi, Yudong Yang, Oliver D Muecke, and Franz X Kaertner. Orthogonal control for stable parallel waveform synthesis. In *Nonlinear Optics*, pages NF2A–6. Optical Society of America, 2017.
- [6] Nicolai Klemke, Giuseppe Di Sciacca, Yudong Yang, Giulio Maria Rossi, Roland E Mainz, Nicolas Tancogne-Dejean, Angel Rubio, Franz X Kärtner, and Oliver D Mücke. Ellipticity dependence of higher-order harmonics in solids: unraveling the coupled intraband and interband dynamics. In *CLEO: QELS\_Fundamental Science*, pages JTh5B–10. Optical Society of America, 2017.
- [7] Giulio Maria Rossi, Roland E Mainz, Giovanni Cirimi, Yudong Yang, Oliver Muecke, and Franz Kaertner. High-dynamic-range relative arrival time measurement for accurate and precise parametric waveform synthesis. In *CLEO: Science and Innovations*, pages SM2I–3. Optical Society of America, 2017.
- [8] Roland E Mainz, Giulio Maria Rossi, Giovanni Cirimi, Yudong Yang, Shih-Hsuan Chia, Eiji J Takahashi, Oliver D Mücke, and Franz X Kärtner. Can sub-optical-cycle parametric waveform synthesizers be seeded by separate bulk white-light supercontinua? In *CLEO: Science and Innovations*, pages STu1I–6. Optical Society of America, 2016.

- 
- [9] Shih-Hsuan Chia, Giulio M Rossi, Giovanni Cirmi, Roland E Mainz, Yudong Yang, Oliver D Mücke, and Franz X Kärtner. Two-octave-wide dispersive mirrors based on dual-adiabatic-matching structures. In *Optical Interference Coatings*, pages TD–3. Optical Society of America, 2016.
- [10] Shaobo Fang, Roland Mainz, Giulio Maria Rossi, Yudong Yang, Giovanni Cirmi, Shih-Hsuan Chia, Cristian Manzoni, Giulio Cerullo, Oliver D Mücke, and Franz X Kärtner. Sub-cycle timing lock in a multi-mj parametric waveform synthesizer. In *The European Conference on Lasers and Electro-Optics*, page CG\_P\_4. Optical Society of America, 2015.
- [11] Roland Mainz, Giulio M Rossi, Cristian Manzoni, Giovanni Cirmi, Yudong Yang, Shih-Hsuan Chia, Shaobo Fang, Oliver D Mücke, Giulio Cerullo, and Franz X Kärtner. Timing jitter characterization of a high-energy sub-cycle optical waveform synthesizer. In *Advanced Solid State Lasers*, pages ATu5A–3. Optical Society of America, 2014.
- [12] Oliver D Mücke, Shaobo Fang, Giovanni Cirmi, Giulio Maria Rossi, Shih-Hsuan Chia, Hong Ye, Yudong Yang, Roland Mainz, Cristian Manzoni, Paolo Farinello, et al. Toward waveform nonlinear optics using multimillijoule sub-cycle waveform synthesizers. *IEEE journal of selected topics in quantum electronics*, 21(5):1–12, 2015.

# References

- [1] Theodore H Maiman. Stimulated optical radiation in ruby. *nature*, 187(4736):493–494, 1960.
- [2] FJ McClung and RW Hellwarth. Giant optical pulsations from ruby. *Applied Optics*, 1(101):103–105, 1962.
- [3] P. A. Franken, A. E. Hill, C. W. Peters, and G. Weinreich. Generation of optical harmonics. *Phys. Rev. Lett.*, 7:118–119, Aug 1961. doi: 10.1103/PhysRevLett.7.118. URL <https://link.aps.org/doi/10.1103/PhysRevLett.7.118>.
- [4] Willis E. Lamb. Theory of an optical maser. *Phys. Rev.*, 134:A1429–A1450, Jun 1964. doi: 10.1103/PhysRev.134.A1429. URL <https://link.aps.org/doi/10.1103/PhysRev.134.A1429>.
- [5] LE Hargrove, Richard L Fork, and MA Pollack. Locking of he–ne laser modes induced by synchronous intracavity modulation. *Applied Physics Letters*, 5(1):4–5, 1964.
- [6] A Stingl, R Szipöcs, M Lenzner, Ch Spielmann, and F Krausz. Sub-10-fs mirror-dispersion-controlled ti: sapphire laser. *Optics letters*, 20(6):602–604, 1995.
- [7] Uwe Morgner, Franz X Kärtner, Seong-Ho Cho, Yanbei Chen, Hermann A Haus, James G Fujimoto, Erich P Ippen, V Scheuer, Gregor Angelow, and Theo Tschudi. Sub-two-cycle pulses from a kerr-lens mode-locked ti: sapphire laser. *Optics letters*, 24(6):411–413, 1999.
- [8] Richard Ell, Uwe Morgner, Franz X Kärtner, James G Fujimoto, Erich P Ippen, V Scheuer, Gregor Angelow, Theo Tschudi, Max J Lederer, Alex Boiko, et al. Generation of 5-fs pulses and octave-spanning spectra directly from a ti: sapphire laser. *Optics letters*, 26(6):373–375, 2001.
- [9] Ferenc Krausz and Misha Ivanov. Attosecond physics. *Reviews of Modern Physics*, 81(1):163, 2009.
- [10] Tobias Brixner. Femtosecond quantum control. In *Book of Abstracts*, page 136, 2001.
- [11] O Albert and G Mourou. Single optical cycle laser pulse in the visible and near-infrared spectral range. *Applied Physics B: Lasers and Optics*, 69(3):207–209, 1999.
- [12] Oliver D Mücke, Shaobo Fang, Giovanni Cirimi, Giulio Maria Rossi, Shih-Hsuan Chia, Hong Ye, Yudong Yang, Roland Mainz, Cristian Manzoni, Paolo Farinello, et al. Toward waveform nonlinear optics using multimillijoule sub-cycle waveform synthesizers. *IEEE journal of selected topics in quantum electronics*, 21(5):1–12, 2015.

- [13] Cristian Manzoni, Oliver D Mücke, Giovanni Cirimi, Shaobo Fang, Jeffrey Moses, Shu-Wei Huang, Kyung-Han Hong, Giulio Cerullo, and Franz X Kärtner. Coherent pulse synthesis: towards sub-cycle optical waveforms. *Laser & Photonics Reviews*, 9(2): 129–171, 2015.
- [14] Adrian Wirth, M Th Hassan, Ivanka Grguraš, Justin Gagnon, Antoine Moulet, Tran Trung Luu, S Pabst, R Santra, ZA Alahmed, AM Azzeer, et al. Synthesized light transients. *Science*, 334(6053):195–200, 2011.
- [15] Markus Drescher. Time-resolved esca: a novel probe for chemical dynamics. *Zeitschrift für Physikalische Chemie*, 218(10/2004):1147–1168, 2004.
- [16] Michael Bauer. Femtosecond ultraviolet photoelectron spectroscopy of ultra-fast surface processes. *Journal of Physics D: Applied Physics*, 38(16):R253, 2005.
- [17] Martina Dell’Angela, T Anniyev, Martin Beye, R Coffee, Alexander Föhlisch, Jörgen Gladh, T Katayama, S Kaya, O Krupin, J LaRue, et al. Real-time observation of surface bond breaking with an x-ray laser. *Science*, 339(6125):1302–1305, 2013.
- [18] Annette Pietzsch, Alexander Föhlisch, Martin Beye, Martin Deppe, Franz Hennies, Mitsuru Nagasono, E Suljoti, W Wurth, C Gahl, K Döbrich, et al. Towards time resolved core level photoelectron spectroscopy with femtosecond x-ray free-electron lasers. *New Journal of Physics*, 10(3):033004, 2008.
- [19] M Bauer, C Lei, K Read, R Tobey, J Gland, MM Murnane, and HC Kapteyn. Direct observation of surface chemistry using ultrafast soft-x-ray pulses. *Physical Review Letters*, 87(2):025501, 2001.
- [20] Hatem Dachraoui, Martin Michelswirth, P Siffalovic, Peter Bartz, C Schäfer, B Schnatwinkel, Jochen Mattay, Walter Pfeiffer, Markus Drescher, and Ulrich Heinzmann. Photoinduced reconfiguration cycle in a molecular adsorbate layer studied by femtosecond inner-shell photoelectron spectroscopy. *Physical review letters*, 106(10): 107401, 2011.
- [21] Hatem Dachraoui, Norbert Müller, G Obermeier, C Oberer, S Horn, and Ulrich Heinzmann. Interplay between electronic correlations and coherent structural dynamics during the monoclinic insulator-to-rutile metal phase transition in vo<sub>2</sub>. *Journal of Physics: Condensed Matter*, 23(43):435402, 2011.
- [22] P Siffalovic, Markus Drescher, and Ulrich Heinzmann. Femtosecond time-resolved core-level photoelectron spectroscopy tracking surface photovoltage transients on p-gaas. *EPL (Europhysics Letters)*, 60(6):924, 2002.
- [23] L Miaja-Avila, Guido Saathoff, S Mathias, J Yin, M Bauer, M Aeschlimann, MM Murnane, HC Kapteyn, et al. Direct measurement of core-level relaxation dynamics on a surface-adsorbate system. *Physical Review Letters*, 101(4):046101, 2008.
- [24] W Wurth and D Menzel. Ultrafast electron dynamics at surfaces probed by resonant auger spectroscopy. *Chemical Physics*, 251(1):141–149, 2000.

- [25] R Díez Muiño, Daniel Sánchez-Portal, Viatcheslav M Silkin, Eugene V Chulkov, and PM Echenique. Time-dependent electron phenomena at surfaces. *Proceedings of the National Academy of Sciences*, 108(3):971–976, 2011.
- [26] Adrian L Cavalieri, Norbert Müller, Th Uphues, Vladislav S Yakovlev, A Baltuska, Balint Horvath, B Schmidt, L Blümel, R Holzwarth, S Hendel, et al. Attosecond spectroscopy in condensed matter. *Nature*, 449(7165):1029, 2007.
- [27] Cong Chen, Zhensheng Tao, Adra Carr, Piotr Matyba, Tibor Szilvási, Sebastian Emmerich, Martin Piecuch, Mark Keller, Dmitriy Zusin, Steffen Eich, et al. Distinguishing attosecond electron–electron scattering and screening in transition metals. *Proceedings of the National Academy of Sciences*, page 201706466, 2017.
- [28] Zhensheng Tao, Cong Chen, Tibor Szilvási, Mark Keller, Manos Mavrikakis, Henry Kapteyn, and Margaret Murnane. Direct time-domain observation of attosecond final-state lifetimes in photoemission from solids. *Science*, 353(6294):62–67, 2016.
- [29] Stefan Neppl, Ralph Ernstorfer, AL Cavalieri, C Lemell, G Wachter, Elisabeth Magerl, EM Bothschafter, Michael Jobst, Michael Hofstetter, Ulf Kleineberg, et al. Direct observation of electron propagation and dielectric screening on the atomic length scale. *Nature*, 517(7534):342–346, 2015.
- [30] A Föhlisch, P Feulner, F Hennies, A Fink, et al. Direct observation of electron dynamics in the attosecond domain. *nature*, 436(7049):373, 2005.
- [31] Masatoshi Hatayama, Satoshi Ichimaru, Tadayuki Ohcni, Eiji J Takahashi, Katsumi Midorikawa, and Satoshi Oku. Wide-range narrowband multilayer mirror for selecting a single-order harmonic in the photon energy range of 40–70 ev. *Optics express*, 24(13):14546–14551, 2016.
- [32] Philippe Antoine, Anne L’huillier, and Maciej Lewenstein. Attosecond pulse trains using high-order harmonics. *Physical Review Letters*, 77(7):1234, 1996.
- [33] P \_ M Paul, ES Toma, P Breger, Genevive Mullet, F Augé, Ph Balcou, HG Muller, and P Agostini. Observation of a train of attosecond pulses from high harmonic generation. *Science*, 292(5522):1689–1692, 2001.
- [34] Mauro Nisoli, Sandro De Silvestri, and Orazio Svelto. Generation of high energy 10 fs pulses by a new pulse compression technique. *Applied Physics Letters*, 68(20):2793–2795, 1996.
- [35] Sterling Backus, Charles G Durfee III, Margaret M Murnane, and Henry C Kapteyn. High power ultrafast lasers. *Review of scientific instruments*, 69(3):1207–1223, 1998.
- [36] David Huang, Morrison Ulman, Lucio H Acioli, Hermann A Haus, and James G Fujimoto. Self-focusing-induced saturable loss for laser mode locking. *Optics letters*, 17(7):511–513, 1992.
- [37] Donna Strickland and Gerard Mourou. Compression of amplified chirped optical pulses. *Optics communications*, 55(6):447–449, 1985.

- [38] P Maine, D Strickland, P Bado, M Pessot, and G Mourou. Generation of ultrahigh peak power pulses by chirped pulse amplification. *IEEE Journal of Quantum electronics*, 24(2):398–403, 1988.
- [39] Andrew Weiner. *Ultrafast optics*, volume 72. John Wiley & Sons, 2011.
- [40] Zenghu Chang. *Fundamentals of attosecond optics*. CRC Press, 2016.
- [41] Steven T Cundiff. Phase stabilization of ultrashort optical pulses. *Journal of Physics D: Applied Physics*, 35(8):R43, 2002.
- [42] David J Jones, Scott A Diddams, Jinendra K Ranka, Andrew Stentz, Robert S Windeler, John L Hall, and Steven T Cundiff. Carrier-envelope phase control of femtosecond mode-locked lasers and direct optical frequency synthesis. *Science*, 288(5466):635–639, 2000.
- [43] R Holzwarth, Th Udem, Th W Hänsch, JC Knight, WJ Wadsworth, and P St J Russell. Optical frequency synthesizer for precision spectroscopy. *Physical review letters*, 85(11):2264, 2000.
- [44] Th Udem, J Reichert, R Holzwarth, and TW Hänsch. Accurate measurement of large optical frequency differences with a mode-locked laser. *Optics letters*, 24(13):881–883, 1999.
- [45] Zenghu Chang. Carrier-envelope phase shift caused by grating-based stretchers and compressors. *Applied optics*, 45(32):8350–8353, 2006.
- [46] Enrique AJ Marcatili and RA Schmeltzer. Hollow metallic and dielectric waveguides for long distance optical transmission and lasers. *Bell Labs Technical Journal*, 43(4):1783–1809, 1964.
- [47] T. R. Schibli, O. Kuzucu, Jung-Won Kim, E. P. Ippen, J. G. Fujimoto, F. X. Kaertner, V. Scheuer, and G. Angelow. Toward single-cycle laser systems. *IEEE Journal of Selected Topics in Quantum Electronics*, 9(4):990–1001, July 2003. ISSN 1077-260X. doi: 10.1109/JSTQE.2003.819108.
- [48] F. X. Kärtner, N. Matuschek, T. Schibli, U. Keller, H. A. Haus, C. Heine, R. Morf, V. Scheuer, M. Tilsch, and T. Tschudi. Design and fabrication of double-chirped mirrors. *Opt. Lett.*, 22(11):831–833, Jun 1997. doi: 10.1364/OL.22.000831. URL <http://ol.osa.org/abstract.cfm?URI=ol-22-11-831>.
- [49] FX Kärtner, U Morgner, R Ell, T Schibli, JG Fujimoto, EP Ippen, V Scheuer, G Angelow, and T Tschudi. Ultrabroadband double-chirped mirror pairs for generation of octave spectra. *JOSA B*, 18(6):882–885, 2001.
- [50] Chris Iaconis and Ian A Walmsley. Spectral phase interferometry for direct electric-field reconstruction of ultrashort optical pulses. *Optics letters*, 23(10):792–794, 1998.
- [51] Daniel J Kane and Rick Trebino. Characterization of arbitrary femtosecond pulses using frequency-resolved optical gating. *IEEE Journal of Quantum Electronics*, 29(2):571–579, 1993.

- [52] Rick Trebino and Daniel J Kane. Using phase retrieval to measure the intensity and phase of ultrashort pulses: frequency-resolved optical gating. *JOSA A*, 10(5):1101–1111, 1993.
- [53] Henry Stark. *Image recovery: theory and application*. Elsevier, 1987.
- [54] Rick Trebino. *Frequency-resolved optical gating: the measurement of ultrashort laser pulses*. Springer Science & Business Media, 2012.
- [55] Daniel J Kane. Principal components generalized projections: a review. *JOSA B*, 25(6): A120–A132, 2008.
- [56] Kenneth W Delong, David N Fittinghoff, and Rick Trebino. Practical issues in ultrashort-laser-pulse measurement using frequency-resolved optical gating. *IEEE Journal of Quantum Electronics*, 32(7):1253–1264, 1996.
- [57] Andrius Baltuška, Maxim S Pshenichnikov, and Douwe A Wiersma. Amplitude and phase characterization of 4.5-fs pulses by frequency-resolved optical gating. *Optics letters*, 23(18):1474–1476, 1998.
- [58] A Weiner. Effect of group velocity mismatch on the measurement of ultrashort optical pulses via second harmonic generation. *IEEE journal of quantum electronics*, 19(8): 1276–1283, 1983.
- [59] A McPherson, G Gibson, H Jara, U Johann, Ting S Luk, IA McIntyre, Keith Boyer, and Charles K Rhodes. Studies of multiphoton production of vacuum-ultraviolet radiation in the rare gases. *JOSA B*, 4(4):595–601, 1987.
- [60] X. F. Li, A. L’Huillier, M. Ferray, L. A. Lompré, and G. Mainfray. Multiple-harmonic generation in rare gases at high laser intensity. *Phys. Rev. A*, 39:5751–5761, Jun 1989. doi: 10.1103/PhysRevA.39.5751. URL <https://link.aps.org/doi/10.1103/PhysRevA.39.5751>.
- [61] Jeffrey L Krause, Kenneth J Schafer, and Kenneth C Kulander. High-order harmonic generation from atoms and ions in the high intensity regime. *Physical Review Letters*, 68(24):3535, 1992.
- [62] Michael Yu Kuchiev. Atomic antenna. *JETP Lett*, 45(7):404–406, 1987.
- [63] Paul B Corkum. Plasma perspective on strong field multiphoton ionization. *Physical Review Letters*, 71(13):1994, 1993.
- [64] KC Kulander, KJ Schafer, and JL Krause. Dynamics of short-pulse excitation, ionization and harmonic conversion. In *Super-intense laser-atom physics*, pages 95–110. Springer, 1993.
- [65] LV Keldysh et al. Ionization in the field of a strong electromagnetic wave. *Sov. Phys. JETP*, 20(5):1307–1314, 1965.
- [66] DM Wolkow. Über eine klasse von lösungen der diracschen gleichung. *Zeitschrift für Physik A Hadrons and Nuclei*, 94(3):250–260, 1935.
- [67] W Becker, S Long, and JK McIver. Modeling harmonic generation by a zero-range potential. *Physical Review A*, 50(2):1540, 1994.



- [68] AM Perelomov, VS Popov, and MV Terent'ev. Ionization of atoms in an alternating electric field. *Sov. Phys. JETP*, 23(5):924–934, 1966.
- [69] AM Perelomov, VS Popov, and MV Terent'ev. Ionization of atoms in an alternating electric field: II. *Sov. Phys. JETP*, 24(1):207–217, 1967.
- [70] AM Perelomov and VS Popov. Ionization of atoms in an alternating electrical field. III. *Soviet Physics JETP*, 25(2), 1967.
- [71] Maxim V Ammosov, Nikolai B Delone, and Vladimir P Krainov. Tunnel ionization of complex atoms and atomic ions in electromagnetic field. In *High intensity laser processes*, volume 664, pages 138–141, 1986.
- [72] A. Zaïr, M. Holler, A. Guandalini, F. Schapper, J. Biegert, L. Gallmann, U. Keller, A. S. Wyatt, A. Monmayrant, I. A. Walmsley, E. Cormier, T. Auguste, J. P. Caumes, and P. Salières. Quantum path interferences in high-order harmonic generation. *Phys. Rev. Lett.*, 100:143902, Apr 2008. doi: 10.1103/PhysRevLett.100.143902. URL <https://link.aps.org/doi/10.1103/PhysRevLett.100.143902>.
- [73] M. Lewenstein, Ph. Balcou, M. Yu. Ivanov, Anne L'Huillier, and P. B. Corkum. Theory of high-harmonic generation by low-frequency laser fields. *Phys. Rev. A*, 49:2117–2132, Mar 1994. doi: 10.1103/PhysRevA.49.2117. URL <https://link.aps.org/doi/10.1103/PhysRevA.49.2117>.
- [74] Toshiaki Kita, Tatsuo Harada, N Nakano, and Hiroto Kuroda. Mechanically ruled aberration-corrected concave gratings for a flat-field grazing-incidence spectrograph. *Applied optics*, 22(4):512–513, 1983.
- [75] Paolo Villorosi. Compensation of optical path lengths in extreme-ultraviolet and soft-x-ray monochromators for ultrafast pulses. *Applied optics*, 38(28):6040–6049, 1999.
- [76] Eiji J Takahashi, Masatoshi Hatayama, Satoshi Ichimaru, and Katsumi Midorikawa. Dispersion-free monochromatization method for selecting a single-order harmonic beam. *arXiv preprint arXiv:1502.05124*, 2015.
- [77] Max Born and Emil Wolf. *Principles of optics: electromagnetic theory of propagation, interference and diffraction of light*. Elsevier, 2013.
- [78] M Th Hassan, Tran Trung Luu, Antoine Moulet, O Raskazovskaya, P Zhokhov, Manish Garg, Nicholas Karpowicz, AM Zheltikov, V Pervak, Ferenc Krausz, et al. Optical attosecond pulses and tracking the nonlinear response of bound electrons. *Nature*, 530(7588):66, 2016.
- [79] M Hentschel, R Kienberger, Ch Spielmann, Georg A Reider, et al. Attosecond metrology. *Nature*, 414(6863):509, 2001.
- [80] Reinhard Kienberger, Michael Hentschel, Matthias Uiberacker, Ch Spielmann, Markus Kitzler, Armin Scrinzi, M Wieland, Th Westerwalbesloh, U Kleineberg, Ulrich Heinzmann, et al. Steering attosecond electron wave packets with light. *Science*, 297(5584):1144–1148, 2002.

- [81] Andrius Baltuška, Th Udem, M Uiberacker, M Hentschel, E\_ Goulielmakis, Ch Gohle, Ronald Holzwarth, VS Yakovlev, A Scrinzi, Th W Hänsch, et al. Attosecond control of electronic processes by intense light fields. *Nature*, 421(6923):611–615, 2003.
- [82] Johan Mauritsson, Per Johnsson, E Gustafsson, Anne L’Huillier, KJ Schafer, and MB Gaarde. Attosecond pulse trains generated using two color laser fields. *Physical review letters*, 97(1):013001, 2006.
- [83] Yu Oishi, Masanori Kaku, Akira Suda, Fumihiko Kannari, and Katsumi Midorikawa. Generation of extreme ultraviolet continuum radiation driven by a sub-10-fs two-color field. *Optics express*, 14(16):7230–7237, 2006.
- [84] Thomas Pfeifer, Lukas Gallmann, Mark J. Abel, Phillip M. Nagel, Daniel M. Neumark, and Stephen R. Leone. Heterodyne mixing of laser fields for temporal gating of high-order harmonic generation. *Phys. Rev. Lett.*, 97:163901, Oct 2006. doi: 10.1103/PhysRevLett.97.163901. URL <https://link.aps.org/doi/10.1103/PhysRevLett.97.163901>.
- [85] H Vincenti and F Quéré. Attosecond lighthouses: how to use spatiotemporally coupled light fields to generate isolated attosecond pulses. *Physical review letters*, 108(11):113904, 2012.
- [86] Jonathan A Wheeler, Antonin Borot, Sylvain Monchocé, Henri Vincenti, Aurélien Ricci, Arnaud Malvache, Rodrigo Lopez-Martens, and Fabien Quéré. Attosecond lighthouses from plasma mirrors. *Nature Photonics*, 6(12):829–833, 2012.
- [87] TJ Hammond, Graham G Brown, Kyung Taec Kim, DM Villeneuve, and PB Corkum. Attosecond pulses measured from the attosecond lighthouse. *Nature Photonics*, 10(3):171, 2016.
- [88] Zenghu Chang. Single attosecond pulse and xuv supercontinuum in the high-order harmonic plateau. *Physical Review A*, 70(4):043802, 2004.
- [89] Giuseppe Sansone, E Benedetti, Francesca Calegari, Caterina Vozzi, Lorenzo Avaldi, Roberto Flammini, Luca Poletto, P Villoresi, C Altucci, R Velotta, et al. Isolated single-cycle attosecond pulses. *Science*, 314(5798):443–446, 2006.
- [90] P Tzallas, E Skantzakis, C Kalpouzos, EP Benis, George D Tsakiris, and D Charalambidis. Generation of intense continuum extreme-ultraviolet radiation by many-cycle laser fields. *Nature physics*, 3(12):846, 2007.
- [91] Zenghu Chang. Controlling attosecond pulse generation with a double optical gating. *Physical Review A*, 76(5):051403, 2007.
- [92] Hiroki Mashiko, Steve Gilbertson, Chengquan Li, Sabih D Khan, Mahendra M Shakya, Eric Moon, and Zenghu Chang. Double optical gating of high-order harmonic generation with carrier-envelope phase stabilized lasers. *Physical review letters*, 100(10):103906, 2008.
- [93] Ximao Feng, Steve Gilbertson, Hiroki Mashiko, He Wang, Sabih D. Khan, Michael Chini, Yi Wu, Kun Zhao, and Zenghu Chang. Generation of isolated attosecond pulses with 20 to 28 femtosecond lasers. *Phys. Rev. Lett.*, 103:183901, Oct 2009. doi: 10.

- 1103/PhysRevLett.103.183901. URL <https://link.aps.org/doi/10.1103/PhysRevLett.103.183901>.
- [94] NH Burnett, C Kan, and PB Corkum. Ellipticity and polarization effects in harmonic generation in ionizing neon. *Physical Review A*, 51(5):R3418, 1995.
- [95] Misha Yu Ivanov, Thomas Brabec, and Neal Burnett. Coulomb corrections and polarization effects in high-intensity high-harmonic emission. *Physical Review A*, 54(1):742, 1996.
- [96] K. S. Budil, P. Salières, Anne L’Huillier, T. Ditmire, and M. D. Perry. Influence of ellipticity on harmonic generation. *Phys. Rev. A*, 48:R3437–R3440, Nov 1993. doi: 10.1103/PhysRevA.48.R3437. URL <https://link.aps.org/doi/10.1103/PhysRevA.48.R3437>.
- [97] Eiji J Takahashi, Pengfei Lan, Oliver D Mücke, Yasuo Nabekawa, and Katsumi Midorikawa. Infrared two-color multicycle laser field synthesis for generating an intense attosecond pulse. *Physical review letters*, 104(23):233901, 2010.
- [98] Y Mairesse, A De Bohan, LJ Frasinski, H Merdji, LC Dinu, P Monchicourt, P Breger, M Kovačev, R Taïeb, B Carré, et al. Attosecond synchronization of high-harmonic soft x-rays. *Science*, 302(5650):1540–1543, 2003.
- [99] Yann Mairesse and F Quéré. Frequency-resolved optical gating for complete reconstruction of attosecond bursts. *Physical Review A*, 71(1):011401, 2005.
- [100] PD Keathley, S Bhardwaj, J Moses, G Laurent, and FX Kärtner. Volkov transform generalized projection algorithm for attosecond pulse characterization. *New Journal of Physics*, 18(7):073009, 2016.
- [101] Michael Chini, Steve Gilbertson, Sabih D Khan, and Zenghu Chang. Characterizing ultrabroadband attosecond lasers. *Optics express*, 18(12):13006–13016, 2010.
- [102] Aurelia Cionga, Viorica Florescu, Alfred Maquet, and Richard Taïeb. Target dressing effects in laser-assisted x-ray photoionization. *Physical Review A*, 47(3):1830, 1993.
- [103] TE Glover, RW Schoenlein, AH Chin, and CV Shank. Observation of laser assisted photoelectric effect and femtosecond high order harmonic radiation. *Physical Review Letters*, 76(14):2468, 1996.
- [104] Markus Kitzler, Nenad Milosevic, Armin Scrinzi, Ferenc Krausz, and Thomas Brabec. Quantum theory of attosecond xuv pulse measurement by laser dressed photoionization. *Physical review letters*, 88(17):173904, 2002.
- [105] Justin Gagnon, Eleftherios Goulielmakis, and Vladislav S Yakovlev. The accurate frog characterization of attosecond pulses from streaking measurements. *Applied Physics B: Lasers and Optics*, 92(1):25–32, 2008.
- [106] L Poletto, F Frassetto, F Calegari, S Anumula, A Trabattoni, and M Nisoli. Microfocusing of attosecond pulses by grazing-incidence toroidal mirrors. *Optics express*, 21(11):13040–13051, 2013.
- [107] Ximao Feng, Steve Gilbertson, Sabih D Khan, Michael Chini, Yi Wu, Kevin Carnes, and Zenghu Chang. Calibration of electron spectrometer resolution in attosecond streak camera. *Optics express*, 18(2):1316–1322, 2010.